

ESTIMATION OF SOIL MOISTURE CONTENT USING GPR AND TIME- LAPSE RESISTIVITY: A CASE STUDY OF KNUST ANWOMASO OIL PALM PLANTATION

KNUST

By

NATHANIEL SACEKEY

(BSc. Geology)

A Thesis Submitted to the Department of Physics,
Kwame Nkrumah University of Science and Technology,
In partial fulfillment of the requirements for the degree
of
MASTER OF PHILOSOPHY (GEOPHYSICS)
College of Science

Supervisor: Dr. Kwasi Preko

© Department of Physics

October, 2014.

DECLARATION

I hereby declare that this submission is my own work towards the award of M.Phil. Degree in Geophysics and that, to the best of my knowledge, it contains no material previously published by another person or material which has been accepted for the award of any other degree of the University, except where due acknowledgement has been made in the text.

KNUST

Nathaniel Sackey (20291157)

.....
Student's Name

.....
Signature

.....
Date

Certified by:

Dr. Kwasi Preko

.....
Supervisor's Name

.....
Signature

.....
Date

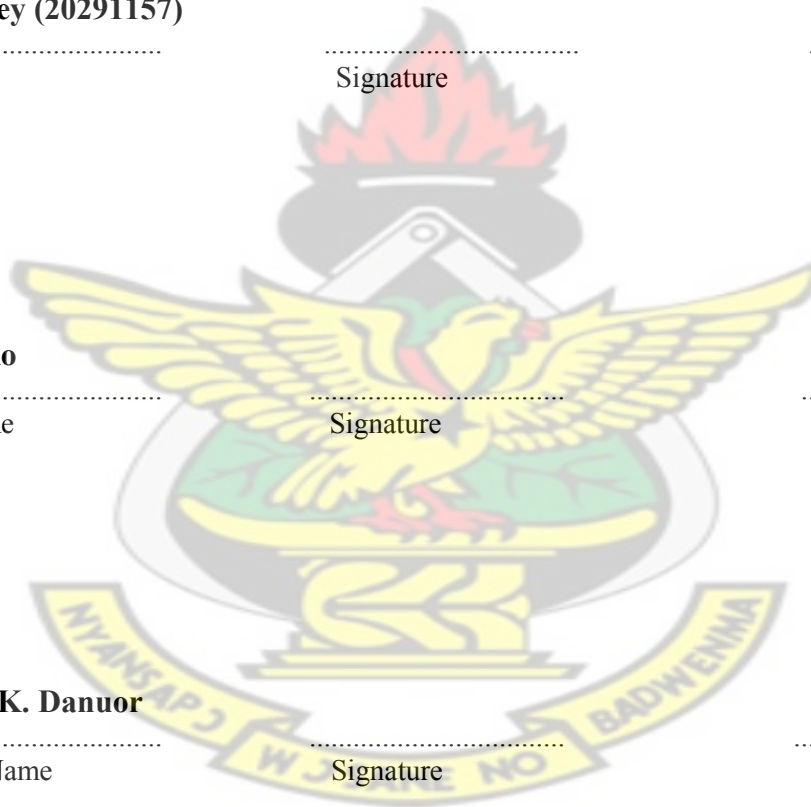
Certified by:

Prof. Sylvester K. Danuor

.....
Head of Dept.'s Name

.....
Signature

.....
Date



ABSTRACT

The viability of the ground penetrating radar (GPR) and time lapse resistivity measurements to assess the temporal and spatial variation of the volumetric water content in soil was tested in this work at the KNUST Agricultural Research station at Anwomaso - Kumasi. In the case of the GPR, the surface water content was measured with the ground wave, which is a direct wave between the transmitter and receiver through the upper centimeters of the soil. Spatial water content variation was measured on a 32 day monitoring period along four (4) 82 m profile lines. Electrical resistivity tomography (ERT) was used to measure resistivity at the experimental site with the objective of quantifying soil moisture for 20 days. This was based on the fact that, the degree of water saturation affects the resistivity measured hence water moisture could be imaged from the resistivity measurements. The time-series data set was used to generate desaturation models. It was observed from the results that rainfall affects the volumetric soil water and the resistivities measured. It was concluded that the non-invasive GPR measurements provide the means to accurately and consistently monitor the spatial water content variation in time at shallow depths with water content ranging from $0.06 \text{ m}^3/\text{m}^3$ to $0.4 \text{ m}^3/\text{m}^3$ whereas resistivity measurements are useful in imaging the moisture content at deeper depth.

CONTENTS

Abstract.....	i
Content	ii
List of figures.....	vi
List of tables	ix
List of software used	x
List of used symbols	xi
Acknowledgement	xii
CHAPTER 1	1
Introduction	1
1.1 Background to Research.....	2
1.2 Statement of Problem.....	2
1.3 Research Objectives	3
1.4 Justification of Thesis.....	4
1.6 Structure of Thesis	4
CHAPTER 2	5
Literature Review And Theoretical Background	5
2.1 Literature review	5
2.2 Background of Ground Penetrating Radar	8
2.2.1 Electromagnetic wave propagation	9
2.2.2 Maxwell's Equations	11

2.2.3 Constitutive Relations.....	13
2.2.4 The Physical Properties of soil	15
2.2.5 Topp's Model	16
2.2.6 GPR ground wave.....	17
2.2.7 Data collection modes for GPR	17
2.2.8 Penetration depth	18
2.2.9 Attenuation	18
2.3 Background of Electrical resistivity.....	20
2.3.1 Electrical Resistivity theory.....	20
2.3.2 Configurations of Electrical Resistivity surveys	23
CHAPTER 3	27
Materials And Methods	27
3.1 Project Site	27
3.1.1 Topography.....	27
3.1.2 Geology of site.....	28
3.1.3 Soil.....	30
3.1.4 Climate.....	30
3.1.5 Vegetation.....	30
3.1.6 Land Use.....	30
3.2 Data Acquisition.....	30

3.2.1 Ground Penetrating Radar Measurements	31
3.2.2 Field Procedures	33
3.2.2 Time-Lapse Electrical Resistivity Measurement.....	37
3.3 Data Processing	40
3.3.1 GPR Processing Procedure	40
3.3.2 Electrical Resistivity Processing	46
CHAPTER 4	48
Results And Discussion	48
4.0 Introduction	48
4.1 GPR Results	48
4.1.1 Spatial water distribution.....	55
4.1.2 Influence of Rainfall on Water Content	58
4.2 Resistivity Models.....	60
4.2.1 Desaturation Models.....	66
4.3 Comparison of Results	69
4.4 Summary of Results	73
CHAPTER 5	76
Conclusion And Recommendations	76
5.1 Conclusion.....	76
5.2 Recommendations	78

References	79
Appendix A	88
Appendix B	91
Appendix C	95

KNUST



LIST OF FIGURES

Figure 2.1: GPR setup and wave propagation.....	9
Figure 2.2: Schematic diagram of an electromagnetic wave	10
Figure 2.3: Current flow from a point source	21
Figure 2.4: Electrical resistivity measurement setup	22
Figure 2.5: Electrode configuration for the various arrays	25
Figure 3.1: Project site location.....	27
Figure 3.2: Topography of research site	28
Figure 3.3: Geological map of Kumasi Metropolis	29
Figure 3.4: Profile lines at project site	31
Figure 3.5: The Mala GPR system.....	33
Figure 3.6: Monitor Interface; settings	34
Figure 3. 7: GPR setup showing wooden cart (A), transmitter (B) and receiver (C)	36
Figure 3.8: Data acquisition; moving cart along profile lines	36
Figure 3.9: Resistivity measurement using the terrameter (A), Selector (B), multi-core cable... ..	38
Figure 3.10: Line setup for measurements.....	39
Figure 3.11: Sketch of electrodes for resistivity measurements in building a pseudosection	39
Figure 3.12: Schematic diagram showing processing sequence	42
Figure 3.13: GPR data in point mode showing unprocessed data (X), processed data (Y),	44

Figure 3.14: GPR data in wiggle mode showing airwave (A) and ground wave (B)	45
Figure 4.1: Volumetric water content for 17 th to 21 st June 2013 on line 1.....	50
Figure 4.2: Volumetric water content on line 1 from 24 th June to 27 th June 2013	50
Figure 4.3: Volumetric water content distribution on line 2 from 24 th June to 27 th July 2013 ...	51
Figure 4.4: Volumetric water content distribution on line 2 from 2 nd July to 5 th July 2013.....	51
Figure 4.5: Volumetric water content distribution on line 3 from 24 th June to 27 th June 2013 ...	53
Figure 4.6: Volumetric water content for 16 th August to September 3 rd 2013 on line 3.	53
Figure 4.7: Volumetric water content distribution on line 4 from 2 nd July to 5 th July 2013	54
Figure 4.8: Volumetric water content distribution on line 4 from 5 th to 14 th August 2013	54
Figure 4.9: Spatial water content distribution for 17 th June 2013	56
Figure 4.10: Spatial water content distribution for 2 nd July 2013.....	56
Figure 4.11: Spatial water distribution for 26 th July 2013	57
Figure 4.12: Spatial water content distribution for 3 rd September 2013	57
Figure 4.13: Relation between soil moisture and precipitation;	59
Figure 4.14: Resistivity models for line 1 from 9 th to 12 th July 2013.	61
Figure 4.15: Resistivity models for line 2 from 12 th July to 22 nd July 2013	62
Figure 4.16: Resistivity models for 24 th July to 7 th August 2013 on line 3	64
Figure 4.17: Resistivity models for 16 to 26 th August 2013 on line 4	65
Figure 4.18: Desaturation models for 10 th and 22 nd of July and 16 th August 2013 on line 4	67

Figure 4.19: Desaturation models for 19 th , 23 rd and 26 th of August 2013	68
Figure 4.20: Spatial distribution of the volumetric water content for 9 th of July 2013	70
Figure 4.21: 3D resistivity model for the survey area on July 9 th 2013.	70
Figure 4.22: Surface plot of volumetric water content for 26 th August 2013	72
Figure 4.23: 3D resistivity model for the field on 26 th August 2013.....	72
A 1: Script to compare files for equal data points.....	88
A 2: Sample script to join files	88
A 3: Script to collate 2D resistivity data into 3D.....	89
B 1: GPR result for line 1.....	91
B 2: Results for line 2	92
B 3: Results for line 3	93
B 4: Results for line 4	94
C 1: Resistivity results for August on line 1.....	95
C 2: Resistivity results for August on line 2.....	96
C 3: Resistivity results for August on line 3.....	97
C 4: Resistivity results for August on line 4.....	98
C 5: 3D resistivity for 18 th July 2013	99
C 6: 3D resistivity for 26 th July 2013	99
C 7: 3D resistivity for 26 th August 2013	99

LIST OF TABLES

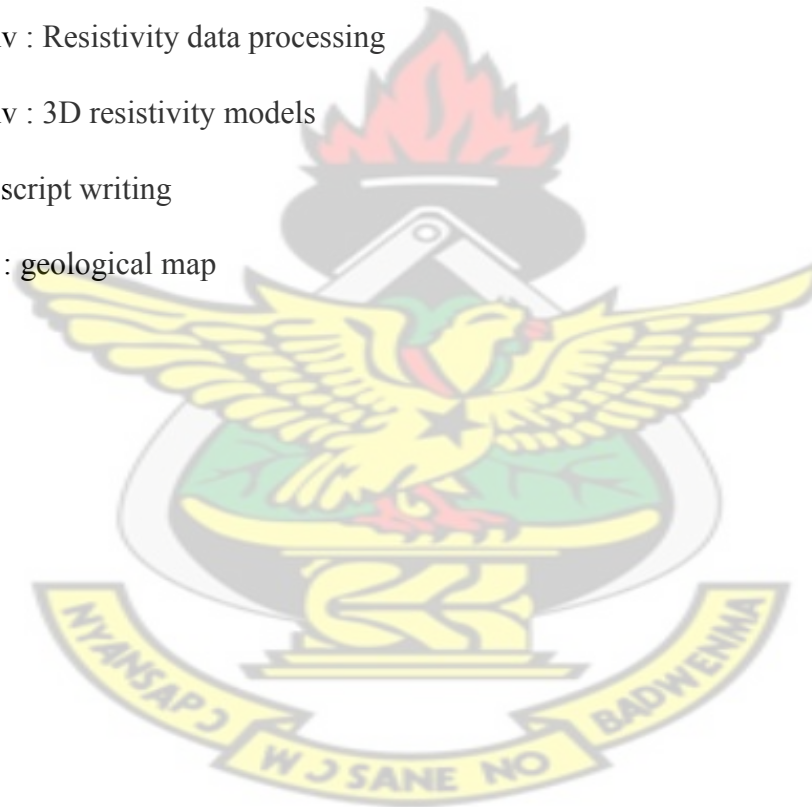
Table 2.1: Electrical properties of geological materials	19
Table 2.2: Resistivity of earth materials	23
Table A 1: Measurement days and rainfall rates.....	90

KNUST



LIST OF SOFTWARES USED

- Microsoft Paint: graphics.
- Corel PAINT Graphics 12: graphics.
- Golden Software Grapher 8: statistical analysis and plots.
- Microsoft Excel: data processing.
- Microsoft Word: typesetting.
- Reflexw 4.5: GPR data processing
- Res2DInv : Resistivity data processing
- Res3DInv : 3D resistivity models
- Ubuntu: script writing
- Arc GIS : geological map



LIST OF USED SYMBOLS

c – speed of light [$3 \times 10^8 \text{ ms}^{-2}$]

E – Electric field [Vm^{-1}]

H – Magnetic field [Am^{-1}]

J – Electric charge density [Am^{-3}]

ρ – Volume charge density [Cm^{-3}]

D – Electric flux density [Cm^{-2}]

B – Magnetic flux density [Wm^{-2}]

σ – Conductivity [S]

ϵ_0 – Permittivity of free space [$8.854 \times 10^{-12} \text{ Fm}^{-1}$]

μ_0 – Permeability of free space [$4\pi \times 10^{-12} \text{ Hm}^{-1}$]

ϵ_r – Relative permittivity

μ_r – Relative permeability

ϵ – Permittivity of material

μ – Permeability of material

χ – Electric susceptibility

χ_m – Magnetic susceptibility

n – Refractive index

v – Velocity of radar wave

θ_v – Volumetric water content

L – Attenuation

α – Attenuation constant

R – Resistance

ρ – Resistivity [Ωm]

I – Current [A]

V – Potential difference [V]

ACKNOWLEDGEMENT

This work was carried out at the KNUST Agricultural Research Station at Anwomaso, Kumasi. My profound gratitude therefore goes to the staff and supervisor at the station for their support during the 3 months of work. Their output is greatly appreciation for the successful completion of this project.

I wish to express my sincere gratitude to my supervisor, Dr. Kwasi Preko and also to Dr. Akwasi Acheampong Aning for the opportunity to carry out this research, excellent working conditions, supervision on the field and the many invaluable suggestions.

I am highly indebted to the post graduate students in the Physics Department especially the Geophysics Section for their time with me in the field. I also acknowledge Mr. Jakalia I. Sontaa for his continued support during very difficult times and for creating a very pleasant working environment without which this work could not have been brought this far.

The Physics Department readily provided me with all the needed tools and software packages “Reflexw” and “Res2DInv” which were used to process the data. The equipments could not have been properly operated without the help of Mr. Thomas Dwomoh who always found time to assist me in the field.

I wish to express my profound thanks to Mr. Thomas Quansah who transported me to and from the field even in bad weather.

Finally, I acknowledge the friendliness and pleasant working atmosphere created by the entire staff at the Physics Department.

CHAPTER 1

INTRODUCTION

Water at the near subsurface (tens of meters) is an essential resource for human needs and natural ecosystems. The need for water for agriculture and other activities are increasing. Also, natural hazards that involve water such as floods, drought and landslides are major natural treats to many countries (Entekhabi et al., 1999). Therefore, there is the need for soil water content measurements for management purposes. Huisman et al., (2003a) asserted that high-frequency electromagnetic techniques are the most promising category of soil water content sensors to fulfill this need because, this category contains a range of techniques that measure the same soil water proxy, namely dielectric permittivity, at different spatial scales. Ground Penetrating Radar (GPR), produces high frequency electromagnetic waves (MHz range), and has therefore been applied by many investigators to non-invasively explore soil water (Preko and Wilhem, 2012; Preko, 2007). Also, electrical resistivity is considered as a proxy for the spatial and temporal variability of many other soil physical properties (thus structure, water content, or fluid composition). The method is non-destructive and very sensitive hence it offers a very attractive tool for describing the subsurface properties without digging (Samouelian et al., 2005). In studying the changes of the subsurface resistivity with time, two dimensional resistivity imaging surveys are often repeated over the same line at different times. Such studies include the flow of water through the vadose zone and the changes in the water table due to water extraction (Barker and Moore, 1998).

GPR and electrical resistivity tomography (ERT) were therefore employed to assess the soil hydrological properties at Kwame Nkrumah University of Science and Technology (KNUST), Agricultural Research Station at Anwomaso – Kumasi for a period of three months.

1.1 Background to Research

Hydrologically, soil water is that component of water in the soil that may be evaporated from the soil by heating between 100 °C and 110 °C but usually 105 °C until there is no further weight loss (Gardner et al., 2001). In the vadose zone, soil water occurs under two classifications: bound and free water. Bound water refers to water molecules which are found in the first few molecular layers surrounding the soil particles. They are tightly held to the surface of the soil particles due to the influence of matric and osmotic forces (Baver et al., 1997). This water clings to the surface of the soil mineral grain so strongly that it does not flow under the influence of gravity and cannot be removed without destroying its structure. It is also not available to plant. This category of water comprises of capillary and adsorption water.

Water molecules located several molecular layers away are relatively free to move within the soil medium and are therefore referred to as free water. Free water is held solely by gravity and it is available to plants while serving as the main source of groundwater. Soil water occupies about 0.005 % of water on the earth surface (Schlesinger, 1997).

Soil water content is the amount of water a porous medium contains and is defined in most cases as the mass water content θ_m or the volumetric water content θ_v . It is therefore an important parameter for soil/water conservation, irrigation and agricultural management as well as in hydrological studies. It helps in identifying the appropriate time to apply irrigation water and in the right amount for consistently high yields.

1.2 Statement of Problem

A significant cause of low crop production and crop failure in rain fed agriculture in the tropic and sub-tropic regions is low and erratic rainfall. However, in many areas, crop and land

management do not necessarily optimize water flow along the rooting zones of the crop. Therefore, poor yields are more related to an insufficiency of soil moisture rather than to insufficiency of rainfall.

Also, excessive water application reduces yields by carrying nitrates below the depths of root penetration and by displacing soil air for a long time, thereby causing a lack of oxygen to the roots whereas water shortage also reduces yields due to drought stress.

For the hydrologist, the portioning of rainfall into infiltration, evaporation and runoff, depends on the soil water content and this has a large influence on soil erosion and river discharge. Recent studies have shown that including soil water content heterogeneity in spatially distributed hydrological models can improve discharge predictions (Merz and Plate, 1997; Merz and Bardossy, 1998; Pauwels et al., 2001). This makes soil water content estimation and monitoring for an area a very important exercise since it could help mitigate flood disasters, landslides, soil erosion and help in the appropriate management of water in irrigation and farming in general.

1.3 Research Objectives

The main aim of this research was to estimate the volumetric water content in the near surface (0.1m) with the Ground Penetrating Radar (GPR) under field conditions. The research was, however, conducted with the following specific objectives in mind:

- To validate the GPR technique as efficient and appropriate for soil water content estimation by comparing with time-lapse electrical resistivity measurements at the site.
- To determine the spatial and temporal variability of soil water content over a period.
- To determine the applicability of the resistivity method for imaging soil moisture.

1.4 Justification of Thesis

According to the World Bank in 2013, agricultural input to the GDP of Ghana has reduced from 41.55% in 2004 to 21.96% in 2013 as a result of climate change. In order to mitigate the effect of climate change and help in the appropriate management of water for good crop yields and better economic gains, it is important to monitor the soil water content in-situ on a field scale.

1.6 Structure of Thesis

The research work, consist of five chapters. The first chapter introduces the reader to the project where the following are considered;

- Background for the research
- Statement of the problem,
- Objective of the research and
- Justification of research

Chapter two (2) deals with the review of previous literature, and the theoretical background on which the research is based. This is intended to bring the reader up to date with most of the terms associated with the research.

The third chapter covers the research materials and methodology – the research was conducted with a combination of geophysical methods for data collection. A review of how and what was done in the field and at the desk are described in this chapter.

In chapter four (4), the research results and findings are presented and discussed. The fifth and final chapter presents the conclusions drawn and recommendations made from the research.

CHAPTER 2

LITERATURE REVIEW AND THEORETICAL BACKGROUND

2.1 Literature review

Surface water content is highly variable in both space and time. Variability of water content results from many processes acting over a range of temporal and spatial scales. The processes that determine the spatial water content variability include spatial heterogeneity of soil properties at different scales from centimeters (Ritsema, 1999) to kilometers (Jackson and le Vine, 1996), and lateral water redistribution at centimeters to tens or hundreds of meters under the influence of topography (Western et al., 1998). Temporal variability of water is often climatically determined; that is, the evaporation rate in the course of a year is a strong influence on the seasonal change of water content (Grayson et al., 1997). In summary, near surface water content is a function of spatially and sometimes temporal variables such as topography, precipitation, evapo-transpiration, geology and vegetation (Western et al., 1998). As such, collection of enough measurements to adequately capture the spatial distribution of water content can be challenging using conventional point measurements.

The measurement of space-time variation of surface water content status over a range of scales (centimeters to kilometers) is important in many research fields. For example, a correct description of the evolution of antecedent water content patterns can improve simulations in event-based hydrological modeling (Merz and Plate, 1997). Similarly, knowledge of space-time water content patterns is of key importance in solute transport modeling because of strong influence of water content on soil water fluxes (Ritsema and Dekker, 1998). Furthermore, the

space-time variation of surface water content can be used to extract information about physical properties and processes within the vadose zone (Ahuja et al., 1993; Hoeben and Troch, 2000).

Galagedara et al. (2003) opined that as yet, no efficient method has been developed to measure the variability of soil water content at the field or watershed scales, which is vital in applications that include agricultural water management and soil conservation.

The gravimetric method using soil samples is the standard and direct method for soil water content measurement. Field disturbance, intensive labour and inability to carry out repeat measurements are the main disadvantages of the gravimetric method (Galagedara et al., 2003). Time-domain reflectometry (TDR) has become the most widely used and accepted method for soil water content measurement (Topp et al., 1980, 1982; Whalley, 1993; Nielsen et al., 1973). However, the sample volume of TDR is restricted to a small cylindrical volume along the probe length (Nadler et al., 1991; Zegelin et al., 1992). Remotely sensed microwave radiations has also been used to estimate accurate soil water content below 0.1 m depth over a large area by Whalley and Bull (1991) and Whalley et al., (1991).

Many laboratory studies are often limited to a relatively small number of soil textures examined over a wide range of moisture content, contrasting with field sites having potentially many soil textures studied over a relatively narrow range of soil moistures. Additionally, these small-scale studies cannot easily address the heterogeneities in large scale natural systems or the variable resolution of geophysical measurements in heterogeneous systems with different scales of interest (Singha and Gorelick, 2006).

Theoretical, field and lab-based studies have documented that relationships exist between physical properties in the unsaturated zone (such as moisture content) and geophysical

measurements (Auerswald et al., 2001; Kalinski and Kelly, 1993; Kalinski et al., 1993; Mualem and Friedman, 1991; Titov et al., 2004). For example, Kalinski and Kelly (1993) were able to show excellent correlation between soil electrical resistivity and volumetric soil water content at the centimeter scale. However, there can be complicated relationships between resistivity and soil moisture which depends on mineralogy, soil structure, hydraulic properties, and soil chemistry (Abu-Hassanein et al., 1996; Rinaldi and Cuestas, 2002), and which are difficult to accurately replicate in the laboratory.

With the ever increasing need for soil water content measurement techniques that can provide dense and accurate measurements at an intermediate (field) scale, the ground penetrating radar (GPR) has been conceived as the natural intermediate-scale counterpart of TDR for soil water content measurements. Although the number of TDR applications has increased immensely in the past 20 years, the number of GPR applications for soil water content has only recently increased. Probably, the most important reason behind this delay is the more complicated behaviour of the unguided waves used in GPR as compared with waves guided by the TDR sensor. Furthermore, recent improvement in GPR technology allow more accurate travel time measurements, which are needed for soil water content determination with GPR (Huisman et al., 2003b)

There are several methods to measure volumetric water content with GPR, these include; surface reflection (Chanzy et al., 1996), reflection from groundwater table (van Overmeeren et al., 1997), and reflection from soil horizon (Weiler et al., 1998), but this work focuses on the velocity of ground wave, which is the wave directly travelling from the source to the receiving antenna through the top soil (Du and Rummel, 1994; Du, 1996). This particular wave is used

because it is the only wave with which the soil permittivity can be calculated from a single GPR measurement without knowledge of the depth of the reflecting layer (Huisman et al., 2003a).

Electrical resistivity tomography (ERT) also known as electrical resistivity imaging (ERI) is sensitive to changes in the subsurface resistivity distribution which is highly dependent on the degree of water saturation. Time-lapse ERT therefore has been used widely for environmental and hydrologic monitoring experiments (Mitchell et al., 2011). Daily et al. (1992) also tracked infiltration using time-lapse ERT measurements. Its field application makes it another valuable tool for near surface processes studies.

Therefore, this thesis discusses the use of the ground wave velocity and time-lapse resistivity measurements to determine the soil moisture content.

2.2 Background of Ground Penetrating Radar

Ground penetrating radar (GPR) is a geophysical mapping tool which employs a high-frequency (from 10 MHz to 2 GHz) electromagnetic pulse transmitted from a radar antenna to probe the earth. A transducer generates the electromagnetic wave and it is radiated from a transmitting antenna to a receiving antenna. The velocity of the wave travelling through the ground is determined by electrical properties (dielectric coefficient, conductivity and magnetic permeability) of the subsurface (Preko, 2007). The receiving antenna records the travel time and amplitude of the signal. Three types of waves are recorded (Figure 2.1). These are;

1. Airwave: part of the energy that travels through the air from transmitter to receiver
2. Direct ground wave: part of the energy that travels through the air-ground interface
3. Reflected wave: part of the energy that reaches the antenna after bouncing off a medium with contrasting electrical properties.

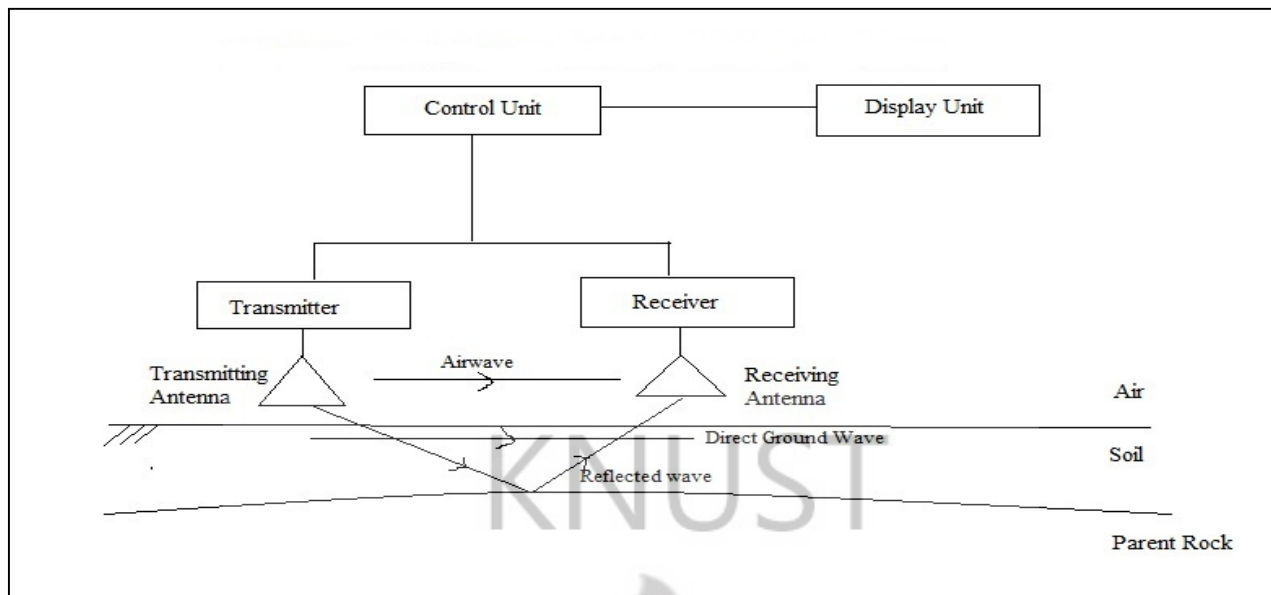


Figure 2.1: GPR setup and wave propagation

Normally, a GPR antenna emits succession of pulses of the same form and duration at definite intervals. The frequency around which most of the pulses' energy is concentrated is called the center frequency, f_c . GPR systems are generally planned to create a frequency bandwidth, d_f , which is similar to the center frequency, thus $d_f \sim f_c$. In the time interval between two successive pulses, the receiving antenna measures the electric field in the incoming pulse as an analogue signal, which is later amplified and converted to digital form. The interval at which the incoming signals are sampled is called the sampling interval (Basson, 1992).

In order to understand how the pulses propagate through the earth, the electromagnetic wave propagating through a medium is assumed to be non-magnetic with negligible losses. Also, for the purposes of this work, more attention would be placed on the direct ground wave.

2.2.1 Electromagnetic wave propagation

Electromagnetic waves are pulses which can travel through the vacuum of outer space and are created by the local disturbance in the electric and magnetic fields. When an alternating voltage

is applied to the antenna, dipole moments oscillate up and down on the antenna, corresponding to the current. The oscillating current creates oscillating electric (**E**) and magnetic (**H**) fields which in turn generate more electric and magnetic fields that moves perpendicular to each other. An outward propagating electromagnetic wave is created as a result and it moves perpendicular to both fields. The orientation is called the polarization (Figure 2.2).

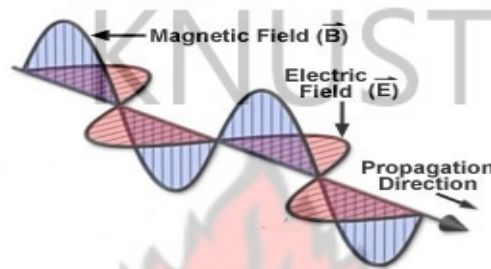


Figure 2.2: Schematic diagram of an electromagnetic wave

From its origin, the wave will propagate outwards in all direction. If the medium in which it is propagating (air for example) is the same everywhere, the wave will spread out uniformly in all directions. An electromagnetic wave transports its energy through vacuum at a speed of 3.0×10^8 m/s and this value is commonly represented by the symbol c .

When the electromagnetic wave passes over the conducting material, it will create an oscillating current in it. Therefore, the same design (dipole antenna) can be used to obtain signals from the air as is done with current in a circuit. The Antennas couple the current flowing in the wires into electromagnetic waves in air (Stratton 2007).

Generally, the propagation of an electromagnetic wave through a material medium occurs at a net speed that is less than 3.0×10^8 m/s. The mechanism for the transport of energy through a medium involves the absorption and reemission of the wave energy by the atoms of the material. When an electromagnetic wave impinges on the atoms of a material, the energy of that wave is

absorbed. The absorption of energy causes the electrons within the atoms to undergo vibrations. After a short period of vibrational motion, the vibrating electrons create a new electromagnetic wave with the same frequency as the first electromagnetic wave. While these vibrations occur for only a short time, they delay the movement of the wave through the medium. Once the energy of the electromagnetic wave is reemitted by an atom, it travels through a small region of space between atoms. When it reaches the next atom, the electromagnetic wave is absorbed, transformed into electron vibrations and then reemitted as an electromagnetic wave. While the electromagnetic wave will travel at a speed of c (3.0×10^8 m/s) through the vacuum of interatomic space, the absorption and reemission process causes the net speed of the electromagnetic wave to be less than c . The actual speed of an electromagnetic wave through a material medium is dependent on the optical density of the medium. Different materials cause different delays due to the absorption and reemission process. This is because, some materials have their atoms more closely packed and thus the distance between atoms is small. These factors (absorption and reemission) are dependent on the nature of the material through which the electromagnetic wave is travelling (Basson, 1992). Therefore, the speed of the electromagnetic wave is dependent on the material through which it is travelling.

2.2.2 Maxwell's Equations

Maxwell's equations describe the propagation of electromagnetic energy away from time-varying sources (current and charge) in the form of waves.

$$\nabla \times \mathbf{E} = -\frac{\partial B}{\partial t} \quad (2.1)$$

$$\nabla \times \mathbf{H} = J + \frac{\partial D}{\partial t} \quad (2.2)$$

$$\nabla \times \mathbf{D} = \rho \quad (2.3)$$

$$\nabla \times \mathbf{B} = 0 \quad (2.4)$$

The first equation (2.1) is Faraday's law of induction; the second equation (2.2) is Ampere's law that has been amended by Maxwell to include the displacement current $\partial D / \partial t$, the third (2.3) and fourth equations (2.4) are Gauss' law for the electric and magnetic fields. The displacement current term $\partial D / \partial t$ in Ampere's law is essential in predicting the existence of a propagating electromagnetic wave.

The four (4) equations are in SI units. The quantities \mathbf{E} and \mathbf{H} are the electric and magnetic field intensities and are measured in units of [V/m] and [A/m], respectively. The quantities \mathbf{D} and \mathbf{B} are the electric and magnetic flux densities and are in units of [C/m²], and [W/m²] or [tesla] respectively. \mathbf{D} is also called the electric current density, and \mathbf{B} , the magnetic induction. The quantities ρ and \mathbf{J} are the volume charge density and electric current density (charge flux) respectively of any external charges (not including any induced polarization charges and currents). They are measured in units of [C/m³] and [A/m³] respectively. The right-hand side of the fourth equation is zero because there are no magnetic mono-pole charges.

The charge and current densities may be thought of as the sources of the electromagnetic fields. For wave propagation problems; these densities are localized in space; for example, they are restricted to flow on an antenna. The generated electric and magnetic fields are radiated away from these sources and can propagate to large distances to the receiving antennas. Away from the sources in source-free regions of space, Maxwell's equation takes the simpler form;

$$\nabla \times \mathbf{E} = -\frac{\partial \mathbf{B}}{\partial t} \quad (2.5)$$

$$\nabla \times \mathbf{H} = \frac{\partial \mathbf{D}}{\partial t} \quad (2.6)$$

$$\nabla \times \mathbf{D} = 0 \quad (2.7)$$

$$\nabla \times \mathbf{B} = 0 \quad (2.8)$$

Equations 2.5 – 2.8 are source-free Maxwell equations.

Also, from Ohms law; for dielectrics and conductors,

$$\mathbf{J} = \sigma \mathbf{E} \quad (2.9)$$

where σ is the conductivity of the material (Stratton, 2007).

2.2.3 Constitutive Relations

The electric and magnetic flux densities \mathbf{D} and \mathbf{B} are related to the field intensities \mathbf{E} and \mathbf{H} by the constitutive relations, whose precise form depends on the material in which the field exists. In the absence of magnetic or dielectric materials, the constitutive relations take their simplest form;

$$\mathbf{D} = \epsilon_0 \mathbf{E} \quad (2.10)$$

$$\mathbf{B} = \mu_0 \mathbf{H} \quad (2.11)$$

where ϵ_0 and μ_0 are the permittivity and permeability of free space, with numerical values; 8.854×10^{-12} F/m and $4\pi \times 10^{-7}$ H/m, respectively.

For simple homogeneous isotropic dielectric and magnetic materials;

$$\mathbf{D} = \epsilon \mathbf{E} \quad (2.12)$$

$$\mathbf{B} = \mu \mathbf{H} \quad (2.13)$$

where ϵ and μ are the permittivity and permeability of the material respectively. These two (permittivity and permeability) are related to the electric and magnetic susceptibilities as follow;

$$\epsilon = \epsilon_0(1 + \chi) \quad (2.14)$$

$$\mu = \mu_o(1 + \chi_m) \quad (2.15)$$

where χ and χ_m are electric and magnetic susceptibilities, respectively (Takahashi et al., 2012).

For non-magnetic materials, the relative permeability μ_r , which is the ratio of the permeability of a specific medium to the permeability of free space, μ_o equals 1. This implies μ equals μ_o .

The relative permittivity ϵ_r or the dielectric constant (**K**) which is the ratio of the amount of electrical energy stored in a material by an applied voltage, relative to that stored in vacuum is

given by:

$$\epsilon_r = \frac{\epsilon}{\epsilon_0} = (1 + \chi) \quad (2.16)$$

The refractive index **n** of such a material is therefore given by;

$$n = \sqrt{(\mu_r \epsilon_r)} \quad (2.17)$$

The refractive index **n**, which describes how the wave propagates through the medium is also

given by;

$$n = \frac{c}{v} \quad (2.18)$$

where **v** is the velocity of the wave propagating through the medium

Radar velocities are controlled by the relative permittivity (dielectric constant) and conductivity of the subsurface. Velocity of the radar wave (**v**) is given by:

$$v = \frac{c}{\sqrt{(\mu_r \epsilon_r)}} = \frac{c}{\sqrt{\epsilon_r}} \quad (2.19)$$

where **c** is the velocity of light in a vacuum, μ_r , is the relative magnetic permeability (close to unity (1) for non-magnetic rocks and materials), and ϵ_r , the relative dielectric permittivity (Kearey et al., 2002).

Hence, for non-magnetic materials

$$\epsilon_r = \frac{c^2}{v^2} \quad (2.20)$$

2.2.4 The Physical Properties of soil

As mentioned earlier, the electric and magnetic properties of a medium influence the propagation of the electromagnetic waves. These properties are dielectric permittivity, electric conductivity and magnetic permeability (Jol and Bristow, 2003).

Dielectric permittivity describes the ability of a material to store and release electromagnetic energy in the form of electric charge. Permittivity influences the electromagnetic waves propagation greatly in terms of velocity, intrinsic impedance and reflectivity. In natural soils, dielectric permittivity might have a greater influence than electric conductivity and magnetic permeability (Lampe and Holliger, 2003).

Soil can be regarded as a three-phase composite with soil matrix and pore spaces filled with air and water. The pore-water phase of the soil can be divided into free and bound water (restricted in mobility by absorption to the soil matrix surface). The relative permittivity (dielectric constant) of air is 1 and between 2.7 - 10 for common minerals in soils and rocks (Ulaby et al., 1986). Water, however, has a relative permittivity of 81, depending on the temperature and frequency. Therefore the permittivity of water-bearing soils is strongly influenced by its water content (Robinson et al., 2003). Hence, by analyzing the dielectric permittivity of soil measured with GPR, the water content can be investigated.

The presence of ferrimagnetic minerals in the soil gives soils their magnetic properties. These minerals, mainly magnetite, titanomagnetite and maghemite, either stem from the parents rocks or are formed during soil genesis. The magnetic properties, as mentioned earlier, influence the propagation of electromagnetic waves. However in natural soils, the influence of the magnetic properties of the soil is low and negligible. The magnetic permeability must be extremely high to influence the GPR signal. For example, Cassidy (2009) asserted that magnetic susceptibility

must be greater than $30,000 \times 10^{-5}$ SI to have an influence similar to dielectric permittivity. Soils exhibiting such high magnetic susceptibilities are very rare. Although soils in the tropics display such high susceptibilities, magnetic susceptibilities in this range are exceptional (Preetz et al., 2008). Therefore, the magnetic susceptibility of most soils is assumed to be the same as that of free space.

Electric conductivity describes the ability of a material to pass free electric charges under the influence of an applied field. The primary effect of conductivity on electromagnetic waves is loss of energy. In highly conductive materials, the electromagnetic energy is lost as heat (Takahashi et al., 2012). Hence, the electromagnetic wave cannot propagate deep. The conductivity of soils is increased with increasing water, soluble salts and clay content. Therefore, GPR is ineffective in highly conductive materials such as those under saline conditions or with high clay content (Cassidy, 2009).

2.2.5 Topp's Model

One of the most popular models that provides the dielectric permittivity of soil is an empirical model called Topp's equation (equations 2.21 and 2.22) which describes the relationship between relative permittivity ϵ_r and volumetric water content (θ_v) of soil (Topp et al., 1980):

$$\epsilon_r = 3.03 + 9.3\theta_v + 146\theta_v^2 - 76.6\theta_v^3 \quad (2.21)$$

$$\theta_v = -5.3 \times 10^{-2} + 2.92 \times 10^{-2}\epsilon_r - 5.5 \times 10^{-4}\epsilon_r^2 + 4.3 \times 10^{-6}\epsilon_r^3 \quad (2.22)$$

The model is often considered inappropriate for clays and organic-rich soils, but it agrees well for sandy and loamy soils over a wide range of water contents (5-50%) in the GPR frequency range (10 MHz – 1 GHz). The model, however, does not account for the imaginary component of permittivity.

2.2.6 GPR ground wave

GPR ground waves are boundary waves that are created by the contrast in electromagnetic velocity between air and near-surface materials. The ground wave travels at a velocity (v) determined by the properties of the near surface materials. For agricultural applications, the near surface material is usually soil, and water content typically has the most influence on the velocity of unsaturated soils (Sperl, 1999).

2.2.7 Data collection modes for GPR

There are two (2) common collection modes for surface GPR data, and data obtained from these modes can be used to calculate the ground wave velocity. The most frequently used mode is the common-offset (CO) profiling, where the transmitting and receiving antennas are kept a fixed distance apart and are pulled in parallel along the ground.

CO profiling produces a series of measurements along a profile. For the ground wave, the travel time and amplitude measurements recorded at each location are effective values over the area approximately represented by the antenna separation distance and the depth of influence. The electromagnetic velocity of the ground wave for each CO location can be calculated by dividing the separation distance of the antennas by the measured travel time of the ground wave from the transmitter to the receiver (Galagedara, 2003).

Another data collection mode for surface GPR data is variable-offset profiling, in which the separation distance between the transmitter and receiver is increased evenly. For variable-offset data, the ground wave velocity is calculated by observing the changes in the ground wave arrival time as the antenna separation increases (Weihermuller et al., 2007).

One form of variable-offset profiling is common-midpoint (CMP) surveys, in which the transmitter and receiver are each moved further apart by a constant increment for each new measurement. The other type of variable-offset profiling is wide angle reflection and refraction (WARR) surveys, where one antenna is kept stationary while the other antenna is moved one distance increment for each new measurement (Grote et al., 2003).

2.2.8 Penetration depth

The penetration depth is controlled by the GPR antenna frequency, the electrical conductivity and the attenuation of the subsurface deposits. The depth of influence, z , of the ground wave, ie the thickness of the zone between the surface of the ground and the maximum penetration depth of the ground wave, is not distinctly defined and different researchers present varying formulae to quantify it. The depth is expressed as a function of wavelength of the GPR signal and it is dependent on the volumetric water content (VWC) of the soil (Du and Rummel, 1996; Grote et al., 2003).

2.2.9 Attenuation

Radio waves do not penetrate far through soils and rock. Several processes lead to a reduction of the electromagnetic signal strength. Among the most important processes are attenuation, spherical spreading of the energy, reflection or transmission losses at interfaces and scattering of energy. Special attention will be given to the attenuation, which is a function of dielectric permittivity, (ϵ) , magnetic permeability, (μ) , and electrical conductivity, (σ) , as well as the frequency of the signal itself, $\omega = 2\pi f$, where f is the frequency and ω is angular frequency (Du, 1996).

Generally, attenuation (L) is the loss of the signal's amplitude with increasing propagation distance.

$$L = \alpha d \quad (2.23)$$

where d is the propagation distance and α , the attenuation coefficient in [dB/km].

The attenuation coefficient is expressed as;

$$\alpha = \omega \sqrt{\epsilon \mu \frac{\sqrt{1 + (\sigma / \omega \epsilon)^2} - 1}{2}} \quad (2.24)$$

In low-loss materials, where $\sigma / \omega \epsilon \approx 0$, the attenuation coefficient is reduced to

$$\alpha = \frac{\sigma}{2} \sqrt{\frac{\mu}{\epsilon}} \quad (2.25)$$

The attenuation is proportional to the electrical conductivity, which leads to high attenuation in materials with high electrical conductivity as shown in table 2.1.

Table 2.1: Electrical properties of geological materials (Davis and Annan, 1989)

Material	Dielectric constant (K)	Conductivity [mS/m]	Velocity [m/ns]	Attenuation [dB/m]
Air	1	0	0.3	0
Distilled water	80	0.01	0.033	0.002
Fresh water	80	0.5	0.033	0.1
Sea water	80	30,000	0.01	1,000
Dry sand	3-5	0.01	0.15	0.01
Saturated sand	20-30	0.1-1.0	0.06	0.03-0.3
Limestone	4-8	0.5-2	0.12	0.4-1
Shale	5-15	1-100	0.09	1-100
Silt	5-30	1-100	0.07	1-100
Clay	4-40	2-1,000	0.06	1-300
Granite	4-6	0.01-1	0.13	0.01-1
Salt (dry)	5-6	0.01-1	0.13	0.01-1
Ice	3-4	0.01	0.16	0.01

2.3 Background of Electrical resistivity

The main aim of electrical resistivity surveys is to determine the subsurface resistivity distribution by taking measurements on the ground surface. The true resistivity of the subsurface can be estimated from these measurements (Loke 2000).

2.3.1 Electrical Resistivity theory

The property of a material that resists the flow of electrical current is termed resistivity. It describes a material's ability to transmit electrical current that is independent of the geometrical factors. Electrical resistivity is a function of a number of soil and rock properties; including the nature of the solid constituents (particle size distribution, mineralogy), arrangement of voids (porosity, pore size distribution, connectivity), degree of water saturation (water content), resistivity of the fluid (solute concentration) and temperature. Archie's law relates the resistivity of the earth to the resistivity of the pore fluid in relation to porosity and saturation of rocks as;

$$\rho = a\rho_w\phi^{-m}S^n \quad (2.26)$$

where ρ and ρ_w are the effective rock resistivity and the resistivity of groundwater respectively; ϕ is the porosity, S is the volume fraction of pores with water, a , m and n are constants with $n = 2$, $1.3 \leq m \leq 2.5$ and $0.5 \leq n \leq 2.5$ (Archie, 1942).

The resistivity of an ideal cylinder of length L and cross-sectional area A with uniform composition is given by;

$$\rho = \frac{RA}{L} \quad (2.27)$$

The resistivity appears as the material-specific constant of proportionality in the expression for the total resistance of the cylinder. The total resistance, R , may be obtained experimentally through Ohm's law;

$$V = IR \quad (2.28)$$

where V is the potential difference between the ends of the cylinder and I is the total current flowing through the cylinder. The resistivity of the material, which is an intrinsic property of the material, is then related to experimentally measured extrinsic parameters by;

$$\rho = R_{app}K = \left(\frac{V}{I}\right)\left(\frac{A}{L}\right) \quad (2.29)$$

where R_{app} or (V/I) is the apparent resistance and K or (A/L) is the geometric factor that carries information about the geometry of the material. However, it is extremely difficult to arrive at an expression for the resistivity of material that is not as geometrically simple as the uniform cylinder (Keary et al 2002).

Electric current flows through rocks and soils in three ways namely; electronic (ohmic), electrolytic and dielectric conduction. The current flow line distribution depends on the medium being investigated (Figure 2.3). Electrical equipotential are hemispherical in a homogenous and isotropic half-space when the current electrodes are located at the soil surface.

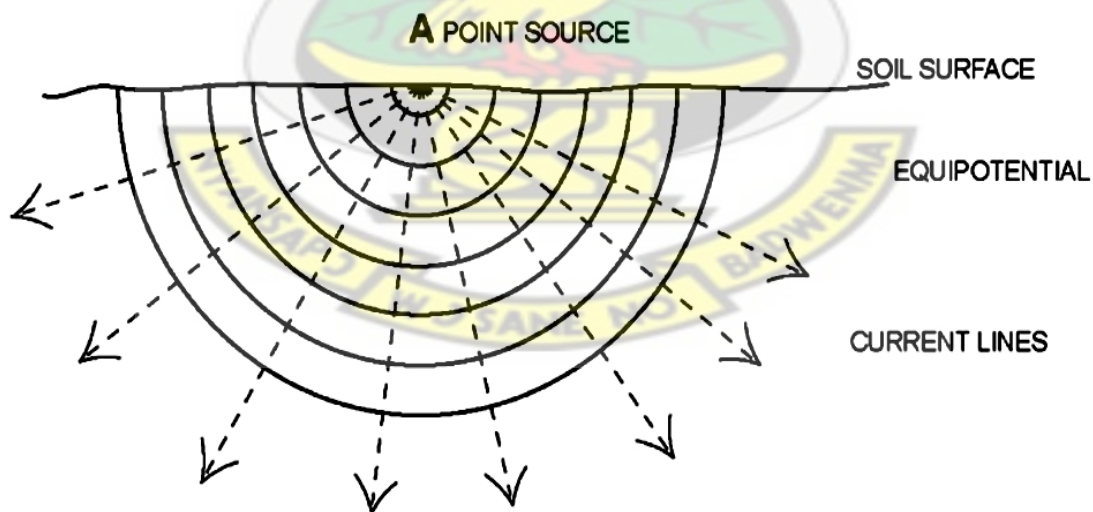


Figure 2.3: Current flow from a point source (Kearey et al., 2002).

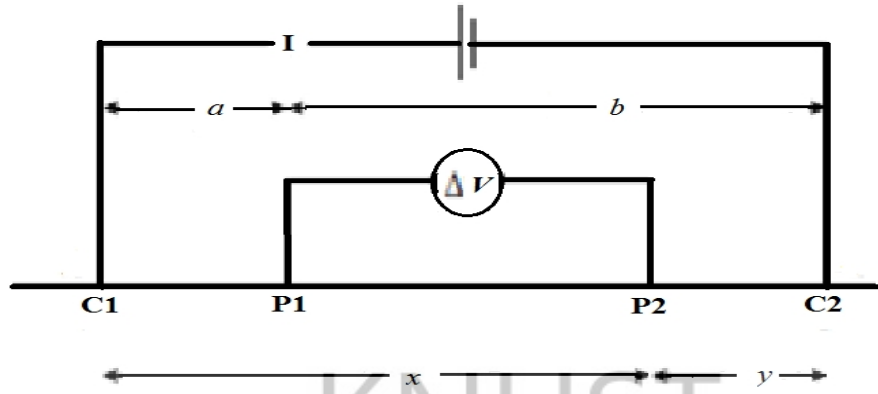


Figure 2.4: Electrical resistivity measurement setup

Electrical resistivity measurements usually require 4 electrodes (Figure 2.4): 2 electrodes namely C1 and C2 are used to inject the current (I), and 2 other electrodes called P1 and P2 are used to record the resulting potential difference. The potential difference ΔV measured between the potential electrodes P1 and P2 is given by the equation;

$$\Delta V = V_{P1} - V_{P2} = \frac{\rho I}{2\pi} \left[\left(\frac{1}{a} - \frac{1}{b} \right) - \left(\frac{1}{x} - \frac{1}{y} \right) \right] \quad (2.30)$$

Thus,

$$\rho = \frac{2\pi\Delta V}{I \left[\left(\frac{1}{a} - \frac{1}{b} \right) - \left(\frac{1}{x} - \frac{1}{y} \right) \right]} \quad (2.31)$$

Where the ground is uniform, the resistivity calculated from the equation of resistivity ρ above, should be constant and independent of both electrode spacing and surface location. When subsurface inhomogeneities exist, the resistivity will vary with the relative positions of the electrodes. Any computed value is then known as the apparent resistivity ρ_a and is the function of

the form of the inhomogeneities. In the homogenous ground, the depth of current penetration increases as the separation of the current electrodes is increased (Kearey et al., 2002).

Resistivity is one of the most variable physical properties ranging between $1.6 \times 10^{-8} \Omega\text{m}$ for native silver to about $10^{16} \Omega\text{m}$ for pure sulphur. Table 2 shows the resistivity of some rocks and earth materials.

Table 2.2: Resistivity of earth materials (Loke, 2011)

Material	Resistivity [Ωm]
Igneous and Metamorphic rocks	
Granite	$5 \times 10^3 - 10^6$
Basalt	$10^3 - 10^6$
Slate	$6 \times 10^2 - 4 \times 10^7$
Marble	$10^2 - 2.5 \times 10^8$
Quartzite	$10^2 - 2 \times 10^8$
Sedimentary Rocks	
Sandstone	$8 - 4 \times 10^3$
Shale	$20 - 2 \times 10^3$
Limestone	$50 - 4 \times 10^2$
Soils and waters	
Clay	1 - 100
Alluvium	10 - 800
Groundwater (fresh)	10 - 100
Sea water	0.2

2.3.2 Configurations of Electrical Resistivity surveys

One of the new developments in recent years is the use of 2D electrical imaging/tomography surveys to map the subsurface resistivity variations (Aning et al., 2014). Such surveys are usually carried out using a large number of electrodes, 25 or more, connected to a multi-core cable. An electronic switching unit is used to automatically select the relevant four electrodes for each measurement. Normally a constant spacing between adjacent electrodes is used.

In practice, the arrays that are most commonly used for 2D imaging surveys are the

- (a) Wenner array
- (b) Dipole-dipole array and
- (c) Schlumberger array

(a) Wenner Array; this is good in resolving vertical changes, but relatively poor in detecting horizontal changes. Also, for the Wenner array, the median depth of investigation is approximately 0.5 times the “a” spacing used. Compared to other arrays, the Wenner array has a moderate depth of investigation. The signal strength is inversely proportional to the geometric factor used to calculate the apparent resistivity value for the array. For the Wenner array, the geometric factor is given by $2\pi a$ which is smaller than the geometric factor for other arrays (Loke 2000). Among the common arrays, the Wenner array has the strongest signal strength (Figure 2.5a).

(b) Dipole-dipole; this array (Figure 2.5b) is used in resistivity surveys because of low E.M coupling between the current and potential circuits. This array is most sensitive to resistivity changes between the electrodes in each dipole pair. This means that, the dipole-dipole array is very sensitive to horizontal changes in resistivity, but relatively insensitive to vertical changes in the resistivity. The geometric factor for this array is given by $\pi n (n+1) (n+2) a$.

(c) Schlumberger; this array (Figure 2.5c) is moderately sensitive to both horizontal and vertical structures. The median depth of investigation for this array is about 10% greater than that for the Wenner array for the same distance between the outer (C1 and C2) electrodes. The signal strength for this array is smaller than that for the Wenner array, but it is higher than the dipole-dipole array. The geometric factor is given by $\pi n (n+1) a$.

Figure 2.5 shows the electrode configuration for the various arrays.

Among the characteristics of an array that should be considered are

- (i) The sensitivity of the array to vertical and horizontal changes in the subsurface resistivity,
- (ii) The depth of investigation,
- (iii) The horizontal data coverage and
- (iv) The signal strength

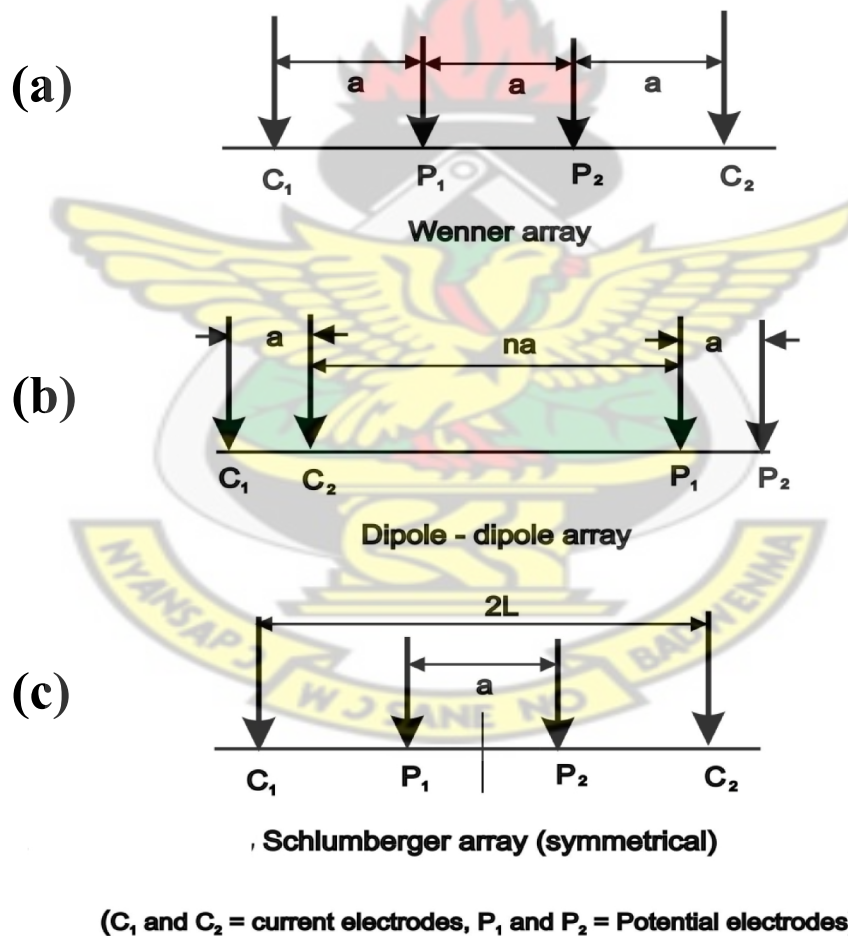


Figure 2.5: Electrode configuration for the various arrays

The geophysical techniques discussed in this chapter provide the basis for this work. For the Ground Penetrating Radar, the ease with which the ground wave velocity can be calculated using the constant offset (CO) mode of measurement makes it ideal for soil water estimation by means of the Topp's model. The Wenner array of the electrical resistivity technique is the best choice for the research as the method is very good in resolving vertical changes in resistivity and provides good resolution data at the near subsurface (Loke 2000).



CHAPTER 3

MATERIALS AND METHODS

3.1 Project Site

The site for the project is an 82×24 m oil palm plantation at the KNUST Agricultural Research Station at Anwomaso near Kumasi. It is centered on latitude $6^{\circ} 42' 00''$ N and longitude $1^{\circ} 32' 00''$ W. Figure 3.1 shows the location of the project site.

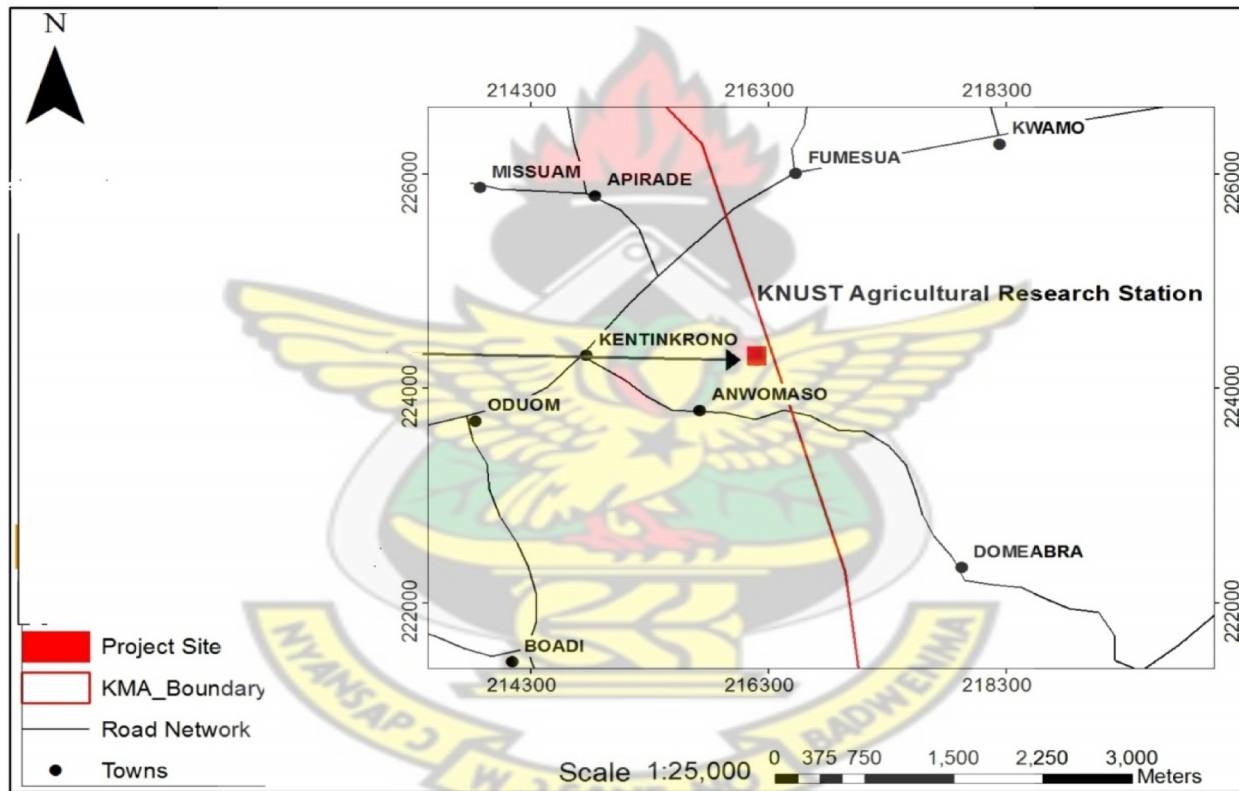


Figure 3.1: Project site location

3.1.1 Topography

The project site has a gentle slope in the west-east direction. Figure 3.1 shows a contour map of the research site with topographic variations across the site.

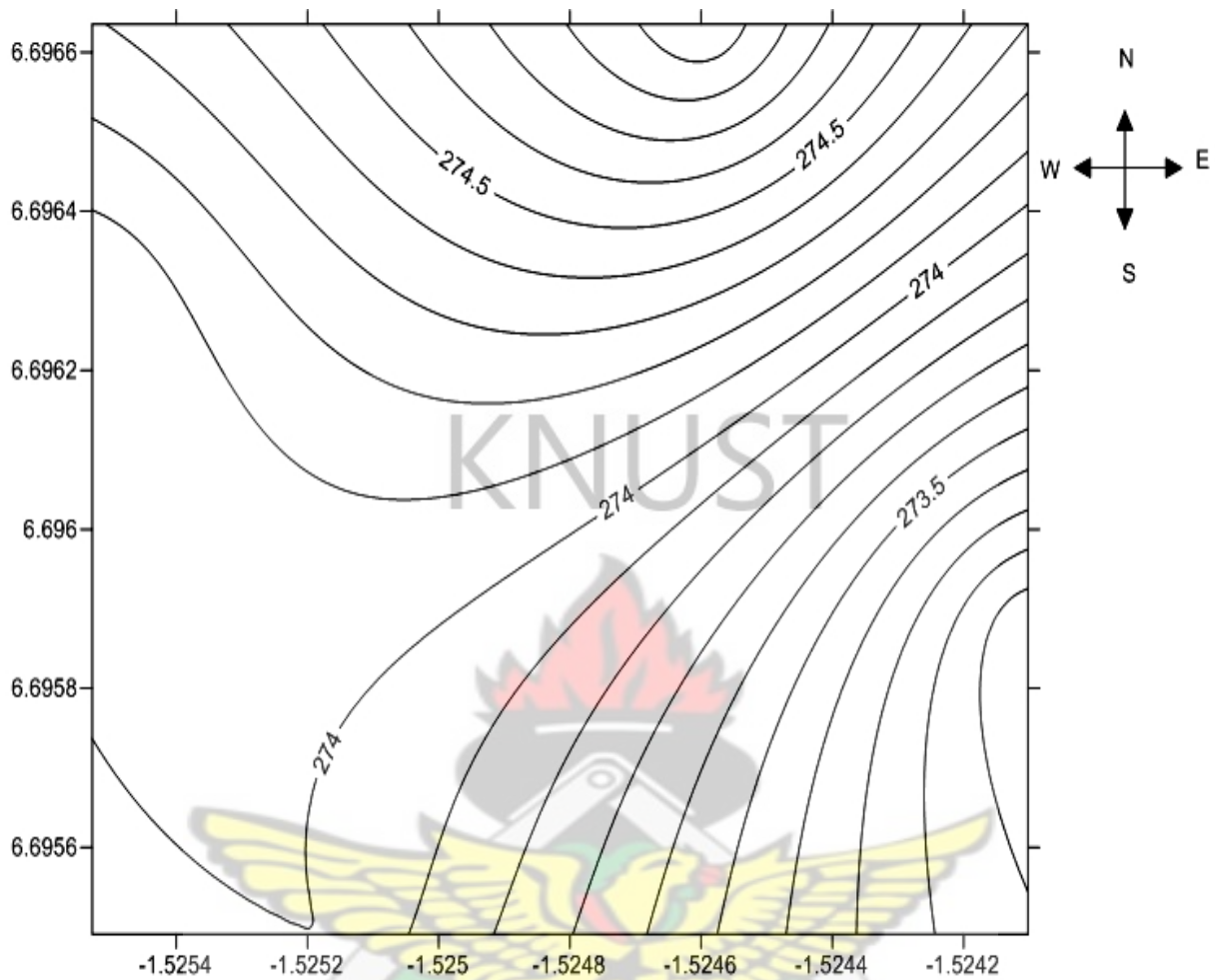


Figure 3.2: Topography of research site

3.1.2 Geology of site

The Project site is within the Kumasi Metropolis (KMA). The geology of the KMA (Figure 3.3) is characterized by middle Precambrian rocks. These rocks are constituents of the Kumasi Basin. The Kumasi Basin covers the entire area between the Ashanti Belt on the east and the Sefwi Belt on the west. It is dominated by very thick sequences of poorly exposed Birimian metasediments and small to very large granitoid complexes of the basin type (Griffis et al., 2002). Ages for the Birimian metasediments and metavolcanics in Ghana generally fall within the range of 2150-2200 Ma (Davis et al., 1994).

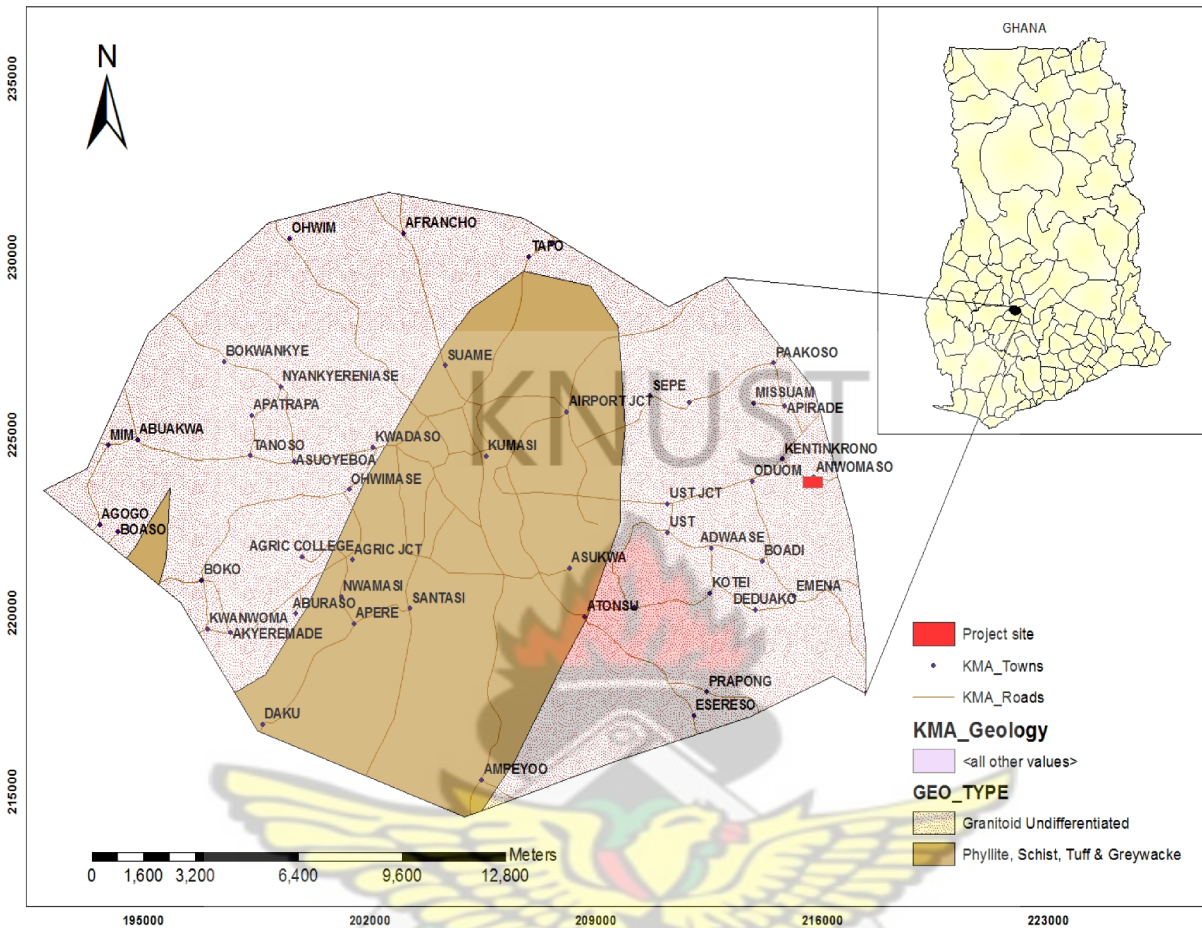


Figure 3.3: Geological map of Kumasi Metropolis (Geological Survey Department, 2009)

Hirdes et al. (1992) adopted a lithofacies scheme of geological mapping that recognized a variety of metamorphosed sedimentary facies in the basin. The facies range from distal argillites in the central portion of the basin to wackes, volcanoclastics and chemical sediments, which are more widespread along the margins of the basins and adjacent volcanic belts. The vast Kumasi granitoid complex (Kesse, 1985) dominates the northern portion of the basin whereas the large Ankasa plutonic complex covers a large area in the southern part of the basin.

The biotite, (hornblende, muscovite) granitoids which are undifferentiated make up the geology for the project site and are 2104 ± 1 Ma in age.

3.1.3 Soil

The texture of the soil across the site varies from sandy loam to clay loam, with the most common textures being sandy loam and sandy clay loam.

3.1.4 Climate

The site for the project falls within the wet sub-equatorial climate. The average minimum temperature is about 21.5°C and a maximum average temperature of 30.7°C. The average humidity is about 84.16 % at 0900 GMT and 60 % at 1500 GMT.

However, for the period of work between June and September, 2013, the average minimum temperature recorded was about 13.75°C and a maximum average temperature of 19°C. The average highest rainfall was recorded in July as 111 mm and lowest in June as 48 mm (www.worldweatheronline.com retrieved on 14th January 2014).

3.1.5 Vegetation

The project site falls within the moist semi-deciduous South-East ecological zone with the predominant species of trees there being Ceiba, Triplochlon, Celtis and Exotic Species. (<http://kma.ghanadistrict.gov.gh> retrieved 20th October, 2014).

3.1.6 Land Use

The land at the site is used for agricultural activities such as the cultivation of oil palm, maize, citrus and vegetables. Other activities include the rearing of poultry and other livestock.

3.2 Data Acquisition

In order to accurately estimate and monitor the soil water content, two (2) different geophysical methods were used. These are the ground penetrating radar (GPR) and the time-lapse electrical resistivity techniques.

The measurements took place between 17th June 2013 and 3rd September 2013. Measurements were taken daily from Monday to Friday till the 22nd of July 2013 where an interval of 2 days was used thereafter.

The GPR data was taken along four (4) established traverses 82 m in length and separated by 8 m. The profile lines run West-East. Figure 3.4 shows the layout of the profile lines at the project site. The resistivity data was also taken along 80 m of the established traverses (lines). Figure 3.4 shows the profile lines at the site.

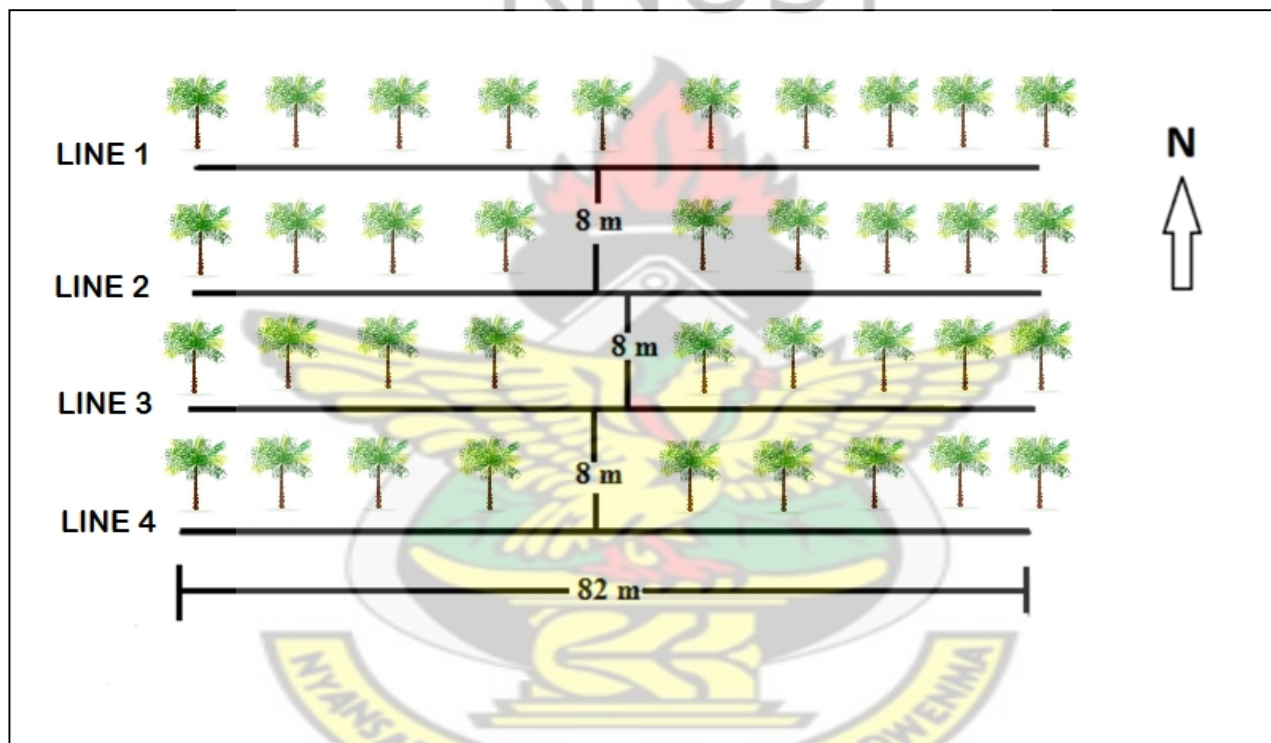


Figure 3.4: Profile lines at project site

3.2.1 Ground Penetrating Radar Measurements

The MALA GPR system was used for the collection of the GPR data at the site. The system includes a monitor, control unit and 200 MHz antennas (Figure 3.5).

The MALA monitor is a dedicated data acquisition platform with a unique user interface designed for the MALA GPR Systems. It is simple, intuitive and easy to navigate and use. The

monitor is equipped with a unique dual function turn/push button for system operation thereby making additional keyboards or mouse unnecessary.

The MALA ProEx Control Unit is a fast acquisition, processing and storage device. The MALA ProEx controller was the first, and still the only, controller available with parallel processors. While most GPR controllers use interleaved processing power to collect and process multi-channel data, MALA ProEx uses a separate processor to handle each data stream. Ethernet communications between the MALA ProEx Control Unit and the MALA XV Monitor or a notebook PC ensure safe and reliable data transfer at high speed.

The MALA ProEx Optical Module allows the connection of all MALA GPR antennas that utilize an optical interface. This includes MALA shielded, unshielded, rough terrain antenna (RTA) and borehole antennas.

The MALA 200 MHz unshielded antenna is a low frequency antenna which gives mid-range penetration depth of up to 10 m with good resolution. The compactness of the antenna facilitates surveys in more vegetated terrain since minimal noise (unwanted externally generated electromagnetic waves) would not be encountered in the farm.

A specially made wooden cart was used for the work (Figure 3.7). The cart was made of wood because unlike metals and other conductive materials, wood has very little effect on the electromagnetic waves being transmitted from the antenna. The design was such that it had two wheels in front and two at the rear. The antennas were mounted on the cart at a short distance from the ground and about 1.2 m apart. Locks on the cart aided in fixing the antennas to the wood. The wooden cart was made to facilitate movement of the GPR system on the field and to aid in acquiring consistent data since the distance from the antennas to the ground was kept constant.

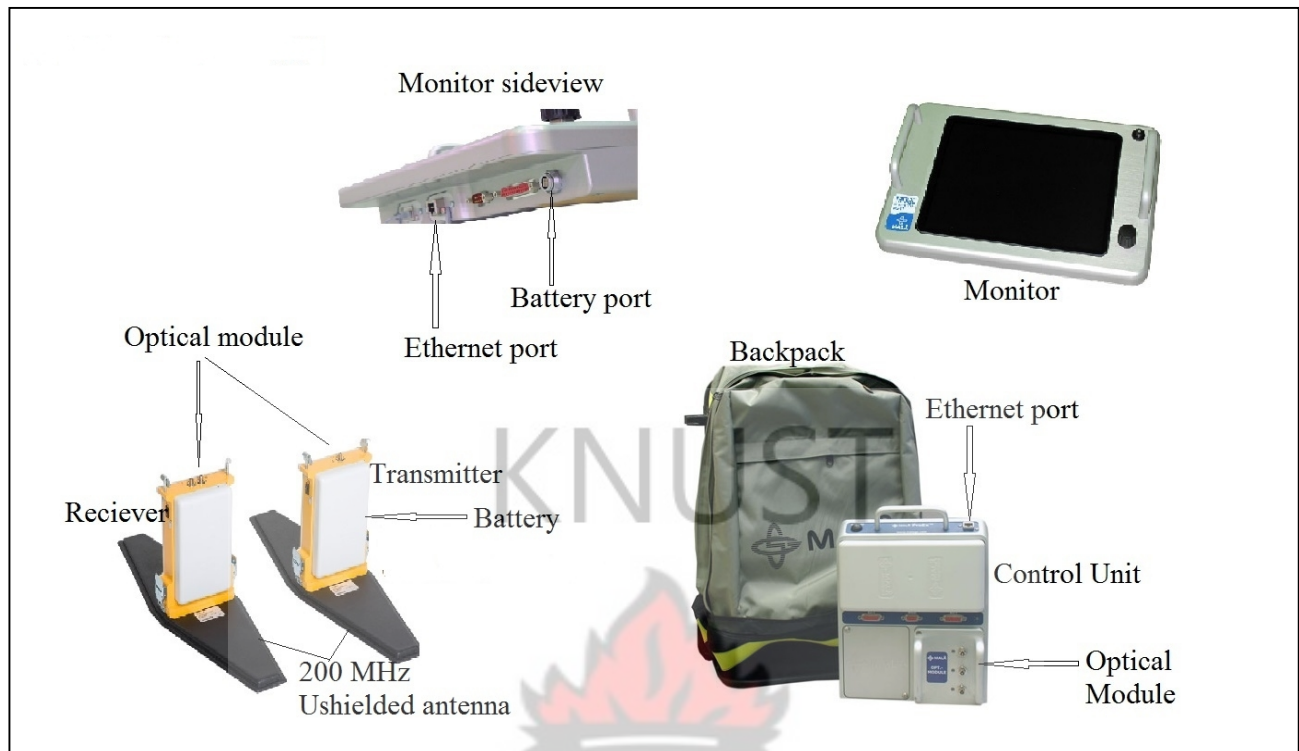


Figure 3.5: The Mala GPR system

3.2.2 Field Procedures

The various units of the system were assembled by means of cable connectors. The monitor was connected to a 12 V battery via the battery port. The antennas and control unit obtained their power supply through attached batteries. The control unit and the monitor establish a link via the Ethernet ports and the antennas connected to the control unit through the optical module using fibre optic cables.

The transmitting and receiving antenna were held strongly by the wooden slab separated by 1.2 m and 12 cm above the ground. The antennas were fixed at 1.2 m apart because this was the optimum distance for the detection of the ground wave. The small distance from the ground was to enable the receiving antenna to record effectively. The transmitter was kept at the rear with the receiver in front. The power button on all the units was pushed after the connections. Some time was allowed for the antennas to warm up and during this period, the survey parameters were set.

The survey parameters were set using the interface on the monitor (Figure 3.6). The survey parameters for this work were set as follows; Acquisition mode: Time triggering, Maximum time window: medium, Time window: 34.3 ns (1.99 m, 64 smp), Velocity: 100 m/ μ s, Time interval: 1.0 s, Sampling frequency: 989.92 MHz. The sampling interval which referred to the rate at which the signals reaching the receiver was sampled usually depends on the frequency of the transmitter. A sampling interval equal to the inverse of the sampling frequency was therefore used. The time length between two transmitted pulses for which the reflections were recorded is called the time window.

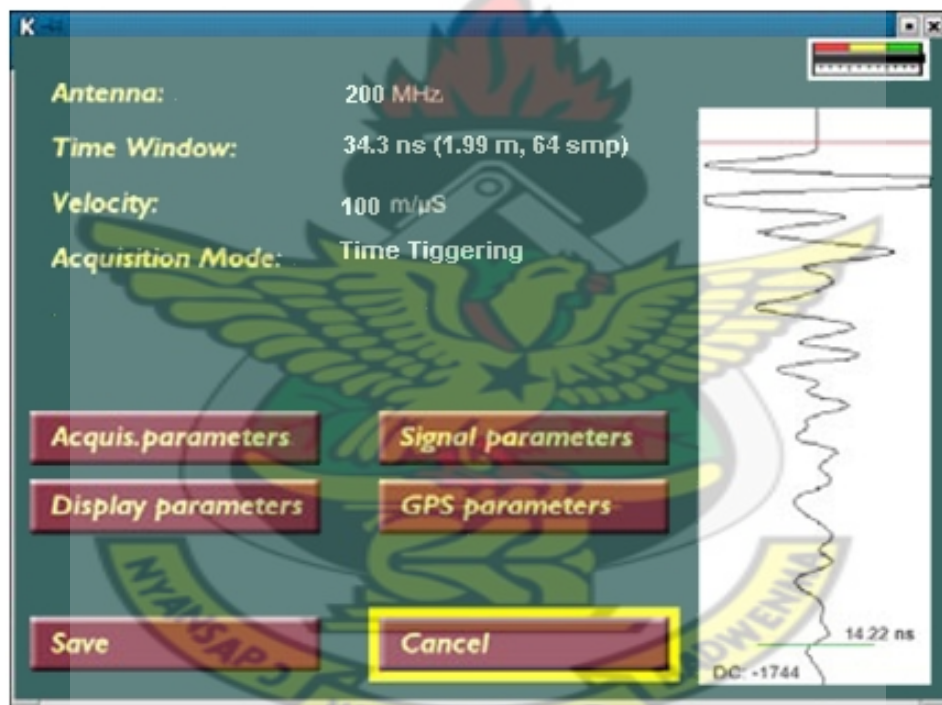


Figure 3.6: Monitor Interface; settings

The control unit receives the survey parameters from the interface and generates the timing signals for the transmitter and receiver. It also receives the data from the receiver and does the initial processing before sending it to the storage device.

On the command of the control unit, the transmitter generated electromagnetic pulse that was emitted through the transmitting antenna connected to it.

The transmitting antenna determined the central frequency and bandwidth of the signal that was sent into the ground. The antenna attached to the receiver intercepts the energy and sends it to the receiver where it was amplified, digitized and sent to the control unit.

Traces which are time versus amplitude graphs were then plotted on the monitor screen. The command to the control unit was sent at the start of measurements along each profile line and another sent at the end of the profile line to stop measurements.

Data was collected at an interval of 1 cm along each profile line as the wooden cart was moved (Figure 3.8), such that the traces could be plotted side by side creating a pseudo-section through the ground. The GPR data was displayed on the monitor during acquisition and stored automatically.

In taking the data, the common offset mode of acquisition was used as the transmitting and receiving antennas distance were kept constant throughout. This was done for 32 days over the four (4) profile lines from 17th June to 3rd September 2013.

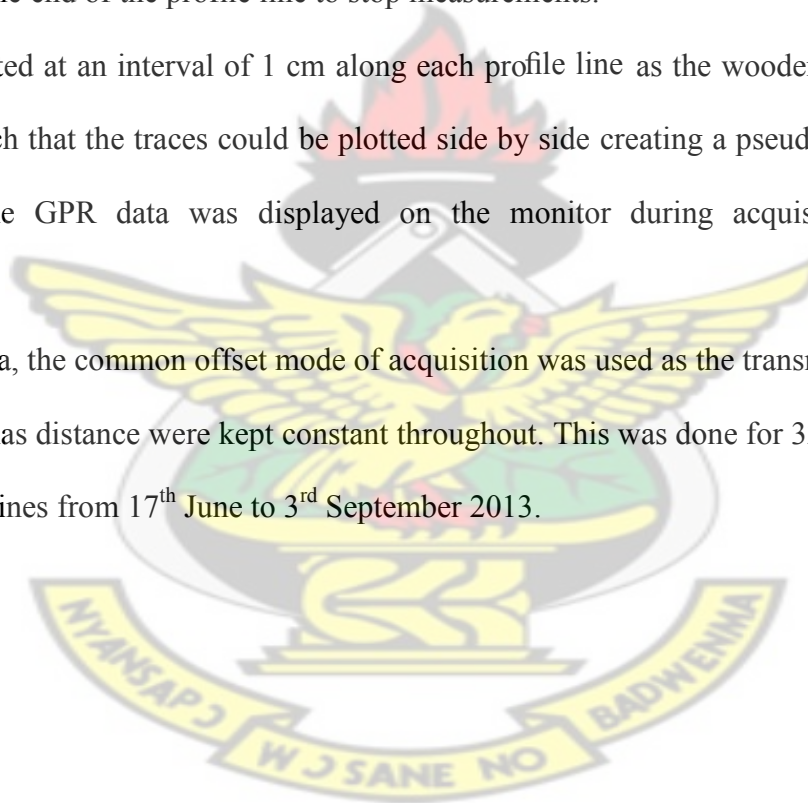




Figure 3. 7: GPR setup showing wooden cart (A), transmitter (B) and receiver (C)



Figure 3.8: Data acquisition; moving cart along profile lines

3.2.2 Time-Lapse Electrical Resistivity Measurement

Resistivity imaging surveys are not only spatial but also temporal. A simple experiment was used to map the distribution of soil moisture at the site. For the time-lapse resistivity measurements, electrical resistivity tomography (ERT) was repeated over the four lines from the 9th of July 2013 to 26th August 2013.

The multi-electrode ABEM Lund Resistivity Imaging System was used to carry out the electrical resistivity measurements on the 4 parallel profiles 80 m in length (Figure 3.4). The system operated automatically once the geometrical parameters (array type, electrode separation and minimum current) were set and electrode check was successful. The electrode check was to make sure that all the electrodes were properly functioning thus sending current into the ground. In cases where an electrode fails, some salt water was sprinkled to enable conduction. In other cases, the electrode was firmly inserted into the ground since bad contact could cause an electrode to fail.

The Wenner array with 41 electrodes connected to two (2) 40 m long multi-core cables was used to collect the data. This configuration (Wenner array) is able to give better resolution of the subsurface resistivity distribution (Hamzah et al., 2006). The equipment used for the survey included the ABEM terrameter SAS 4000, power supply (12 V car battery), specially made wooden electrodes and multi-conductor cables (Figure 3.9). The electrodes were made with copper wire with wood acting as support to aid in insertion into the ground. They were permanently fixed to the ground during the course of the work and this helped in obtaining measurements for the same area throughout the duration.

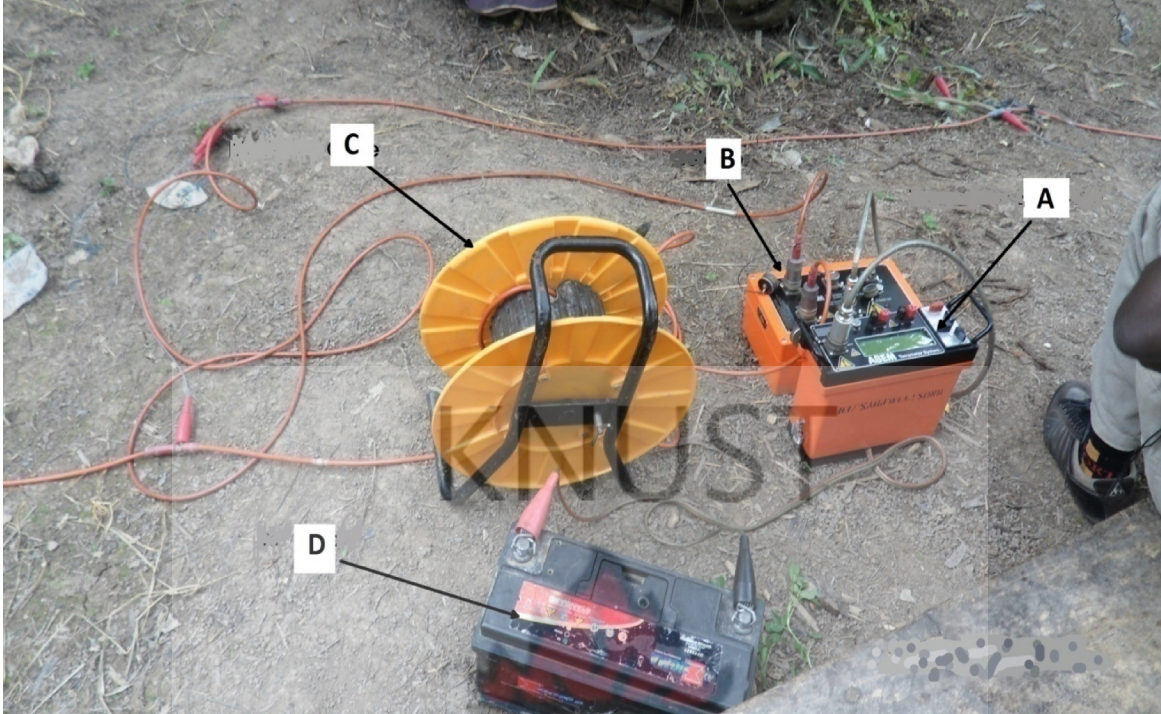


Figure 3.9: Resistivity measurement using the terrameter (A), Selector (B), multi-core cable (C) and a car battery (D)

For this survey, the electrode separations were 2 m. The electrode separation was chosen in order to get a better resolution of the near surface so as to acquire accurate time-lapse inversion results for the subsurface and particularly 1 m depth.

The resistivity measurements were taken along the profile lines, as shown in Figure 3.4, with 4 automatically selected electrodes according to the configuration protocols on the ABEM terrameter. Each electrode position was uniquely identified at a takeout on the cable. The electrodes were connected to the cable takeouts using jumpers (Figure 3.10). This helped in identifying the required current and potential pairs during the measurement at various data levels as ‘a’ (electrode separation) is increased by a factor (Figure 3.11).

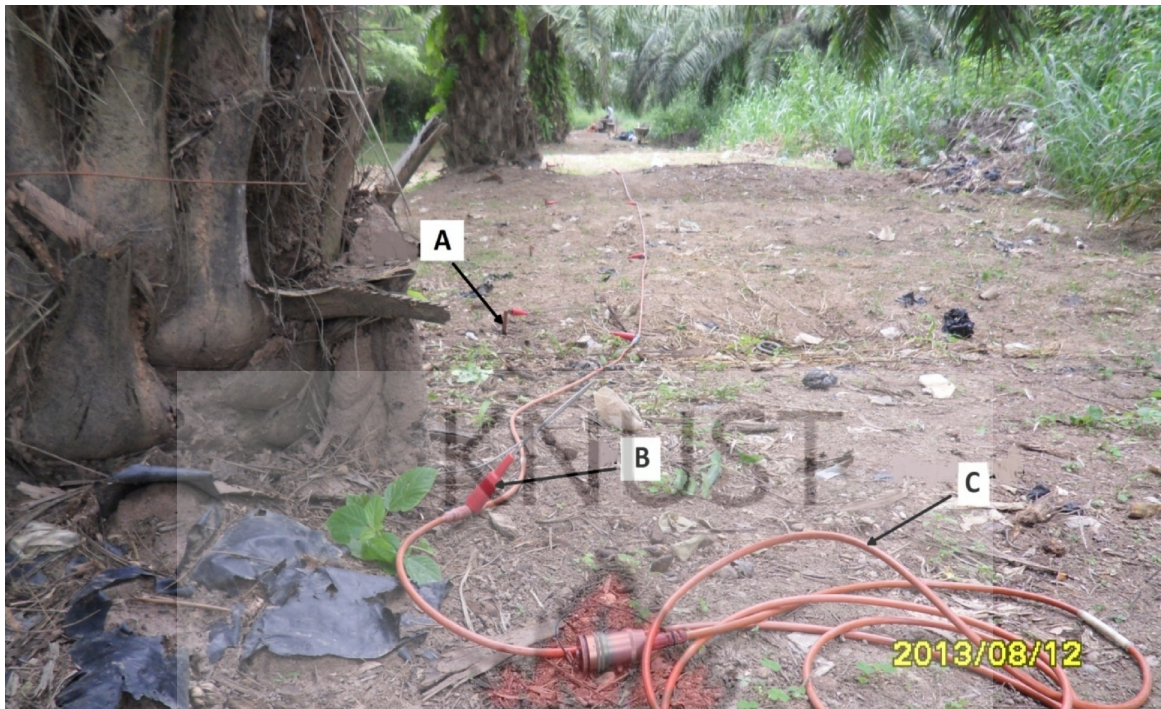


Figure 3.10: Line setup for measurements using special wooden electrode (A), jumper (B) and seismic cable (C)

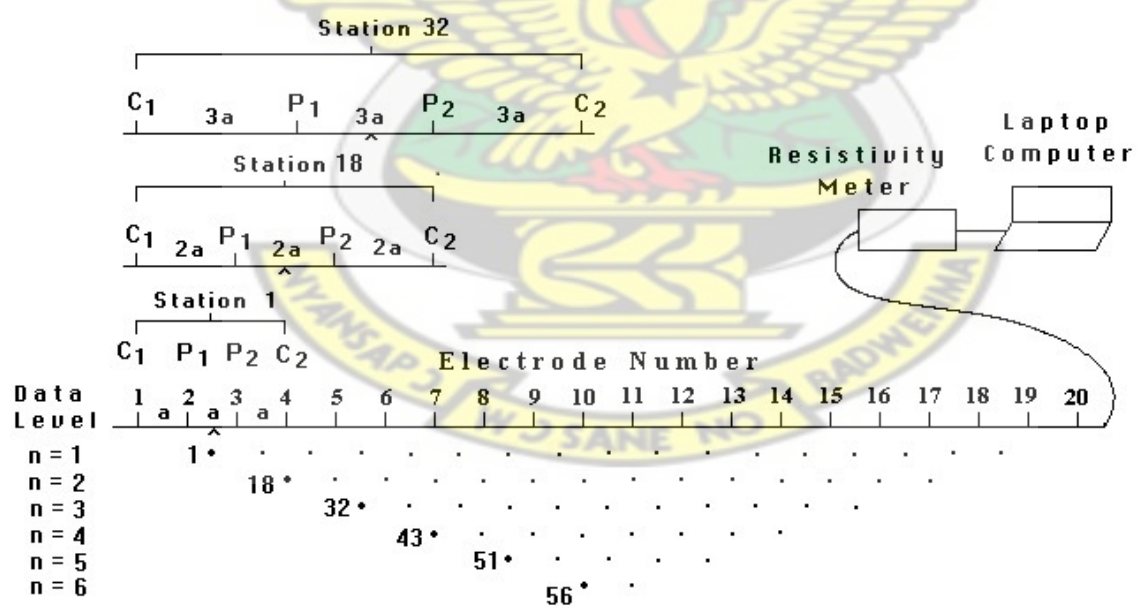


Figure 3.11: Sketch of electrodes for resistivity measurements for building a pseudosection (Loke, 2011)

In the case of the first data level, $n = 1$, the same depth is measured along the line with a constant electrode spacing of 2 m ('a'). As the electrode separation was increased automatically by a factor, deeper depth were probed with fewer data points ($n = 2, 3, 4$). These measurements were done automatically by the terrameter.

As a precaution for the acquisition of reliable and accurate resistivity data, the cables were checked for cuts and on every line, the electrodes were checked for contact resistance. Where the ground contact resistance was bad, salty water was sprinkled around the electrodes and lowered deeply into the ground. Also, the electrodes were left at the same spot to ensure measurements were made at the same spot over the course of the work.

3.3 Data Processing

In order to estimate the volumetric soil water content with the GPR system, two types of software were used. These were the *Reflexw 5.0* and *Grapher 8* by Sandmeier (1998) and Golden software respectively. The files that were processed using the *Reflexw* were the .RD3 Ramac files which were created by the GPR system using an in-built converter.

However, the resistivity data were inverted using *Res2DInv* and *Res3DInv* to produce resistivity and desaturation models.

3.3.1 GPR Processing Procedure

The processing sequence used to analyze the GPR data was as follows:

- Data display
- Data processing
- Picking
- Water content estimation

- Plot (graph/3D surface)

Data display

- A project directory was declared and *Reflexw* made its own subdirectories under the project directory after the program (*Reflexw*) was started.
- From the modules, 2D data analysis was selected and the *.RD3* Ramac files imported/converted to Reflex format; using the appropriate import parameters
- The 2D-data analysis module offered a range of different display possibilities. The data could be displayed either in wiggle or filled area point mode. An interactive color amplitude assignment could also be used for the point mode display.

Data Processing

Background Removal: This filter performed a subtraction of an averaged trace (trace range) which was built up from the chosen time/distance range of each section displayed.

Static Correction: Reflex puts T_0 (depth (z) = 0) at the start of signal so the first arrival typically was a couple of nanoseconds down section. Moving the first arrival to be at T_0 ($z = 0$) helps to eliminate the effect of variation in elevation between transmitter and receiver. This processing step was very important because the same time baseline must be used for all traces.

Dynamic correction: Normal move-out was performed to account for the separation between the transmitter and receiver so that traces approximate zero-offset rays. This processing step facilitates a dynamic, i.e. time dependent correction for a predefined constant velocity and the distance between source and receiver in time (y) direction (Sandmeier, 1998).

Band Pass Butterworth: the filter band was specified by setting two frequency values. The first value determined the low-cut frequency, the second one the high cut frequency. The frequency

spectrum below the low-cut and above the high-cut frequency was set to zero. Noise was suppressed with the band pass filter when it differed from the signal in its frequency content.

Dewow: A running mean value was calculated for each value of each trace. This running mean was subtracted from the central point. This filter was useful in eliminating possible low frequency parts of the trace. For this reason, a filter parameter (time window) was set to about one principal period and the filter acted on each trace independently.

Gain function: the filter facilitated the possibility of multiplying the data points by a given function $g(y)$ or $g(t)$ respectively. The function $g(t)$ consisted of a linear and exponential part with velocity (v) = 0.1 m/ns or 1.0 m/ns. The data was multiplied by this function in order to compensate for possible damping or geometric losses.

The processing sequence is shown in Figure 3.12. These processing steps helped to improve the quality of the signal traces and enhance the data.

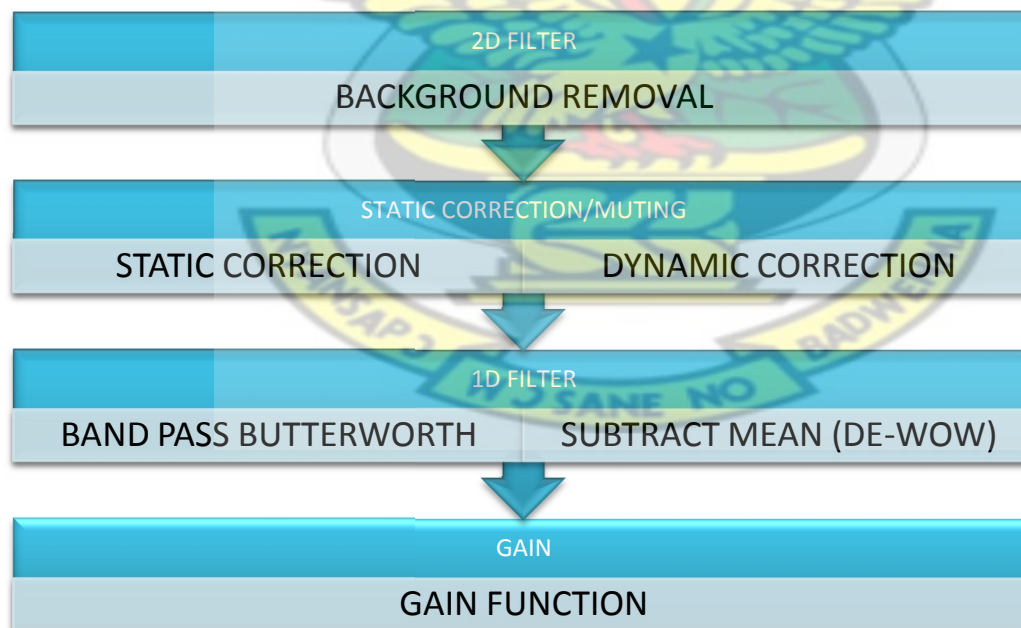


Figure 3.12: Schematic diagram showing processing sequence

Picking

The picking option allowed for the picking of the travel-time and amplitude of the direct ground waves. Picking of these arrivals was done using manual picking, continuous picking and semi-automatic picking using a phase follower (where manual editing is possible) and a full automatic picker. Manual and phase followers were mostly used to pick the arrival times. The picked values were corrected to the extrema (maxima and minima) or the zero-crossing. The direct ground wave was identified as the second wave recorded after the airwave. The picks were converted to ASCII format and saved. Picking was done in point (Figure 3.13) and wiggle (Figure 3.14) modes.

Water content estimation

In order to accurately and reliably estimate the spatial and temporal volumetric water content of the constant offset GPR technique, the picked ground wave velocity was used in the Topp model (Equation 2.22) after it was converted to dielectric constant and the results over the period have been displayed as graphs. The saved ASCII file was loaded into a spreadsheet (*Grapher 8*) and the volumetric water content was calculated from the estimations of the ground wave velocities (distance (1.2 m)/recorded travel time) using Equations 2.20 and 2.22.

The exploration depth or the depth of influence of the ground wave varied due mainly to the soil water content since the frequency of the transmitting antenna was constant.

Plot

The results for the survey were displayed as graphs. A graph of water content against distance was plotted with *Grapher*. The spatial distribution of the soil water content was also plotted with *Surfer 11*. The estimated volumetric water content for each day was collated and a grid file was created with *Surfer* and plotted.

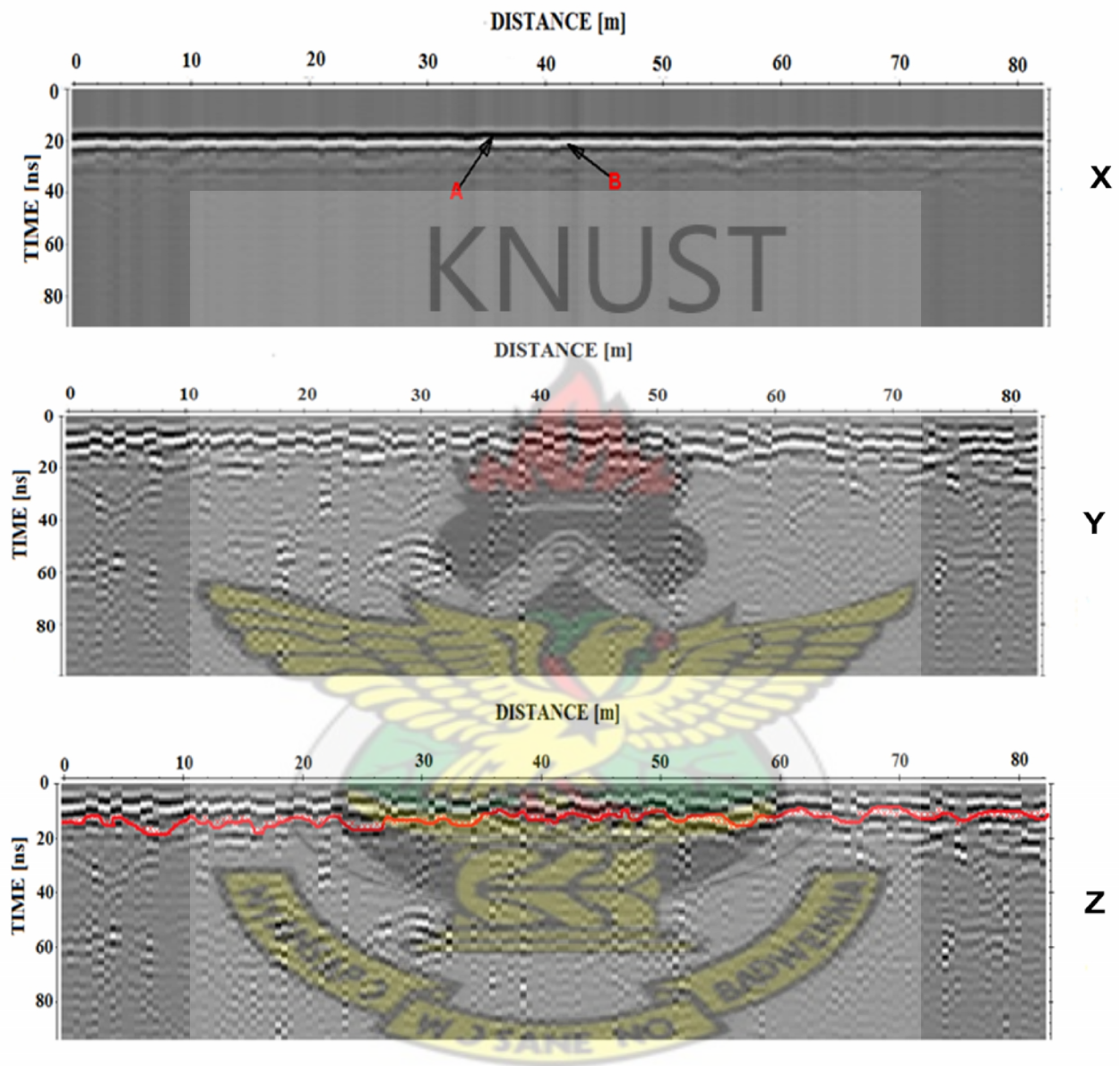


Figure 3.13: GPR data in point mode showing unprocessed data (X), processed data (Y), and picked data (Z), with (A) Airwave and ground wave (B).

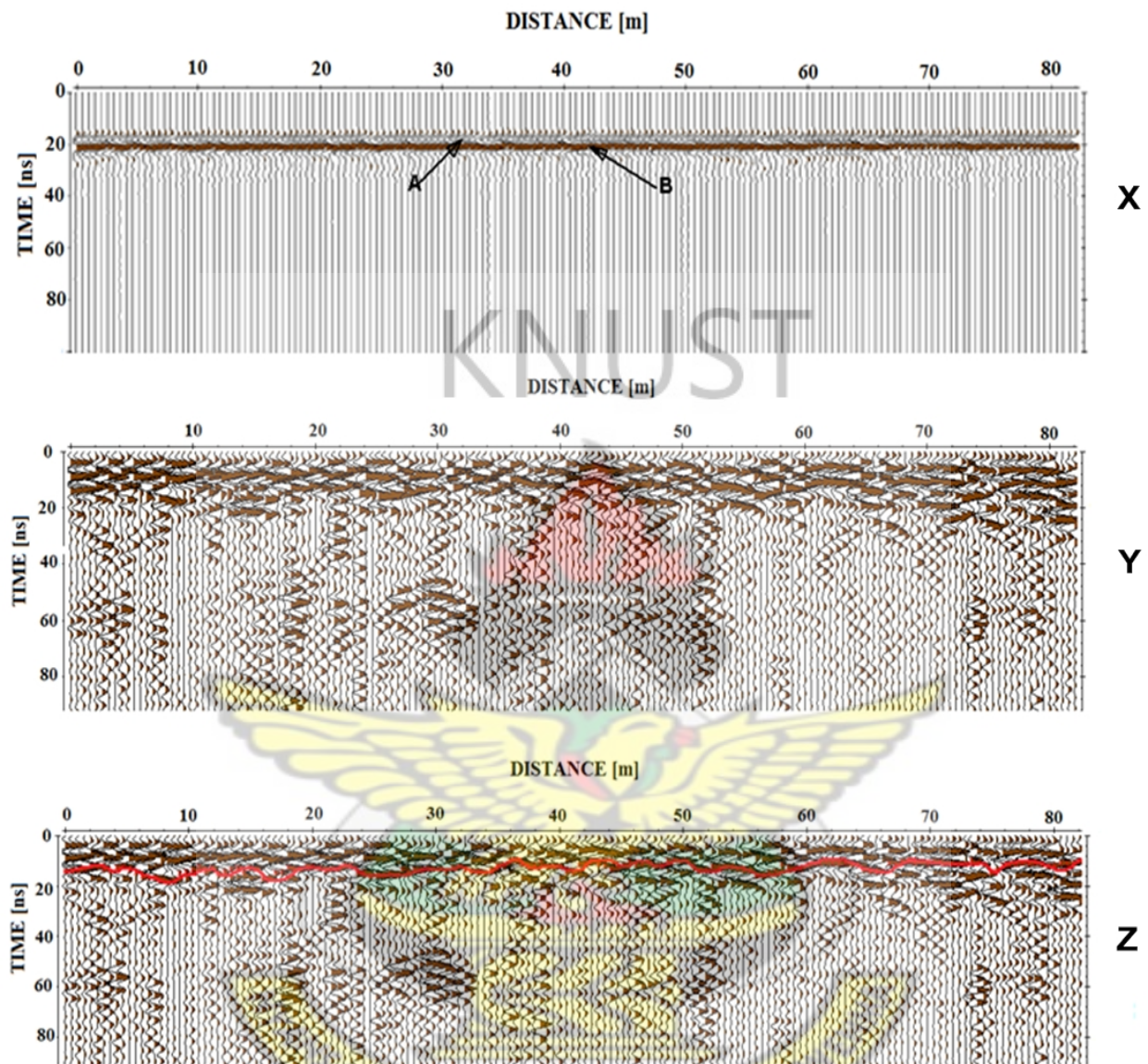


Figure 3.14: GPR data in wiggle mode showing airwave (A) and ground wave (B) with (X) Unprocessed data, (Y) processed data and (Z) picked data.

3.3.2 Electrical Resistivity Processing

The electrical resistivity data was processed by means of the *Res2DInv* and *Res3DInv* software. The data was first loaded and bad datum points (which usually appeared as spikes) were removed to enhance the data. Inversion was carried out to estimate the true resistivity of the subsurface. The L_1 norm (robust inversion technique) of the least square inversion method was used to allow the modeling of relatively sharp changes in resistivity because the inversion algorithm aims to minimize the absolute value of data misfits (Loke et al., 2003).

Model refinement option of the 'Inversion' menu was used to take care of the large resistivity variations near the ground surface. With this option, the program automatically reduced the unit electrode spacing it used by half of that given in the data. The user defined logarithmic contour interval option was used for easier comparison of the models (images). A total of 20 resistivity models were therefore generated for each line.

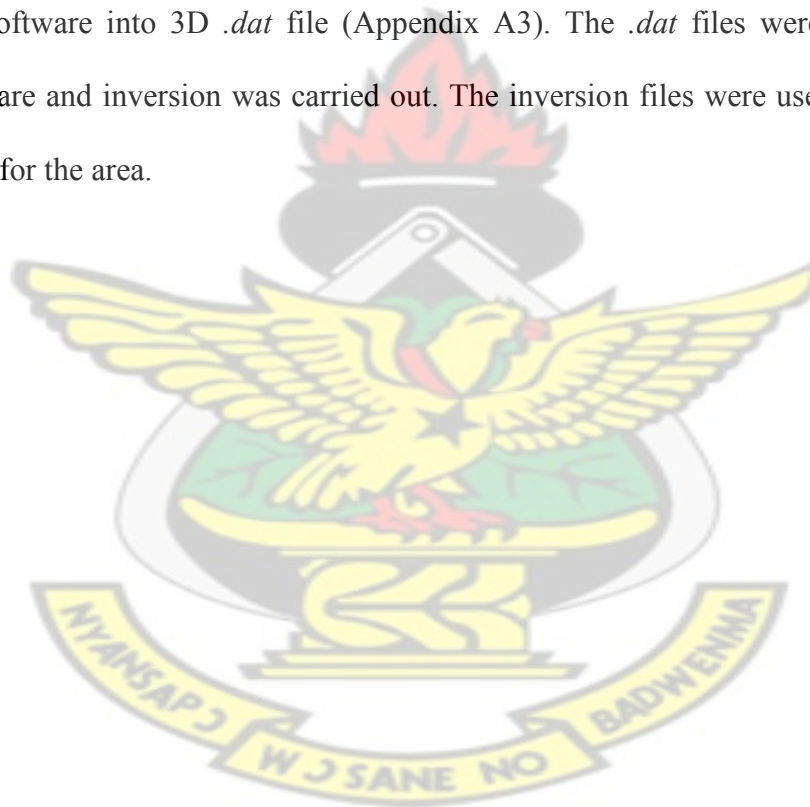
Time-lapse desaturation models were created for the 20 measurement days. This was done after using a script (Appendix A2) to join the 20 files for each line into a single file specifying the time interval in hours before the next measurements. In doing this, the 20 files were compared with each other using the Linux scripts in Appendix A1 to make sure they had the same data levels before joining them. In cases where some data points were missing because they have been removed, they were inserted without resistivity values to make all data points equal. This was to aid in the comparison for the desaturation models since the models were generated from comparison with the initial (first) resistivity measurements.

The water distribution is determined by plotting the percentage change in the subsurface resistivity of the inversion models for the data sets taken at different times when compared with the initial data set or model. The inversion of the data sets was carried out using a joint inversion

technique where the model obtained from the initial data set was used to constrain the inversion of the later time data sets (Loke, 1999).

The *Res2DInv* software was used to calculate the resistivity of the soil and subsurface materials. All inversions showed root mean square (RMS) error values of less than 3% which indicated that the generated models were reliable. The inversion results indicated that the subsurface soil has varied bands with various thicknesses and resistivity values.

For the 3D resistivity plots, the 2D files for the individual lines on each day were collated using the *Res2DInv* software into 3D *.dat* file (Appendix A3). The *.dat* files were loaded into the *Res3DInv* software and inversion was carried out. The inversion files were used to generate 3D resistivity maps for the area.



CHAPTER 4

RESULTS AND DISCUSSION

4.0 Introduction

This chapter is divided into two main parts; the first part is the results and discussion of the Ground Penetrating Radar (GPR) data and the second part is that for the time-lapse electrical resistivity tomography (ERT). A few of the results for both geophysical methods will be discussed and some others displayed in the Appendix B and C. The influence of rainfall on the volumetric water content for a month is examined. Also, some of the 3D resistivity models generated are used to compare the results obtained from the GPR measurements on selected days.

4.1 GPR Results

In this section, the spatial and temporal distribution of the volumetric soil moisture content is displayed as 2D graphs. The graphs show the distribution of soil water over 82 m stretch for each of the four profile lines. Considering the velocity range for the propagation of an electromagnetic wave through the soil ($0.05 \text{ m/ns} < v < 0.15 \text{ m/ns}$) that was used during processing, Sperl (1999) provided an empirical relation which gives the range of exploration depth (d) for this work as $0.07 \text{ m} < d < 0.125 \text{ m}$.

$$d = 0.145\sqrt{\lambda} \quad (4.1)$$

where λ is the wavelength of the electromagnetic wave in soil.

In the Figures 4.1- 4.8, the days of antecedent rainfall are indicated by asterix (*) attached to the day in the legends. 3D surface plots would also be employed to show the spatial distribution of the volumetric water content over the area for selected days.

Figures 4.1 and 4.2 show the volumetric water content distribution for 2 weeks from 17th June to 27th June 2013 for line 1. A steady but significant increase and decrease in the volumetric water content (θ_v) can be seen over the period. The increase could be attributed to infiltration by precipitation and the decrease to evapotranspiration, seepage and uptake of the soil water by the oil palm plant. A visual analysis of the results shows that higher levels of volumetric water content correspond to days of antecedent rainfall.

On June 18th, antecedent rainfall of 4.0 mm was recorded and this is evident in the results displayed in Figure 4.1. The graph shows a considerable increase, of approximately $0.2 \text{ m}^3 \text{m}^{-3}$ of water content from the 40 m to 82 m area and this could be attributed to the gently sloping nature of the land such that surface runoff of the rain got the area saturated. However, the same area lost the water rapidly the days after, probably due to the evaporation.

Figure 4.2 shows days with very dry conditions and fairly constant soil water distribution over the area (line 1) except for 25th June which recorded antecedent rainfall of 1.4 mm. It is evident that, this graph (June 25) shows the highest recorded water content of $0.35 \text{ m}^3 \text{m}^{-3}$ at the 4 m mark.

The volumetric water content distributions from 24th June to 5th July 2013 for line 2 are shown in the Figures 4.3 and 4.4. On this line, the water content is generally higher from 40 to 82 m with an average of $0.3 \text{ m}^3 \text{m}^{-3}$. The results for the 24th of June to the 27th of June as shown in Figure 4.3 is representative of dry conditions on line 2 since only 25th June recorded rainfall of 1.4 mm.

However, Figure 4.4 represents a week with very wet conditions with rainfall recorded at different times of the week. The 3rd of July representing a day with antecedent rainfall of 3.8mm shows the highest water content distribution on the line.

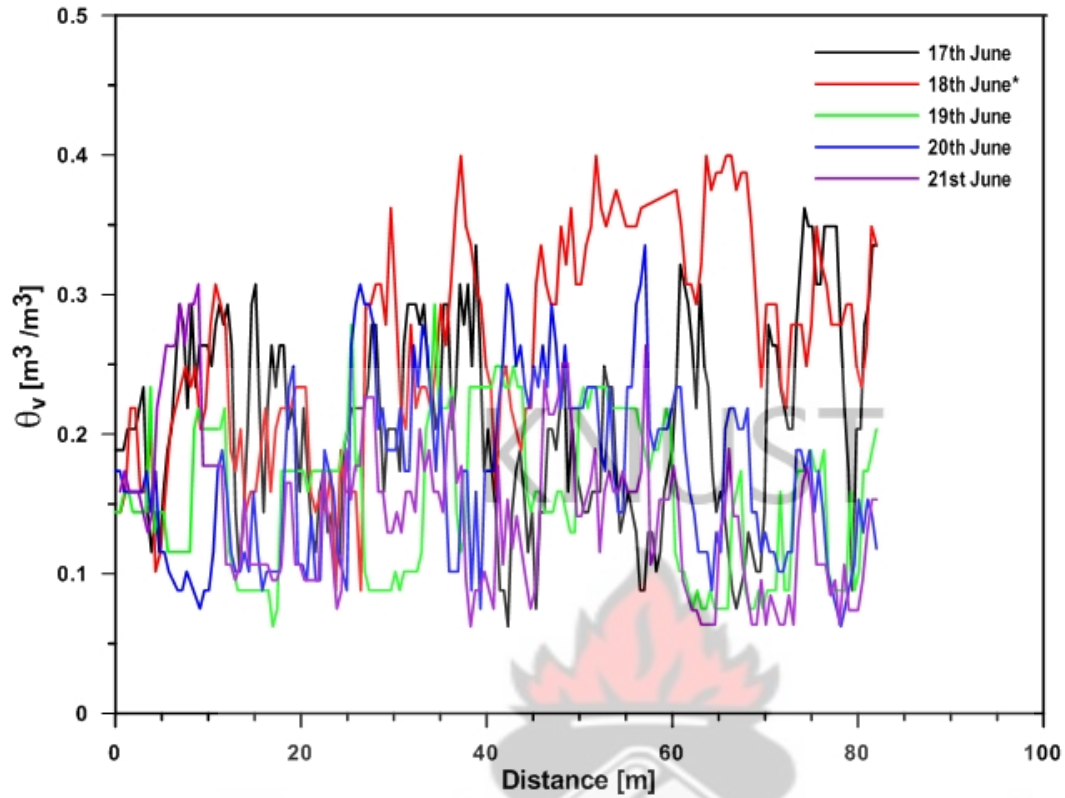


Figure 4.1: Volumetric water content for 17th to 21st June 2013 on line 1

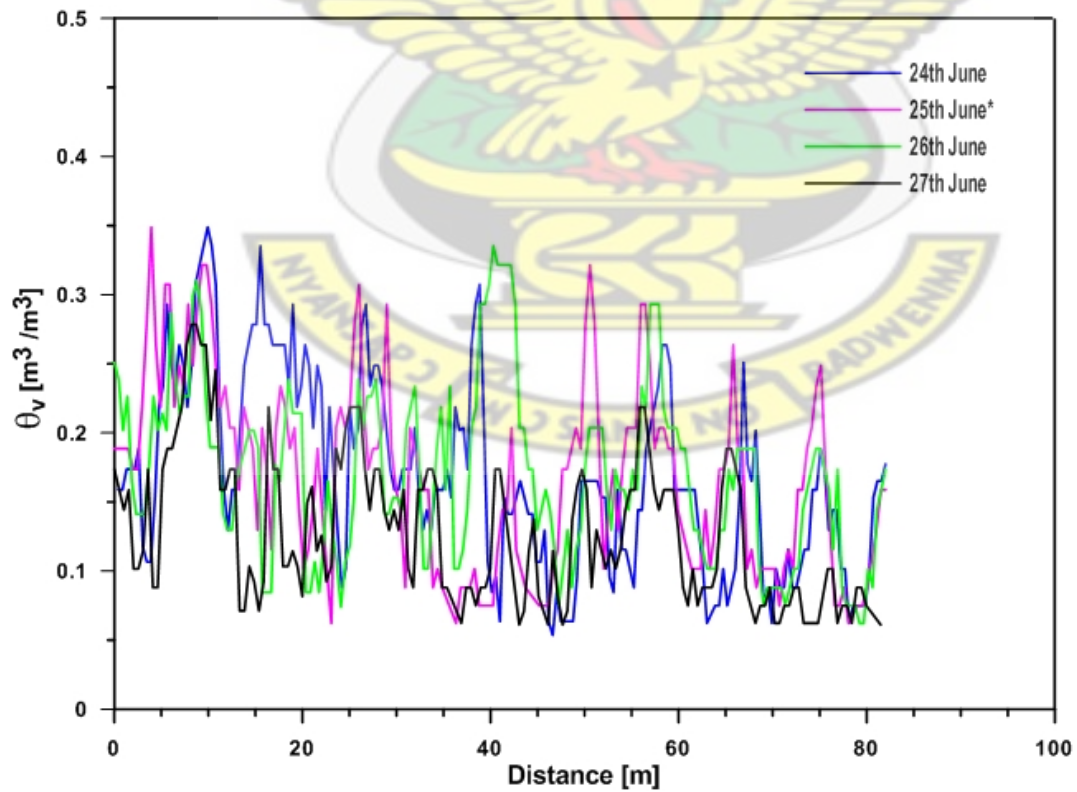


Figure 4.2: Volumetric water content on line 1 from 24th June to 27th June 2013

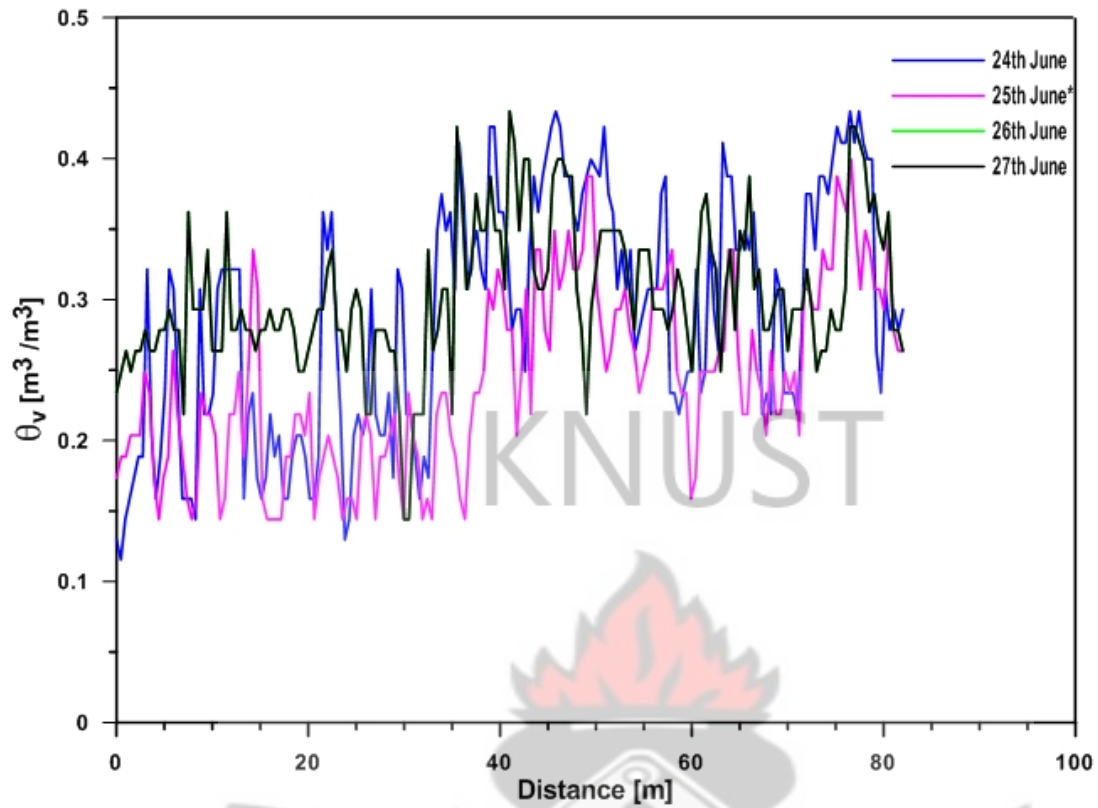


Figure 4.3: Volumetric water content distribution on line 2 from 24th June to 27th July 2013

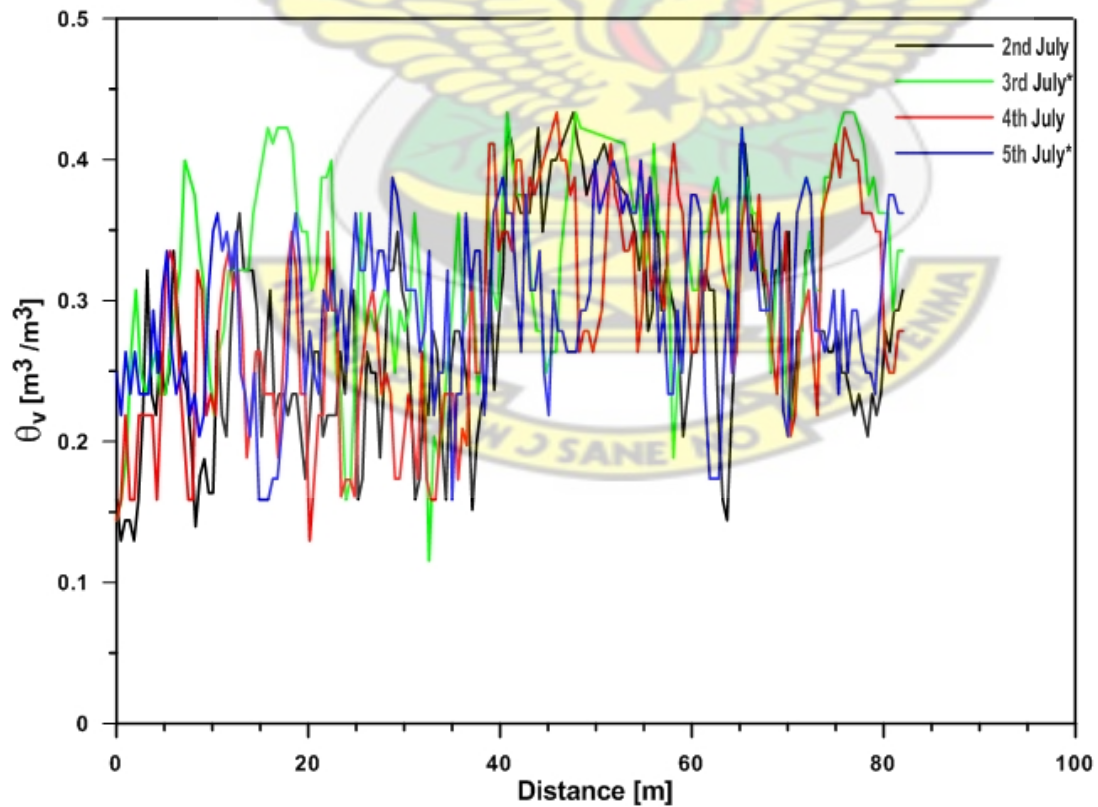


Figure 4.4: Volumetric water content distribution on line 2 from 2nd July to 5th July 2013

Results for the near surface water distribution for line 3 during the period between June 24th to 27th and August 16th to September 3rd are shown in Figures 4.5 and 4.6. The area shows an average soil water distribution of about $0.15 \text{ m}^3 \text{ m}^{-3}$ during dry conditions. However, an average of $0.35 \text{ m}^3 \text{ m}^{-3}$ is recorded for days with antecedent rainfall.

Figure 4.5 shows soil moisture that does not vary rapidly over the period along the line. Higher moisture contents are recorded on days with antecedent rainfall after the 45 m mark to the 82 m mark. Very low moisture was recorded at the 44 m mark throughout the period as shown in the Figure.4.5.

Figure 4.6 shows that high moisture content was recorded for 23rd August and 26th August, as antecedent rainfall was recorded on the 26th of August (Figure 4.6). An average difference of $0.2 \text{ m}^3 \text{ m}^{-3}$ in θ_v can be observed on the line during the period between 23rd August and 3rd September.

Line four (4) shows interesting results, as displayed in Figures 4.7 and 4.8. In Figure 4.7, it is evident that the first 40 m show higher moisture content even in graphs with antecedent rainfall on the 3rd and 5th of July. This could be attributed to the soil type in the area.

However, during very dry conditions, as shown in Figure 4.8, the lower regions show a reverse of the trend with that region showing higher water content. This could be attributed to evaporation rates and the degree of water conservation at the region. The water content measured over the day during the dry period remained fairly constant (Figure 4.8).

The rainfall rates for Anwomaso on the days of measurement have been shown in Table A.1 of Appendix A.

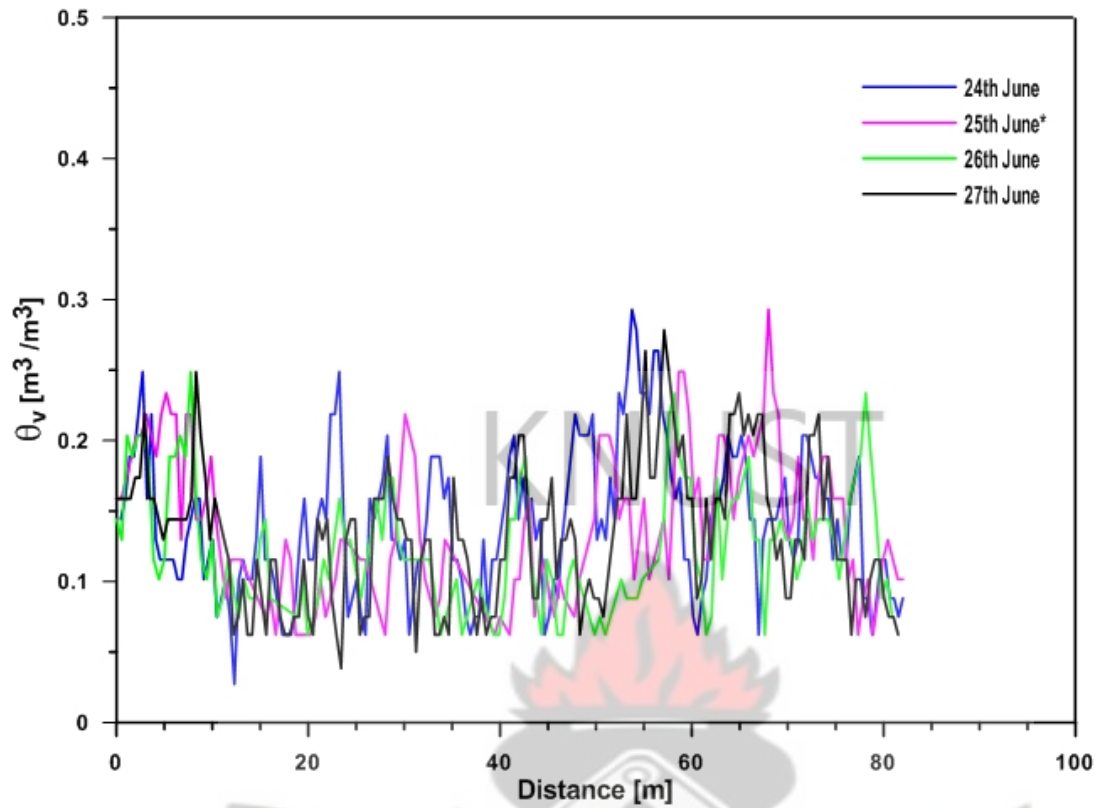


Figure 4.5: Volumetric water content distribution on line 3 from 24th June to 27th June 2013

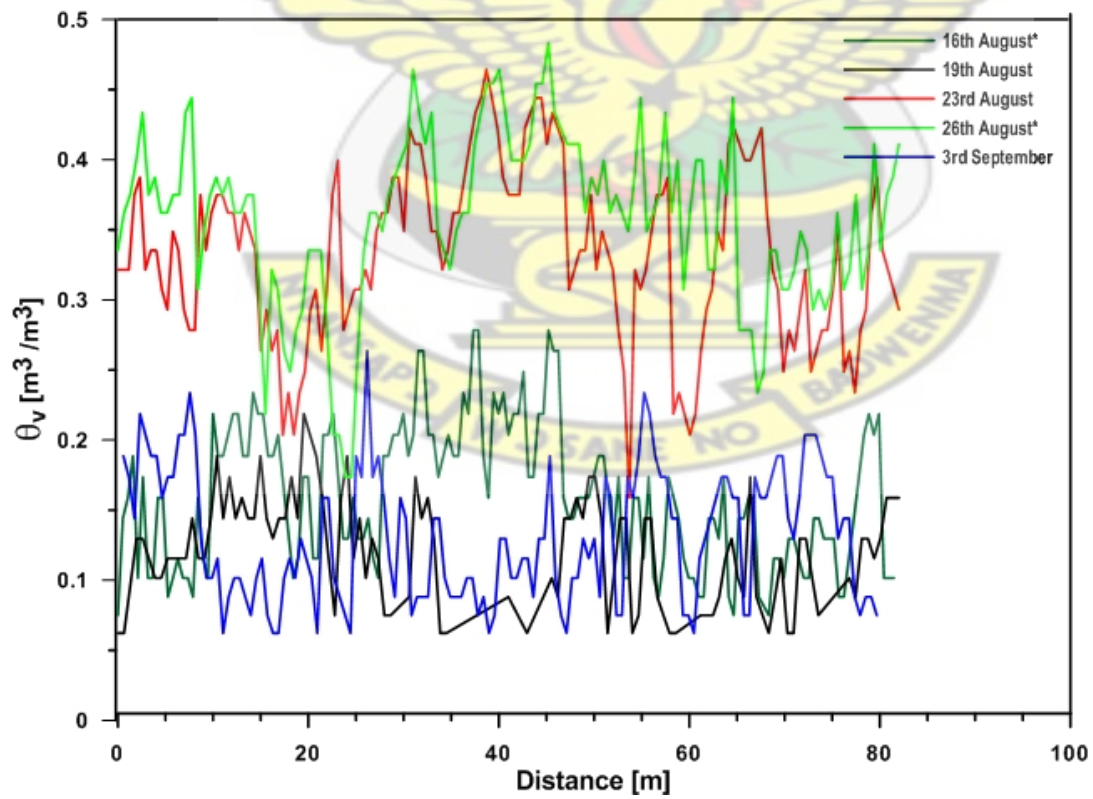


Figure 4.6: Volumetric water content for 16th August to September 3rd 2013 on line 3.

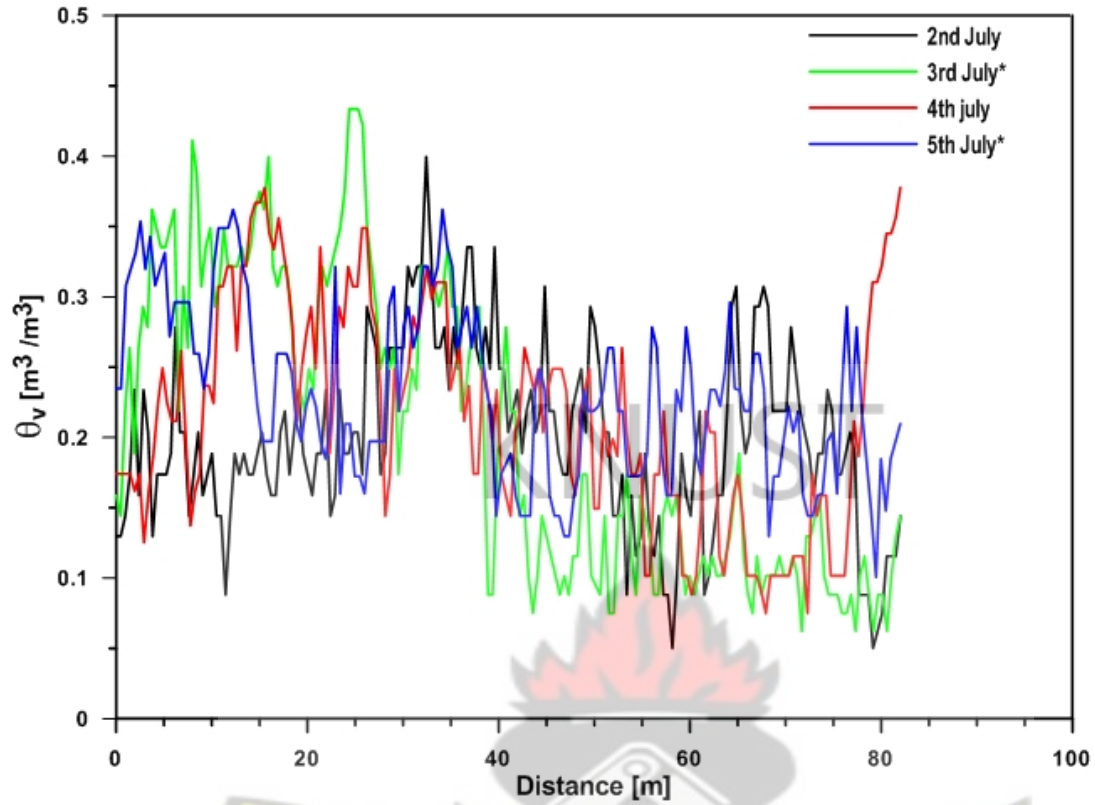


Figure 4.7: Volumetric water content distribution on line 4 from 2nd July to 5th July 2013

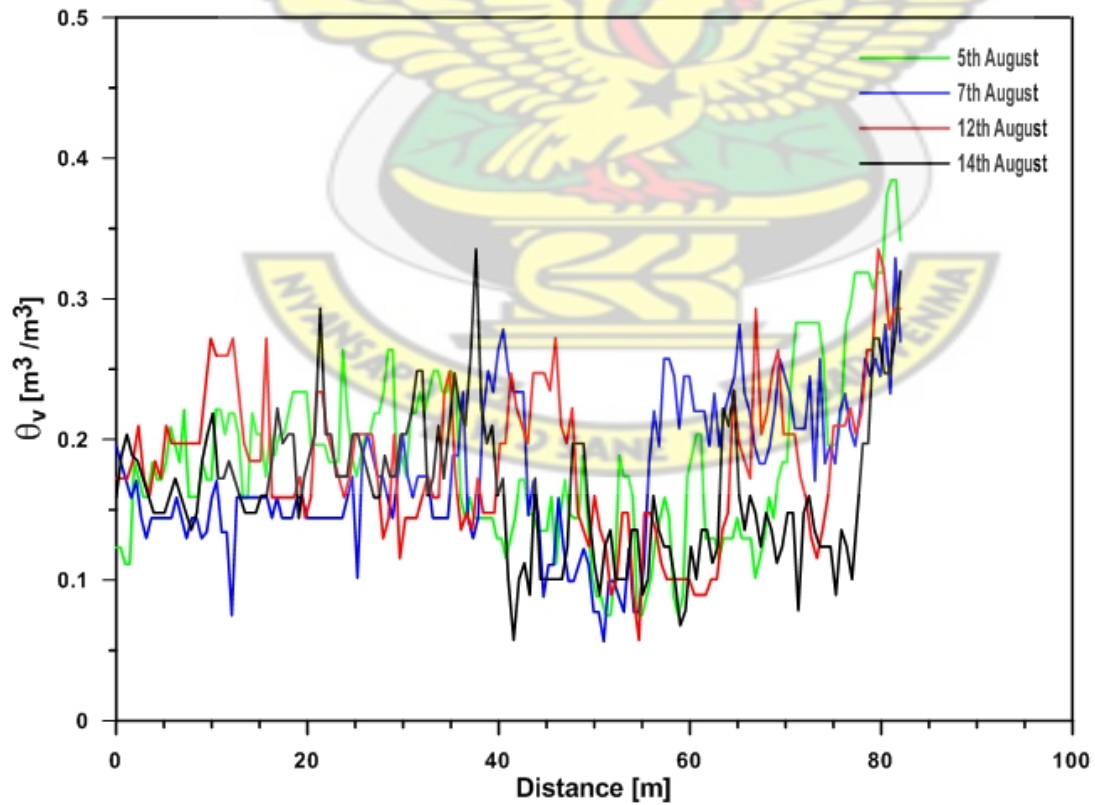


Figure 4.8: Volumetric water content distribution on line 4 from 5th August to 14th August 2013

4.1.1 Spatial water distribution

The 3D surface plots of the water content distribution for the research area are shown in the Figures 4.9 to 4.12. Figure 4.9 shows the spatial distribution of soil water on the first day of measurement thus the 17th of June 2013. Low water contents of about $0.1 \text{ m}^3\text{m}^{-3}$ were recorded in areas on line 1 and 4. However high water contents of up to $0.4 \text{ m}^3\text{m}^{-3}$ were also recorded at some spots on line 2 and 3.

Results for the 2nd of July as displayed in Figure 4.10 shows high water content on lines 2 and 4. The changes in the distribution on this day compared to the first day could be attributed to rainfall, seepage, evaporation and or water uptake by the oil palm plant. Low water content was recorded on line 3 and on the east of line 4 and line 1. Figure 4.10 represents a period with very dry conditions, hence the observed widespread low water content regions and generally low water content measured across the field.

The surface plot for the 26th of July 2013 shows high water content across the field except for line 3, as presented in Figure 4.11. The plot represents a day which recorded antecedent rainfall. It is noticeable on this Figure that, water content of about $0.4 \text{ m}^3\text{m}^{-3}$ was recorded at areas on the east which was low lying. The results suggest that runoff water from rainfall might have increased the water content on the east of the field.

Figure 4.12 shows the results obtained for 3rd September 2013, the last day of measurement. The water content distribution is fairly constant and this can be attributed to antecedent rainfall which caused an increase in the water content. In the Figure, the western section of the field showed higher water content especially on line 2. Line 2 consistently showed high soil water compared to the rest of the lines due possibly to the soil type in that region. It is possible that, this region is

characterized mainly by clayey loam soil which has greater water holding capabilities than sandy loam, as found on line 3.

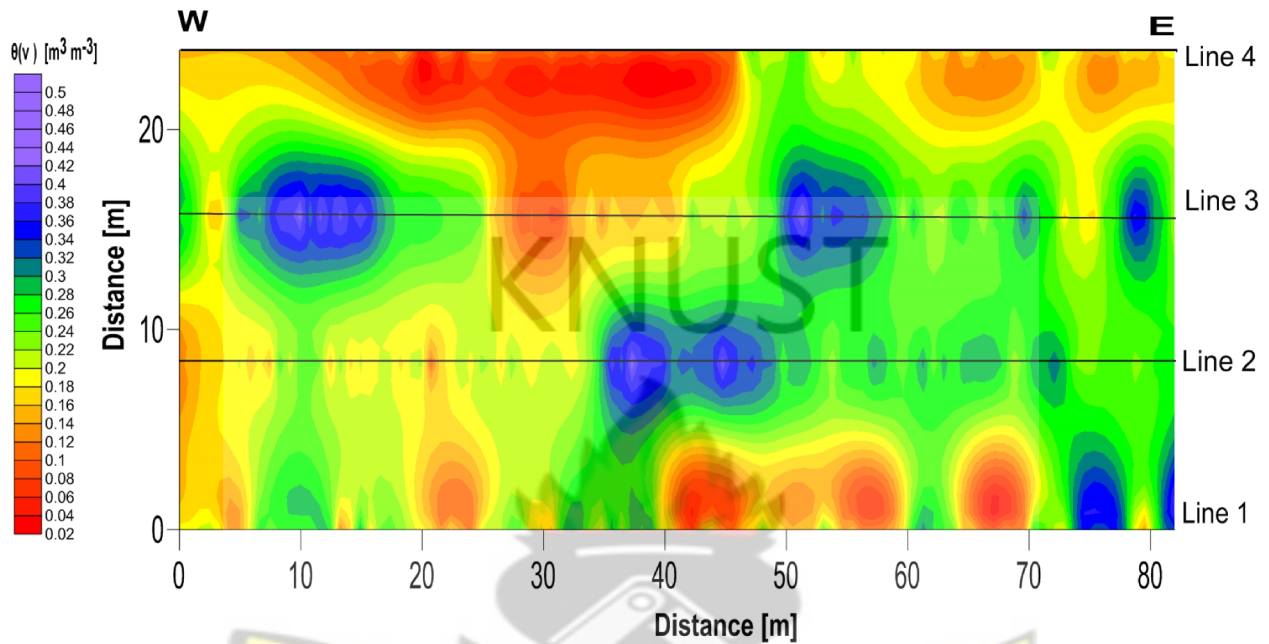


Figure 4.9: Spatial water content distribution for 17th June 2013 to a maximum depth of 0.1 m

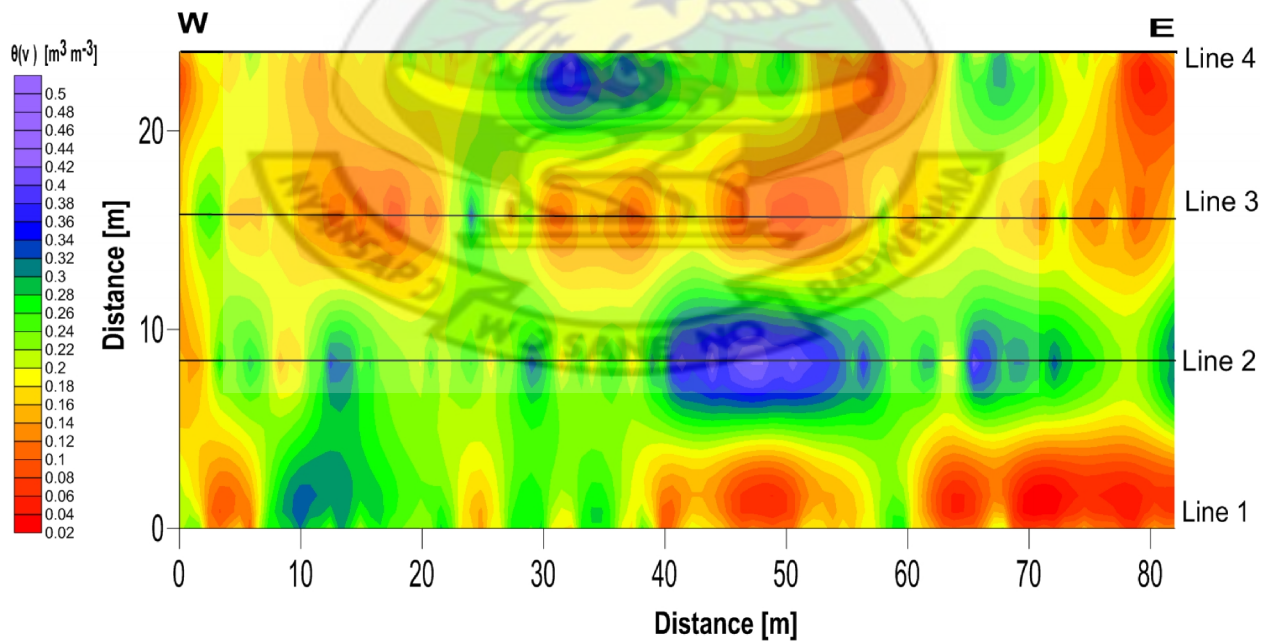


Figure 4.10: Spatial water content distribution for 2nd July 2013 to a maximum depth of 0.1 m

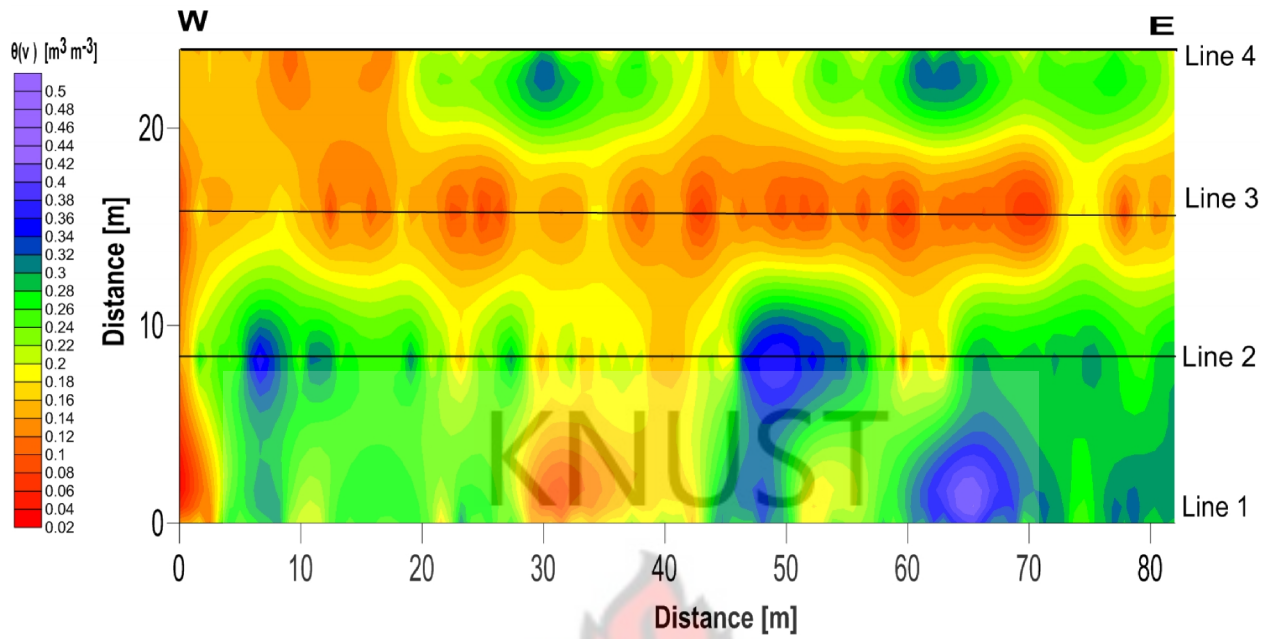


Figure 4.11: Spatial water distribution for 26th July 2013 to a maximum depth of 0.1 m.

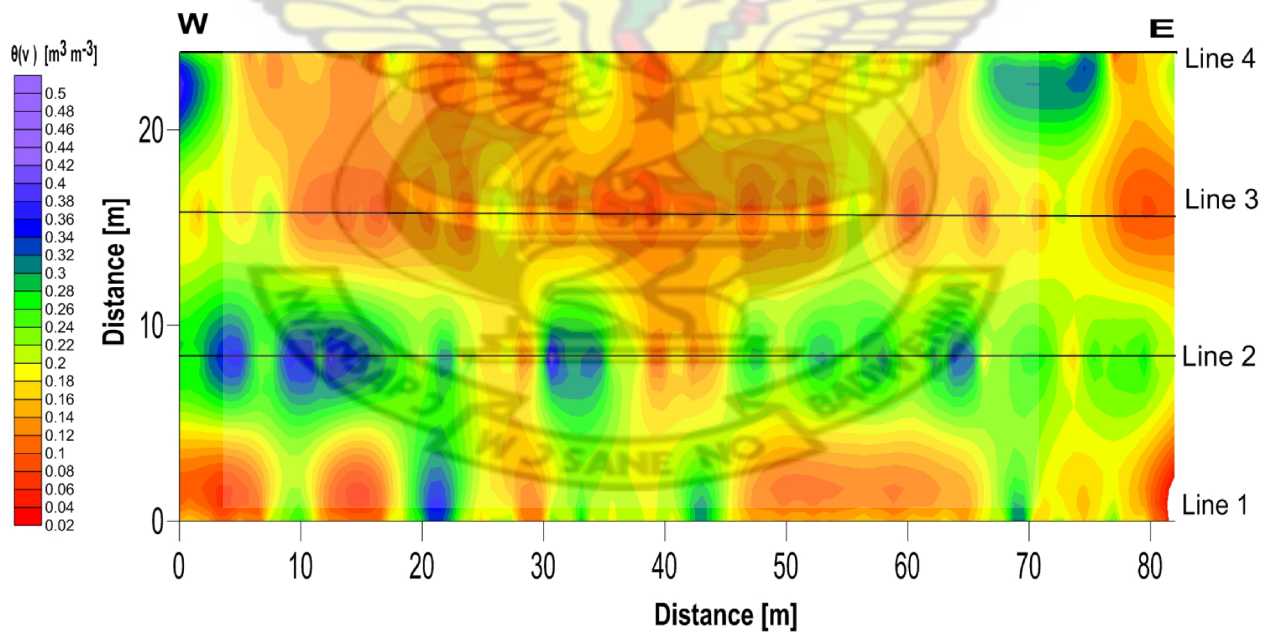


Figure 4.12: Spatial water content distribution for 3rd September 2013 to maximum depth of 0.1 m.

4.1.2 Influence of Rainfall on Water Content

From the GPR measurements, the mean soil water content [m^3m^{-3}] along the four (4) profile lines was determined. The mean soil water values were converted from [m^3m^{-3}] to [mm] to enable direct comparison with rainfall amounts in millimeters. The conversion was done with equation 4.2;

$$\theta_v[\text{mm}] = \frac{\theta_v[\text{m}^3\text{m}^{-3}] \times s[\text{m}^2] \times d[\text{m}] \times 1000[\text{mm}]}{\text{m}^3} \quad (4.2)$$

where θ_v is the mean soil water content, s is the surface area of the antenna configuration, d is the approximate exploration depth.

The optimal antenna separation was 1.2 m and the width of the configuration was 0.54 m. This was used to calculate the surface area of the antenna configuration. The exploration depth was chosen as 0.10 m. The conversion facilitated easier comparison of the GPR-derived soil water content with rainfall. This comparison is displayed graphically in Figure 4.13 which shows the temporal variation of GPR-derived soil water content and rainfall in [mm] for the period between 2nd and 26th July 2013 on lines 3 and 4.

The water from precipitation, when it hits the ground, is expected to cause a change in the measured soil water and the mean for the line on a day. The effect that the amount of rainfall has on the measured water content is examined graphically in Figure 4.13 where θ_1 and θ_2 are the soil moisture content for lines 3 and 4 respectively. Since rainfall is partitioned into various components as surface runoff and infiltration, the comparison would provide information on how much rainfall is held up in the pore spaces of the soil to depths of about 0.1 m. The information also provides an idea of the behavior of the soil types on the lines. Lines 3 and 4 would be compared since from the results line 3 shows low but consistent moisture content compared with

the other profile lines. Also, line 4 as discussed earlier shows water retaining ability in dry conditions hence changes in the water content would be easily detected in the measurements.

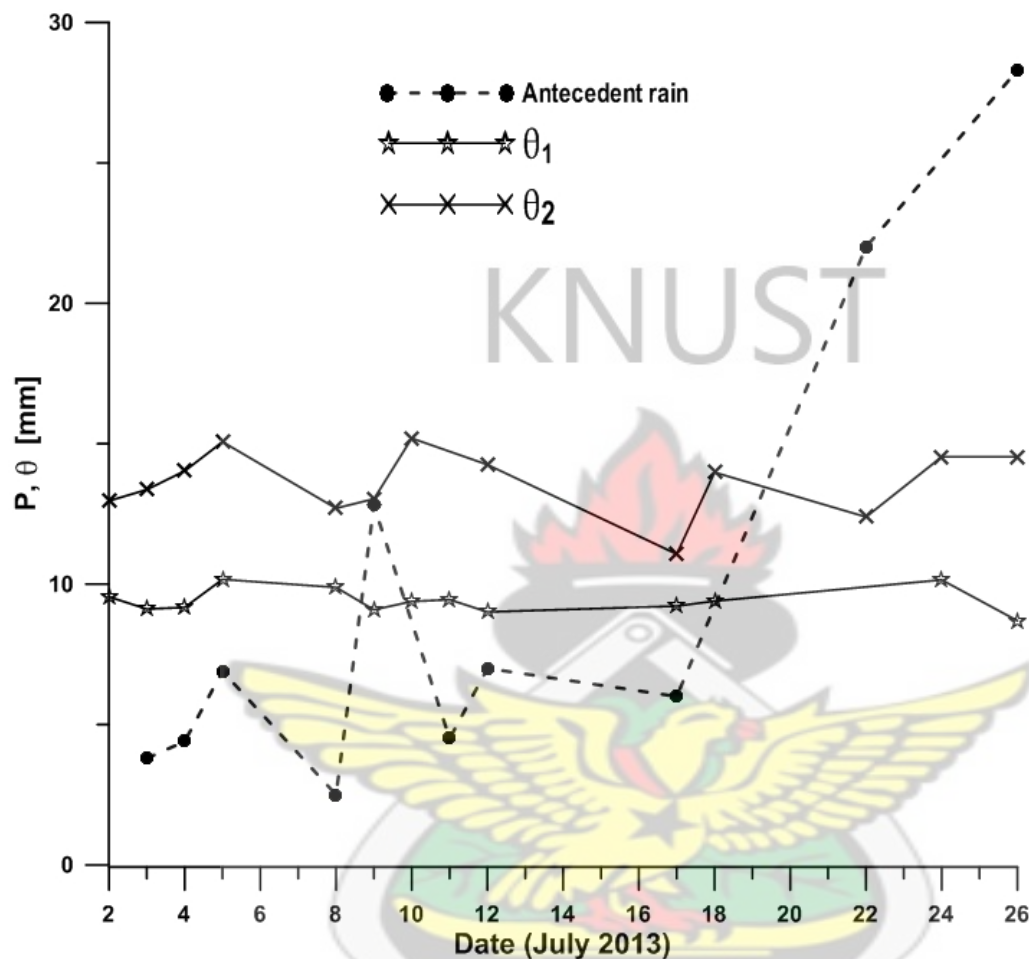


Figure 4.13: Relation between soil moisture and precipitation; θ_1 and θ_2 are the average water content for line 3 and 4 respectively.

In most cases, the antecedent rainfall increases the average soil water content (θ) on the line. A typical example can be seen from the 3rd of July to the 5th of July 2013 in Figure 4.13. As rainfall rates increases, soil moisture increased. In some cases where no rainfall was recorded over a period, for example, from the 5th to 8th and from 12th to 16th, the average water content decreased on line 4 and remained fairly constant on line 3. Additionally, the changes in the water contents

could also be attributed to soil types (sandy loam and sandy clay loam) on the line. Line 3 could be made up of a very permeable soil such that it is unable to retain water but rich in organic matter to be able to conserve its moisture as shown in Figures 4.9, 4.10 and 4.11.

4.2 Resistivity Models

Resistivity is a function of a number of soil properties which include the degree of water saturation. Resistivity measurement is therefore greatly influenced by degree of water saturation in soil. When the soil is homogenous, the resistivity is constant and independent of electrode spacing and surface location (Loke, 2000).

The 2D resistivity models are from the west-east direction and display resistivities to depths of about 13 m. However for the purpose of this work, particular attention was paid to the first 1 m of the models presented.

The models for line 1 are from the 9th to the 12th of July 2013 as shown in Figure 4.14. The near surface shows varied distribution of resistivities. The variation can be attributed to changes in the water content since the same soil material was measured with permanently fixed electrodes with the only varying parameter being the degree of water saturation.

It was observed from the four models for line 1 that, since there was no recharge to the ground from rainfall after the 9th of July 2013, the resistivity of the topsoil increased over the period till 12th July 2013, when rainfall was recorded before the measurements were made. The changes in resistivity on a small scale can be observed at the 16 m mark on the line where an oil palm plant is located. As expected, water is taken up by the plant hence the water loss would be associated with increase in resistivity from about 500 Ωm to about 600 Ωm for the subsequent days till rainfall was recorded on the 12th where resistivity in that area decreases. The resistivity for the 16 m mark therefore decreased from 600 Ωm to about 500 Ωm due to the increase in water content.

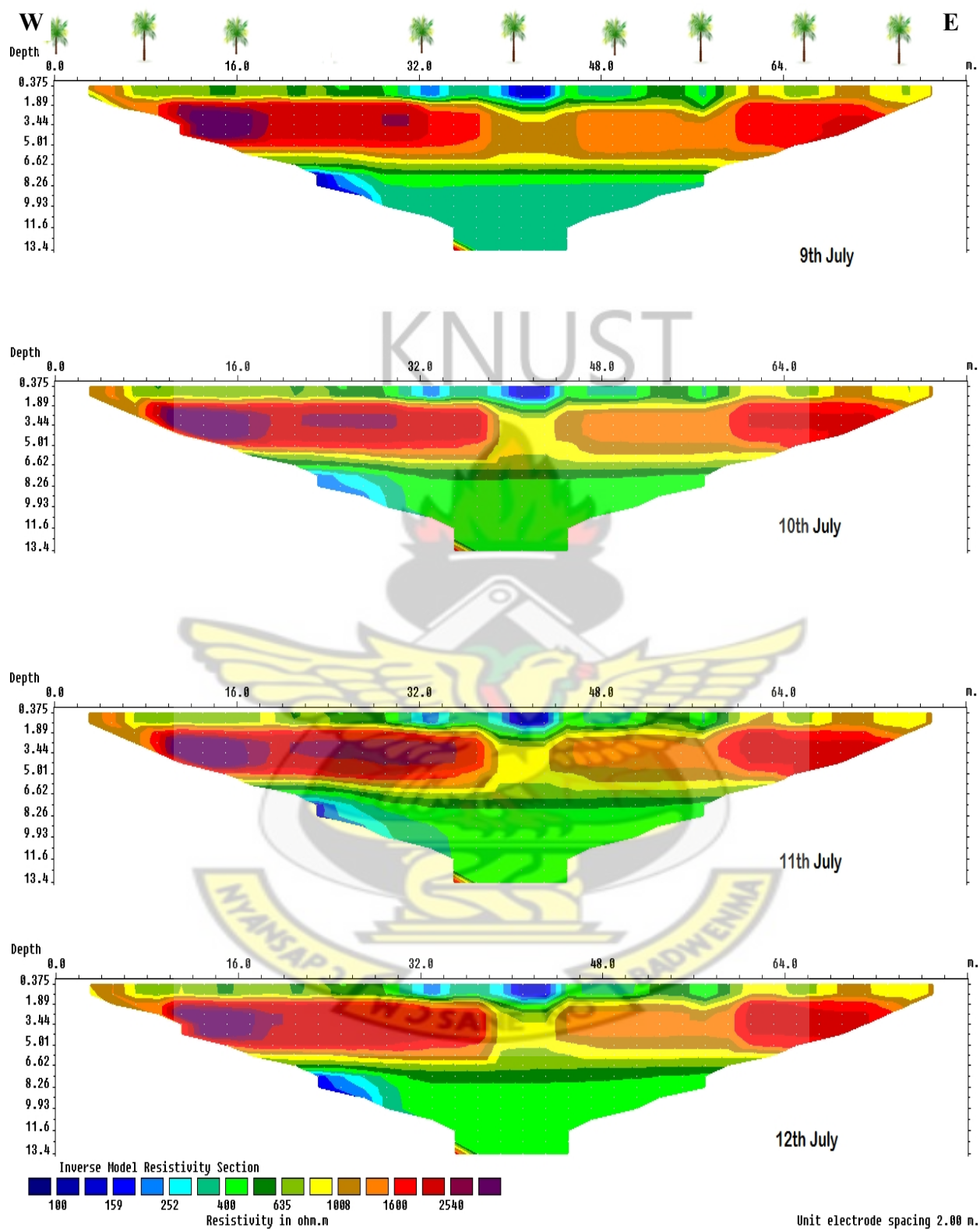


Figure 4.14: Resistivity models for line 1 from 9th to 12th July 2013.

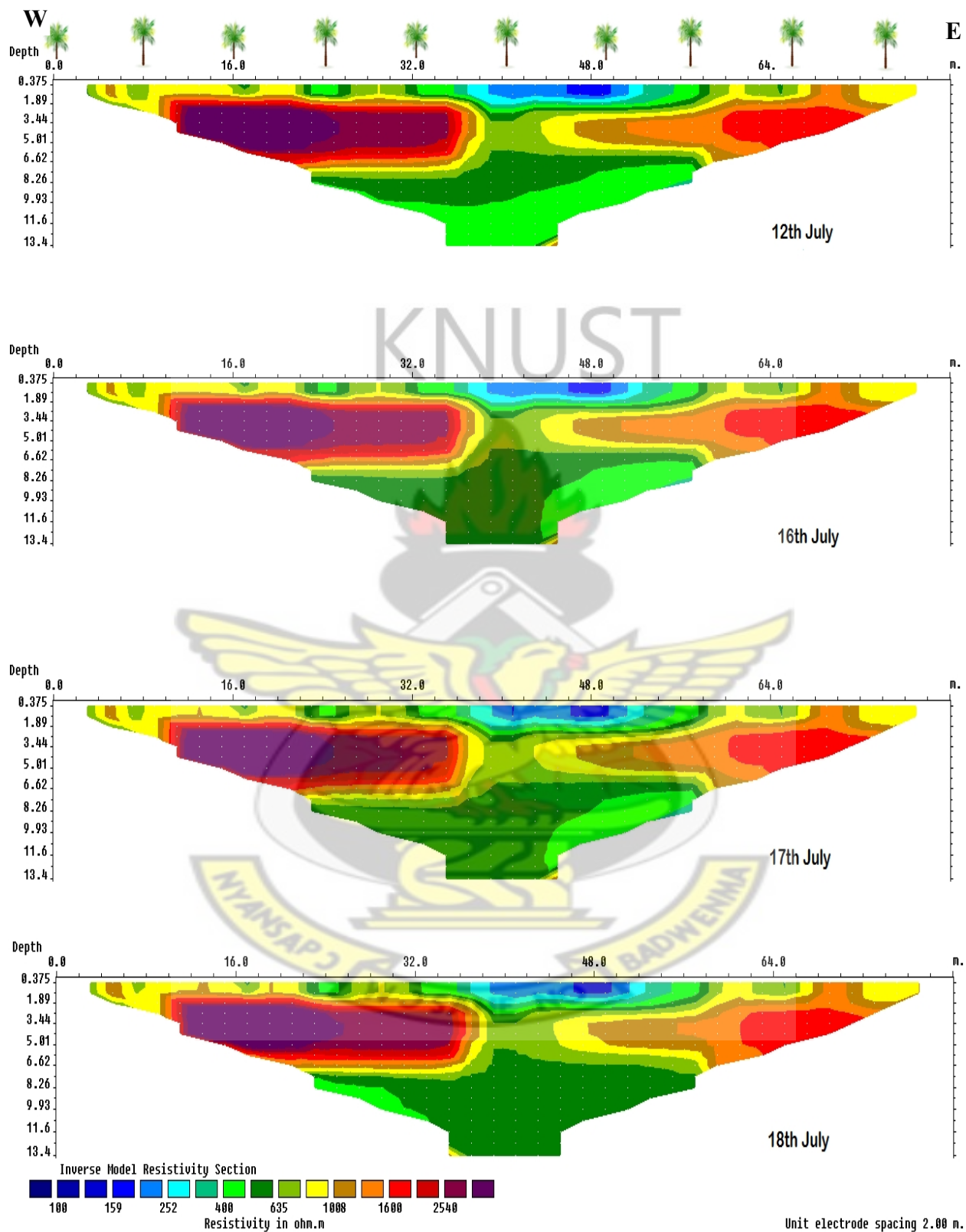


Figure 4.15: Resistivity models for line 2 from 12th July to 22nd July 2013

The models for the second line, as shown in Figure 4.15, represent measurements made on 12th July 2013 and from the 16th to 18th of July 2013. They show decreases in water content during days of no rainfall from the 16th to 18th of July 2013. Typical examples can be made of the 16 m and 64 m marks over the period, as shown in the models. In the topsoil, the relatively low resistivity region from 36 m to 54 m from the surface to a depth of about 1.5 m may be attributed to probable high clay content in the region and or the burrowing activities of earthworms in the region. This region, like others on the lines 1 and 3, show very little changes in the resistivity due to the probable presence of micro voids filled with air thereby leading to the low resistivity measurements and very little changes in the resistivity over the period (Loke 2000).

The models for line 3, as shown in Figure 4.16 support the assertion that the region may be filled with micro voids and or a porous soil material. It is evident from these models that the relatively low resistivity region supposed to be made up of micro voids serve as **channel** for groundwater infiltration. The high resistivity layer (zone) from 2 m depth of about 6 m thickness is either impermeable or has a very low infiltration rate. However, the changes in resistivity between 600 and 500 Ωm just below the low resistivity region can be attributed to infiltrating rainfall.

The first model on the 24th of July 2013 represents a day which saw no antecedent rainfall. The models for the 26th and 5th of August 2013, represent periods with 28.3 mm rain and no rain respectively with resulting decrease and increase in resistivities. This is visible on the near surface (1 m) resistivity distribution.

On the 7th August 2013 model, even as the resistivity increases at the near surface due to lack of rainfall, the resistivity below the high resistive layer ($>1600 \Omega\text{m}$) decreases due to probable recharge from the water holding clay region. This explains the reason why the low resistivity areas on each of the three lines show little or no change in resistivity during the course of the work.

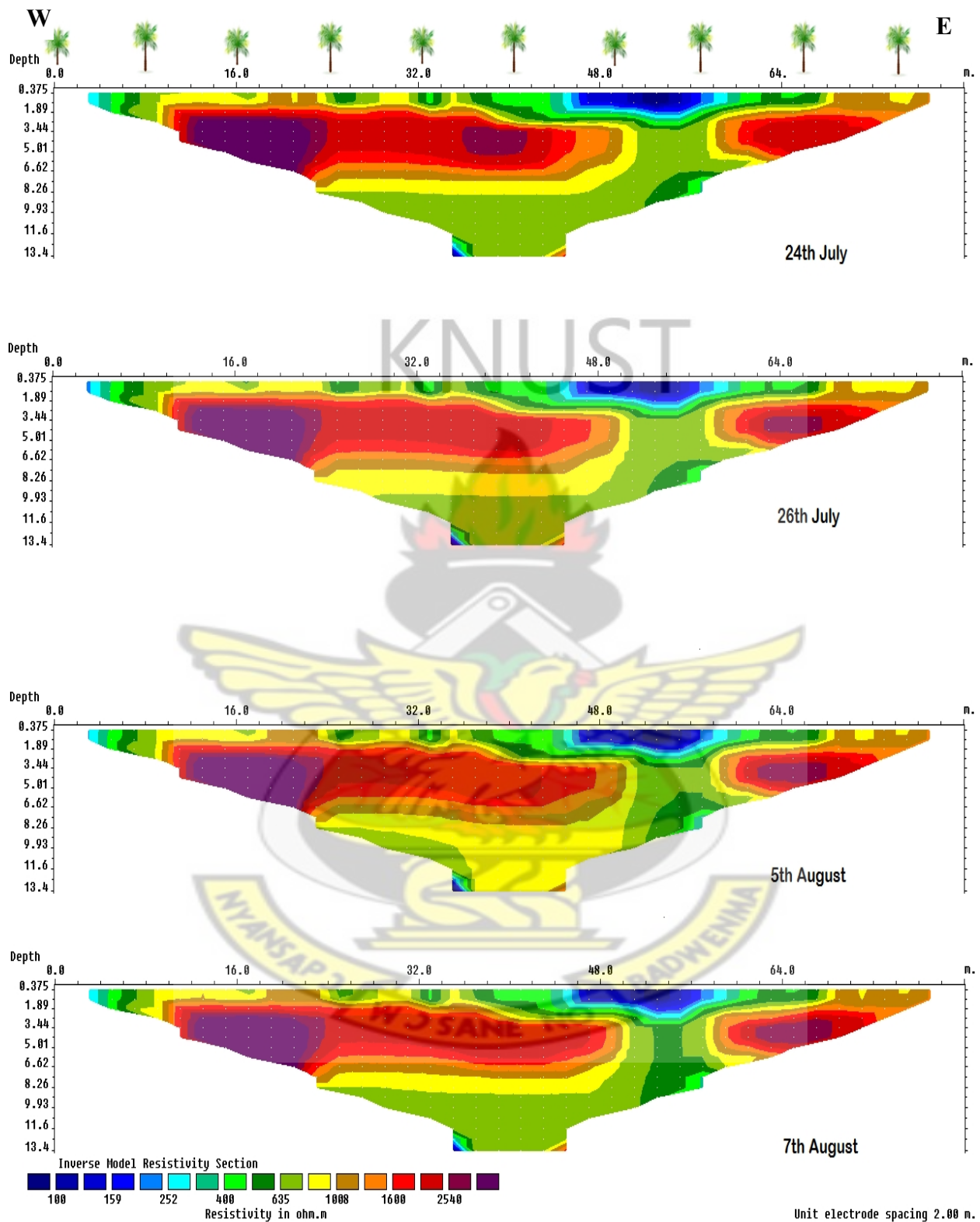


Figure 4.16: Resistivity models for 24th July to 7th August 2013 on line 3

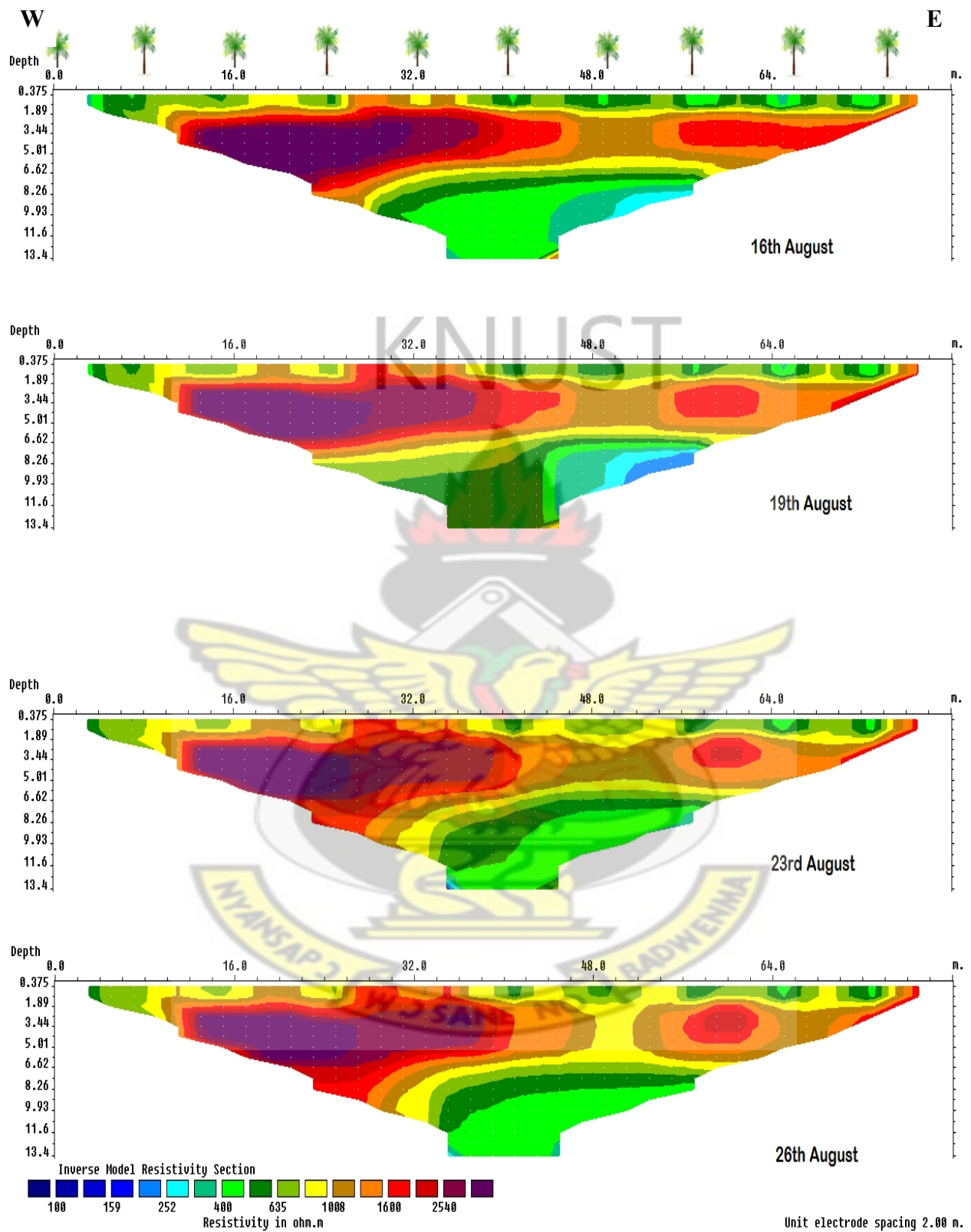


Figure 4.17: Resistivity models for 16th to 26th August 2013 on line 4

The fourth line shows very peculiar results compared to the other three lines. On this line, the low resistivity region encountered in the previous models cannot be found here. The models on this line therefore show significant changes (increase and decrease) in resistivity for all the areas with oil palm plant and the subsurface in general. In this case, the loss of water near the oil palm can be attributed to uptake by the oil palm plant, evapotranspiration and infiltration. Evaporation and infiltration can be linked to the water loss at bare areas.

In these models as shown in Figure 4.17, there is increase in resistivity as a result of no rainfall on 23rd August, 2013. It can be observed that the top soil increased in resistivity (400 Ωm to 600 Ωm in some areas) from the 16th to the 26th of August, 2013.

4.2.1 Desaturation Models

The water distribution for the field can be easily determined by plotting the percentage change in desaturation. Since the resistivity survey was carried out in time, and the measurements were made before and after rainfall, it is possible to compare the inversion models for the various data sets to the initial data and determine the degree of saturation or desaturation over the period.

Twenty (20) measurements were made for the resistivity at intervals of 24 hours for the first 8 days and 48 hour for final 12 days. The desaturation models therefore provide information on the changes in the resistivity due to changes in moisture content over the period from the initial measurement.

For example, in Figure 4.18, time series 2 shows the percentage desaturation between the second day (after 24 hours) of measurement and the first while time series 9 shows percentage desaturation between the ninth day of measurement and the first day, thus 13 days.

In the case of the desaturation models, areas with negative percentages are areas with increase in moisture content. Increasing percentage desaturation would mean loss of water since the initial measurement was made.

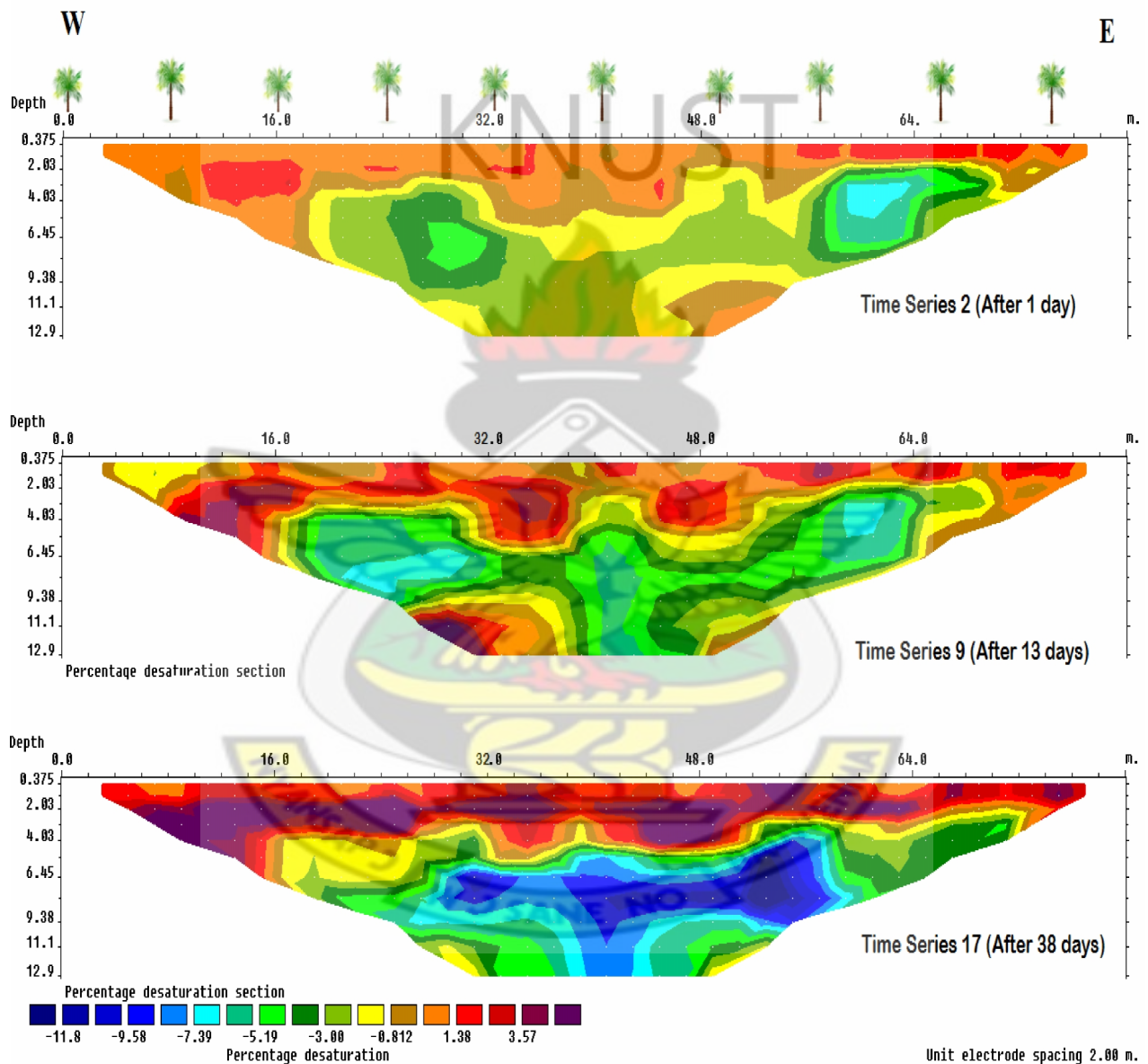


Figure 4.18: Desaturation models for 10th and 22nd of July and 16th August 2013 on line 4

Time series 2 shows general desaturation (1% - 2%) from the first day of measurement due to the fact that no rain was recorded during this period and soil water was lost. Time series 9 however shows patches of saturation (increase in water content) from the 4 to 13 m mark and also from 18 to 24 m. Moreso, desaturation is recorded at the locations with an oil palm plant at 16 m, 32 m, 41 m, 58 m and 66 m. The increase in the soil water can be attributed to previous rainfall before measurements were taken on the 22nd of July 2013. Time series 17 on the 16th of August 2013 show higher percentages of desaturation at the top to depths of about 4 m and saturation below.

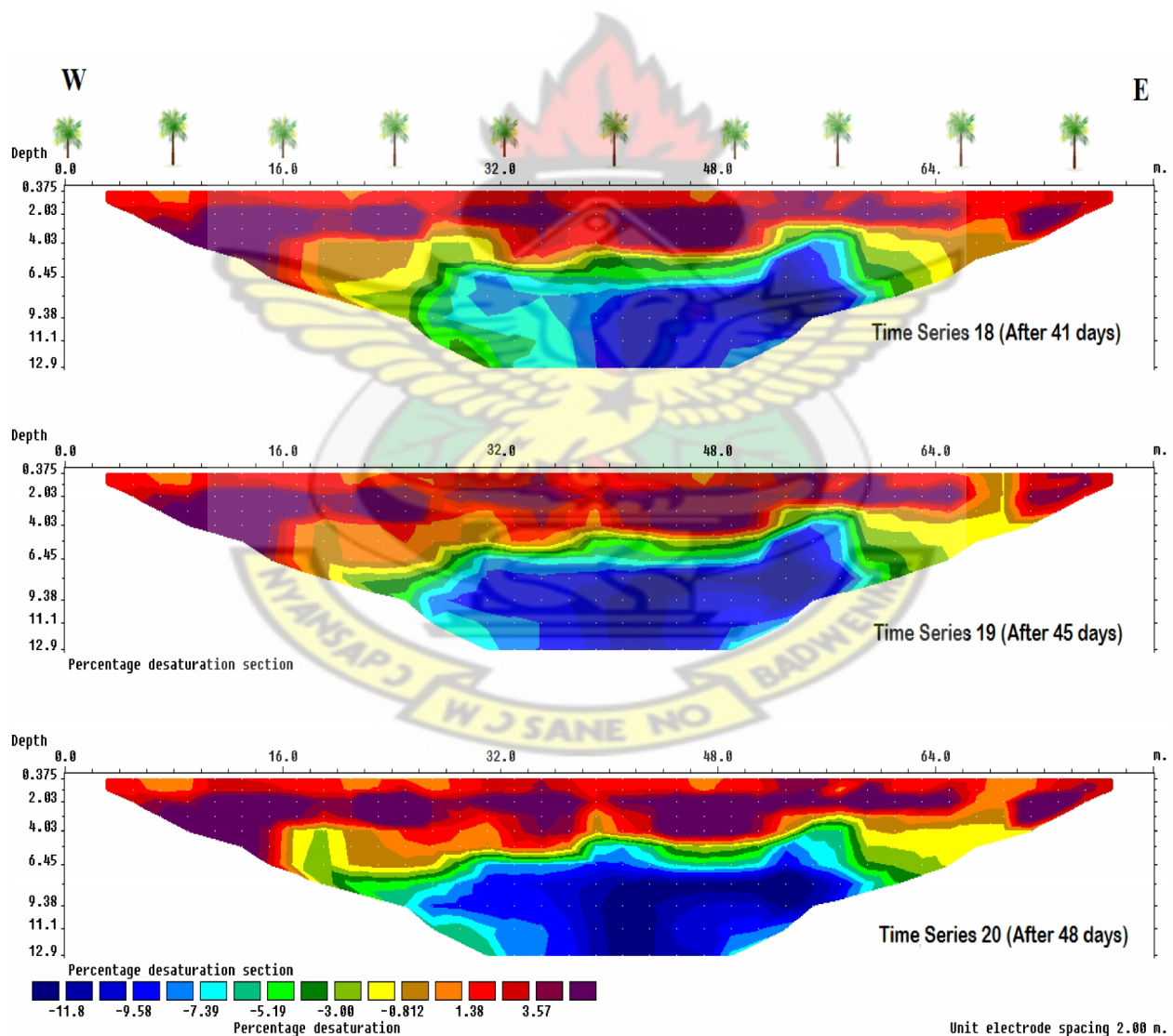


Figure 4.19: Desaturation models for 19th, 23rd and 26th of August 2013

Time series 18 and 19 which represent desaturation model for the 19th and 23rd of August 2013, show high desaturation (2%) on the surface in Figure 4.19. Time series 20 however, shows patches of reduced desaturation (1%) due to antecedent rainfall and the levels of saturation shows that the material below 8 m are more saturated (-10% to -3%) with water compared to when the survey started.

The results in Figure 4.19 show that the top surface has lost more water at the time of measurement on the 26th of August 2013 (final measurement day) than it originally was when the survey began on the 9th of July 2013. The desaturation models therefore explain where most of the infiltrating water from rainfall goes and how soon water from the surface is lost.

The desaturation models therefore provide information on the water content (saturation) as measured over time on line 4 as displayed in Figure 4.18 and 4.19.

4.3 Comparison of Results

The estimates of the volumetric water content derived from the ground wave GPR and displayed as surface plots were compared with the 3D resistivity models. This was based on the fact that the ground wave records different velocities in different material with contrasting dielectric constants based on the water content since the frequency used was constant. Moreover, soil materials also have varied resistivity based on the water content; therefore, both methods would be able to detect changes in the subsurface based solely on the moisture content. The results for both techniques are examined in this section.

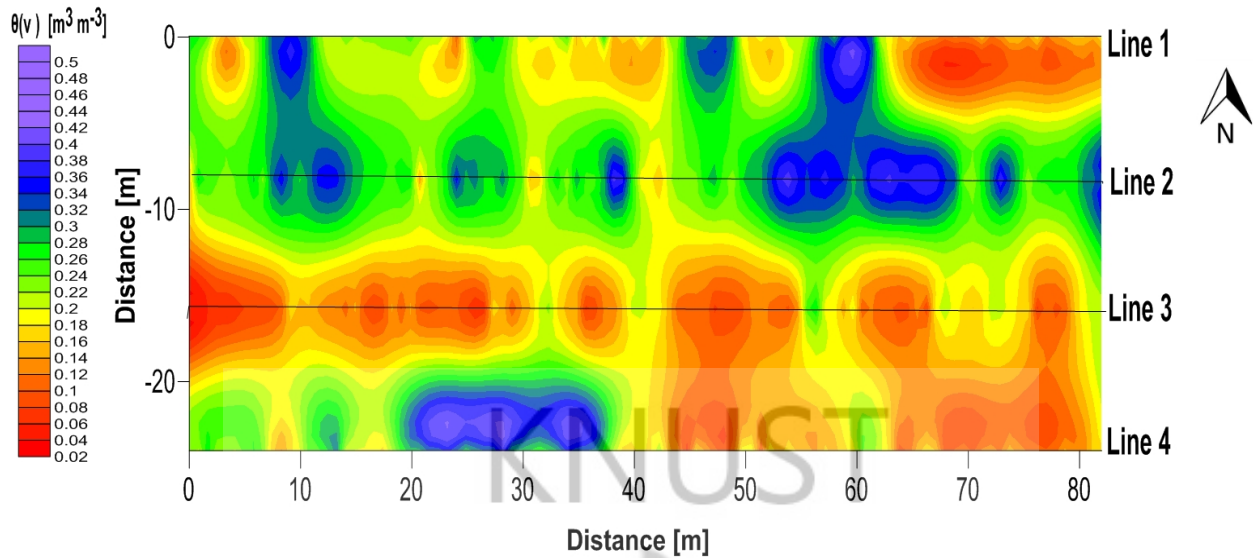


Figure 4.20: Spatial distribution of the volumetric water content for 9th of July 2013 at 0.1 m depth.

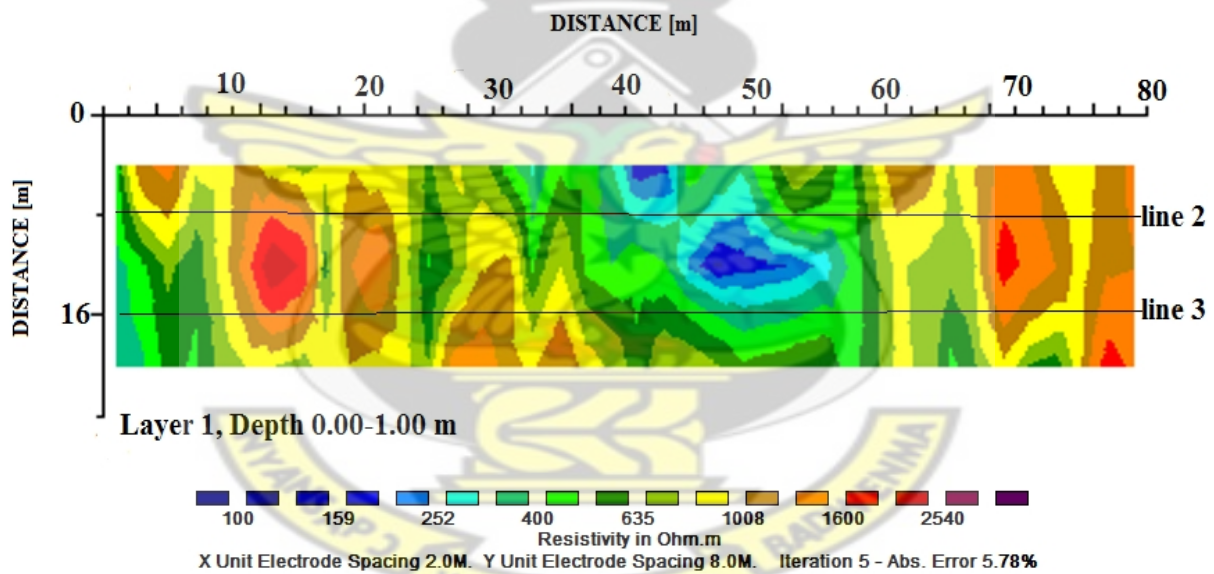


Figure 4.21: 3D resistivity model for the survey area on July 9th 2013.

Increase in water contents would decrease the resistivity of the topsoil. Therefore areas with high water contents are associated with low resistivity and this is evident on line 2 from the 30 m mark to 70 m on both results as displayed in Figures 4.20 and 4.21. This region records high

water content on Figure 4.20 and the resistivity model (Figure 4.21) shows results with low resistivities recorded from the 30 m mark as expected of areas with high degree of water saturation. The results displayed are for a day where antecedent rainfall was recorded. The land sloped gently towards the east; some water was expected to accumulate at lower regions at the east of the line towards the 80 m mark. This explains why high water content was recorded at the end of the profile from the 50 m mark on the Figure 4.20 whereas low resistivities are seen on the resistivity models.

The 20 m stretch of high resistivity recorded on line 3 from 10 to 30 m and also from 60 m to 80 m indicates the lack of soil water at those regions of the field hence the corresponding low moisture measurement (Figure 4.20).

Figures 4.22 and 4.23 show the surface plot and 3D resistivity models for the 26th of August 2013 respectively. These results are for a day where antecedent rainfall was recorded. The surface plots clearly shows high water content across the field. The resistivity model however, shows high resistivities. This could be attributed to the fact that, the intensity of precipitation is low such that, it does not allow for infiltration as in the case of rain showers; the water molecules are therefore found in just a few centimeters of the soil, and the resistivity method is unable to detect this due to the electrode spacing (depth of probe) and the fact that the average of the resistivity (in this case to a depth of 1 m) for the area would not be affected much.

Also, the 3D resistivity models could not provide clear information on lines 1 and 4 except that, interpolation can be used to indicate the resistivities of those area. However, the very low resistive region between lines 2 and 3 shows high water content in the surface plot.

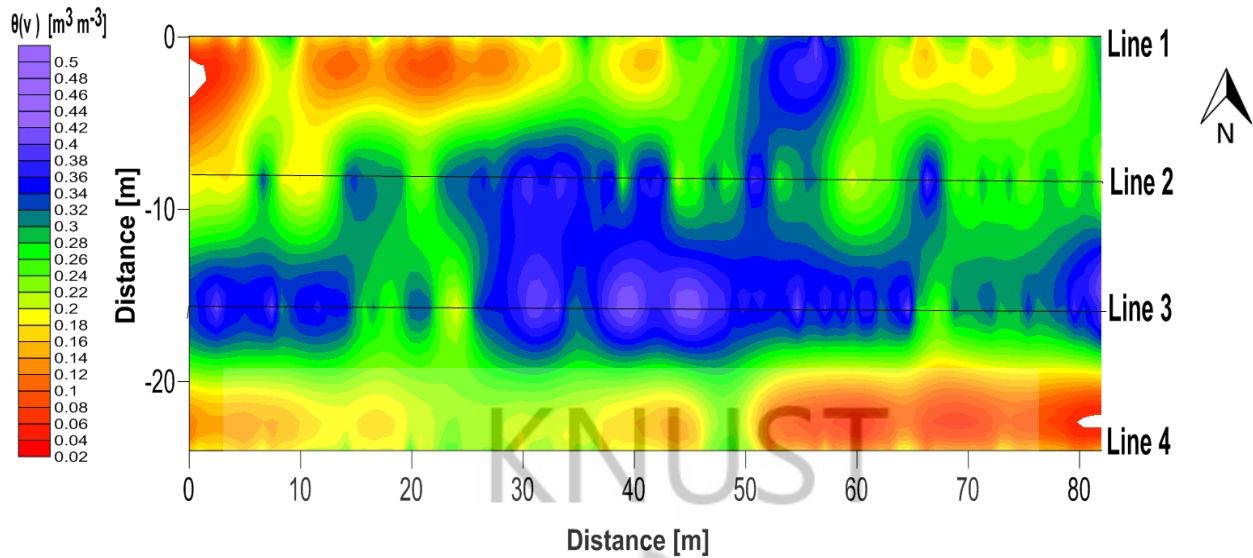


Figure 4.22: Surface plot of volumetric water content for 26th August 2013 to 0.1 m depth

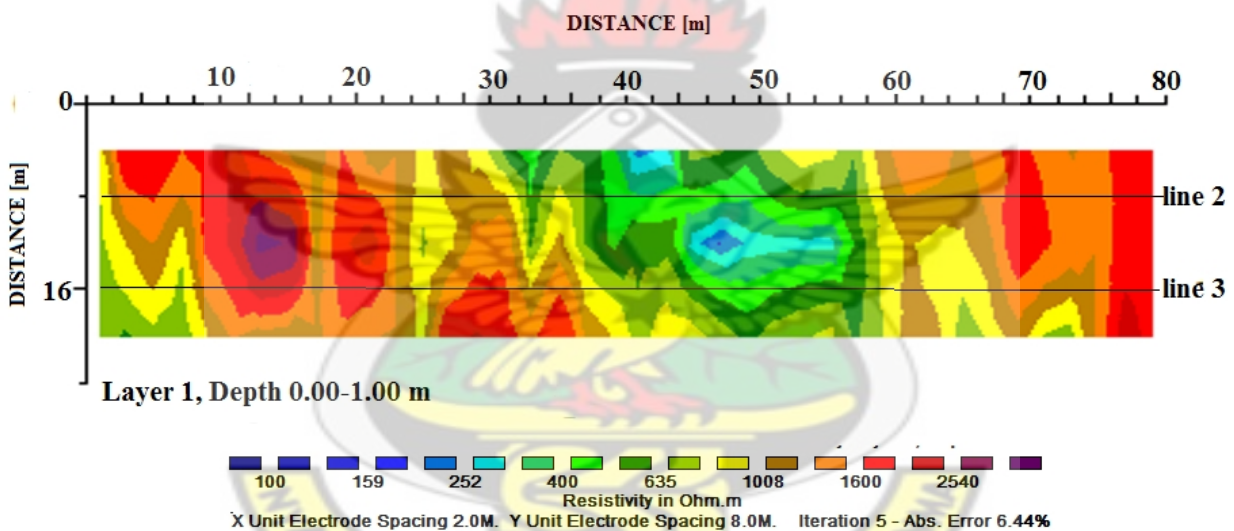


Figure 4.23: 3D resistivity model for the field on 26th August 2013

The comparison of the results for both methods shows very interesting occurrence. In most cases, the low resistivity regions in the models show high volumetric water content. This could be attributed to the fact the area could be made of up clay-loam. Normally, clays absorb less water at a slower rate than the sandy loam. Their water holding abilities also explain why little changes

were recorded in the results for the temporal variations. In general, the results for both measurements agree with each other.

4.4 Summary of Results

A portion of the water that falls as rains infiltrates into the subsurface soil. The amount that infiltrates depends greatly on a number of factors such as soil porosity and permeability. Some of the water that infiltrate will remain in the shallow soil layer from where it gradually moves vertically and horizontally through the soil and subsurface materials. Others may infiltrate deeper, recharging groundwater aquifers. This can be observed with the time-lapse resistivity and desaturation models.

The main factor that controls infiltration is the amount and characteristics (intensity, duration) of precipitation that falls as rain. Also, the characteristics of the subsurface soil influence the rate of infiltration. Some soils such as clay absorb less water at a slower rate than sandy soils. Soils absorbing less water and/or already saturated from previous rainfall cannot absorb much more thus more rainfall will become surface runoff.

Vegetation aids in the slow movement of surface runoff thereby allowing more time for it to seep into the ground. However, since the vegetation was cleared at the site, runoff was increased while hard/compacted grounds aided runoff. When the rain hits the saturated or compacted ground, it begins to flow overland downhill to the east of the survey area. The results shows that rain that fall on steeply-sloped land runs off more quickly and infiltrates less compared to areas that are fairly flat. This was evident in the recorded volumetric water content for the up slope area on the west compared to the down slope area on the east (towards the 80 m mark).

Some infiltration stays near the land surface, within the reach of the oil palm plant roots. The oil palm plant has an adventitious root system with primary roots from the base of the trunk and spreading horizontally or descending at varying angles into the soil. The primary roots bear secondary roots which in turn bear tertiary roots. The quaternary roots which branch out of the tertiary roots are assumed to be the main absorbing roots. (Corley et al., 1976). The tertiary and quaternary roots are found mostly in the upper 30 cm from the soil surface. Jourdan and Rey (1996) asserted that the total plant-available water in a soil profile is that held in all soil layers to the lowest depth from which roots can extract water. With oil palms, this depth limit has usually been taken as 100 - 200 cm, which included nearly all the fine roots. . The plants need this shallow groundwater to grow, and also by the process of evapotranspiration, water is moved back into the atmosphere and this leads to the temporal decrease in the water content.

In all cases, the top layer of the soil was often wet to some extent, but was not totally saturated as observed in the soil below the water table in the desaturation models. The soil above the water table got wet from rain water which infiltrated; but, it easily dried out without additional precipitation. Since the water table is usually below the depth of the plant root, the plants are dependent on the water supplied by precipitation.

Factors that affected the temporal and spatial variation of the soil moisture include the texture of the soil. It was observed that, probable finer textured soils like clay had more pore spaces due to the activities of earthworm and has greater water retention ability due to low permeability. Hence very little changes in water content are recorded over time. Their well-aggregated porous structure favours better porosity, which in turn enhance water retention. Also, areas with higher organic matter retain more moisture in the soil.

Compaction of soil due to the inevitable process of walking on the farm to take measurements and general farm operations might have led to the reduction of the porosities of the soil and consequent infiltration rate.

Finally, water lost through evaporation might have caused areas on the farm that are not shaded by the palm branches to lose water more rapidly compared to areas that are shaded. The shade provided by the palm leaves helped to reduce evaporation during dry periods.



CHAPTER 5

CONCLUSION AND RECOMMENDATIONS

5.1 Conclusion

The research has shown that GPR ground wave data can be used efficiently and effectively as a field tool to accurately, non-invasively, and rapidly estimate shallow water content in field scale application.

The analysis of the travel time data produced reliable results within limited time compared with conventional point measurement techniques. The work proved that, GPR data can be employed to determine both the lateral and vertical distribution of soil water content; this can be done by employing antennas of different frequencies. The low frequencies would be used to probe greater depths than the high. The common-offset (CO) travel time data was useful in investigating the depth of influence of the ground wave using 200 MHz antenna hence the observation.

The GPR is a useful tool for these applications because the spatial density of conventional point measurements of water content is typically insufficient to capture the complete pattern of soil moisture over a large area, and due to the variability of water content, a few point measurements may indicate an incorrect water content distribution. The GPR ground wave measurements can however, be used to image the spatial and temporal variation of soil moisture as shown with this work.

The results of this work showed that water content at this field site is heterogeneous along each profile and is dependent on the type of soil in the zone between 7 and 10 cm below the ground

surface. The water content ranges from $0.06 \text{ m}^3\text{m}^{-3}$ to $0.4 \text{ m}^3\text{m}^{-3}$. It also showed that, the 200 MHz antenna is capable of capturing this heterogeneity.

The GPR estimates of water content could also be used to indicate soil texture, so GPR measurements could be used to identify soil conditions. The temporal persistence of the spatial distribution of water content as seen on some occasions and the similarity of this pattern to the soil texture composition distribution suggest that soil type is a controlling factor on near surface soil water content at the site.

The results from this experiment can be applied to improve agricultural practices. By estimating the soil water content before starting irrigation, the optimal scheduling and amount of irrigation can be determined, and irrigation can be applied non-uniformly across field as needed.

In general, the results presented in this study showed that GPR ground waves can be used as a field tool for estimating volumetric water content.

The comparison of the time-lapse models with the values measured by the ground wave GPR along the four profile lines led to slight differences on average. These results are relatively conclusive and offer interesting prospects. Ground wave GPR measurements indeed have these advantages over electrical resistivity measurements: fast, non-destructive and non-invasive. Also, electrical resistivity has the following advantages over the ground wave GPR measurements: the opportunity to probe greater depths and characterize the structure of the whole soil profile.

However, the interpretation of electrical resistivity measurements remained complex. Given the different factors on which they depend: porosity, temperature, pore-water resistivity and water content.

This work therefore opens interesting prospects for the use and exploitation of electrical resistivity measurements for the assessment of soil water content through imaging.

The resistivity models of soil moisture however, do not resolve small-scale (< 0.3 m) heterogeneity in soil moisture as measured with GPR, but instead represent smoother models which averages these heterogeneities over a larger volume and reflect the inability of electrical resistivity tomography measurements to resolve small-scale differences.

This study has shown that the obtained models can be used to investigate the effects of water content on soil resistivity.

5.2 Recommendations

- To build on this research for use in agriculture, evaporation rates, soil porosities (to help in determining infiltration rates), and precipitation rates for the site should be obtained. This would help in quantifying how much water is taken up by the plant from precipitation by subtraction the other components. This information would be helpful in irrigation farming.
- Also, further research to study the dry and wet season variability can be explored.
- The resistivity technique could be repeated with smaller electrode spacing to help resolve smaller scale heterogeneity.
- Finally, collecting resistivity data with co-located GPR measurements could help create a more complete image of the water content distribution with depth.

REFERENCES

- Abu-Hassanein, Z.S., Benson, C.H. and Blotz, L.R., (1996). Electrical resistivity of compacted clays. *Journal of Geotechnical Engineering* 122 (5), 397–406.
- Ahuja, L.R., Wendroth, O. and Nielsen, D.R. (1993). Relationship between initial drainage of surface soil and average profile saturated conductivity. *Soil Sci. Soc. Am. J.* 57:19–25.
- Aning A. A., Sackey N., Jakalia I. S., Sedoawu O., Tetteh E. H., Hinson G., Akorlie R. K., Appiah D. and Quaye E. K. (2014). Electrical Resistivity as a Geophysical Mapping Tool; A Case Study Of The New Art Department, KNUST-Ghana. *Int. Journal of Scientific and Research Publications*, 4 (1).
- Archie, G.E., (1942). The electrical resistivity log as an aid in determining some reservoir characteristics. *Trans. AM. Inst. Min. Metall. Pet. Eng.* 146, 54–62.
- Auerswald, K., Simon, S. and Stanjek, H., (2001). Influence of soil properties on electrical conductivity under humid water regimes. *Soil Sci. Soc. Am. J.* 166 (6), 382–390.
- Barker, R. and Moore, J., (1998). The application of time-lapse electrical tomography in groundwater studies. *The Leading Edge* (October), 1454–1458.
- Basson U., (1992). Mapping of moisture content and structure of unsaturated sand layers with ground penetrating radar. Thesis submitted for the degree of master of Sciences in Geophysics, October 1992, Tel-Aviv University, Raymond and Beverly Sackler, Faculty of Exact Sciences, Department of Geophysics and Planetary Sciences, 80 p.
- Baver, L. D., Gardner, W. H., Gardner, W. R. (1997). *Soil Physics*. Wiley, New York.

- Bouten, W., Heimovaara, T.J., Tiktak, A. (1992). Spatial patterns of throughfall and soil water dynamics in a Douglas fir stand. *Water Resources Res.* 28:3227–3233.
- Cassidy, N.J., (2009). Electrical and Magnetic properties of rocks, soils and fluid; in Ground Penetrating radar theory and application. *Elsevier Science* 41-64
- Chanzy, A., Tarussov, A. Judge, A., Bonn, F. (1996). Soil water content determination using a digital ground-penetrating radar. *Soil Sci. Soc. Am. J.* 60:1318–1326.
- Corley, R.H.V., J.J. Hardon and B.J. Wood, (1976). Oil Palm Research. Elsevier Scientific Publishing Company, Holland, pp: 532.
- Daily, W., Ramirez, A., LaBrecque, D., and Nitao, J. (1992). Electrical resistivity tomography of vadose water movement. *Water Resources Res.* Vol.28, 5. p. 1429-1442.
- Davis, D.W., Hirdes, W., Schaltegger, E. Nunoo, E. A. (1994). U/Pb age constraint on deposition and Provenance of Birimian and gold-bearing Tarkwaian sediments in Ghana, West Africa. *Precamb. Res* 67.89 107.
- Davis, J.L. and Annan, A.P., (1989). Ground penetrating radar for high resolution mapping of soil and rock stratigraphy. *Geophysical prospecting*, Vol. 37, p. 531-551.
- Du, S. (1996). Determination of water content in the subsurface with the ground wave of ground penetrating radar. Ph.D. thesis. Ludwig-Maximilians-Universitat, Munich, Germany.
- Du, S. and Rummel, P. (1994). Reconnaissance studies of moisture in the subsurface with GPR. p. 1241–1248. *In Proc. Int. Conf. on Ground Penetrating Radar*, 5th. Waterloo Centre for Groundwater Research, Waterloo, Kitchener, ON, Canada.

- Entekhabi, D., Asrar, G.R., Betts, A.K., Beven, K.J., Bras, R.L., Duffy, C.J., Dunne, T., Koster, R.D., Lettenmaier, D.P., McLaughlin, D.B., Shuttleworth, W.J., van Genuchten, M.Th., Wei, M.Y. and Wood, E.F. (1999). An agenda for land surface hydrology research and a call for the second international hydrological decade. *Bull. Am. Meteorol. Soc.* 80:2043–2058.
- Galagedara, L. W., Parkin, G. W. and Redman, J. D. (2003). An analysis of the ground penetrating radar direct ground wave method for soil water content measurement. *Hydrological Processes*, 17 (18):3615–3628
- Gardner, M. K. C., Robinson, D., Blyth, K., and Cooper, J. D. (2001). Soil water content. In *Soil and Environmental Analysis*, pages 1–64. Marcel Dekker, New York.
- Ghana Geological Survey (2009). Geological map of Kumasi Metropolis.
- Grayson, R.B., Western, A.W., Chiew, F.H.S. and Blöschl, G. (1997). Preferred states in spatial soil moisture patterns: Local and non local controls. *Water Resources Res.* 33:2897–2908.
- Griffis, J. R, Barning K., Agezo L. F. and Akosah K.F (2002). Gold Deposit of Ghana, mineral commission. Gandalf Graphics Limited, 605 Alden Rd., Markham, Ontario, Canada.
- Grote, K., Hubbard S. and Rubin Y. (2003). Field-Scale Estimation of Volumetric Water Content using GPR Ground wave Techniques. Dept. of Civil and Env. Engineering, UC Berkeley, Berkeley, CA

- Hamzah, U., Yaacup, R., Samsudin, A. R. and Ayub, M. S. (2006). Electrical Imaging of the Groundwater Aquifer at Banting, Selangor, Malaysia, *Environmental Geology* 49, Issue 8, pp. 1156–1162.
- Hirdes, W., Davis, D., and Eisenlohr, B. (1992). Reassessment of Proterozoic granitoid ages in Ghana on the basis of U/Pb zircon and monazite dating. *Precambrian Res.*, 56, 89-96.
- Hoeben, R. and Troch, P.A. (2000). Assimilation of active microwave observation data for soil moisture profile estimation. *Water Resources Res.* 36:2805–2819.
- Huisman, J.A., Hubbard, S.S., Redman, J.D., and Annan, A.P. (2003a). Measuring soil water content with ground penetrating radar: A Review. *Vadose zone J.* 2: 476—491. Soil Science Society.
- Huisman, J.A., Snepvangers, J.J.J.C., Bouten, W. and Heuvelink, G.B.M. (2003b). Monitoring temporal development of spatial soil water content variation: Comparison of ground penetrating radar and time domain reflectometry. *Vadose Zone J.* 2:519–529.
- Hupet, F. and Vanclooster, M. (2002). Intraseasonal dynamics of soil moisture variability within a small agricultural maize cropped field. *J. Hydrol.* (Amsterdam) 261:86–101.
- <http://www.kma.ghanadistrict.gov.gh>, Vegetation of Research site retrieved 20th October, 2014
- <http://www.worldweatheronline.com>, Rainfall rates. Retrieved 14th January, 2014.
- <http://www.worldbank.org>, GDP of Ghana. Retrieved 12nd October, 2014.
- Jackson, T.J. and Le Vine, D.E. (1996). Mapping surface soil moisture using an aircraft-based passive microwave instrument: Algorithm and example. *J. Hydrol.* (Amsterdam) 184:85–99.

- Jol, H.M. and Bristow C.S (2003): GPR in sediments: advice on data collection, basic processing and interpretation, a good practice guide. – In Bristow C S, Jol H M (eds.) Ground penetrating radar in sediments. Geological Society, London Special Publications 211: 9–27.
- Jourdan, C. and Rey B. (1996). Oil palm root architecture: modeling and simulation. *J. of Am. Soc. for horticultural Sci.*
- Kalinski, R.J. and Kelly, W.E., (1993). Estimating water content of soils from electrical resistivity. *Geotechnical Testing J.* 16 (3), 323–329.
- Kalinski, R.J., Kelly, W.E., Bogardi, I. and Pesti, G., (1993). Electrical resistivity measurements to estimate travel times through unsaturated ground water protective layers. *J. of Applied Geophysics* 30 (3), 161–173.
- Kearey, P., Brooks, M., Hill, I., (2002). An introduction to geophysical exploration. Blackwell Scientific Publications.
- Kesse, G. (1985). The mineral and rock resources of Ghana. United States: A.A. Balkema Publishers Accord, MA.
- Lampe, B and Holliger, K., (2003). Effects of fractural fluctuations in topographic relief, permittivity and conductivity on ground penetrating radar antenna radiation. *Soc. Of Expl, Geophysicist* 68 (6) 1934-1944.
- Loke, M.H. (2000). Electrical imaging surveys for environmental and engineering studies; A practical guide to 2D and 3D surveys.
- Loke, M. H, (2011). Tutorial: 2-D and 3-D Electrical Imaging Survey Manual.

- Loke, M.H, Acworth I. and Dahlin T. (2003). A comparison of smooth and blocky inversion methods in 2-D electrical imaging surveys. *Explora.Geophysics*, 34:183–187.
- Loke, M.H., (1999). Time-lapse resistivity imaging inversion. Proceedings of the 5th Meeting of the Environmental and Engineering Geophysical Society European Section, Em1.
- Merz, B. and Bardossy. A. (1998). Effects of spatial variability on the rainfall runoff process in a small loess catchment. *J. Hydrol.(Amsterdam)* 212–213:304–317.
- Merz, B. and Plate. E.J. (1997). An analysis of the effects of spatial variability of soil and soil moisture on runoff. *Water Resources Res.* 33:2909–2922.
- Mitchell, V., Knight, R., and Pidlisecky, A. (2011). Inversion of time-lapse electrical resistivity imaging data for monitoring infiltration. *The Leading Edge* vol.30, # 2 p.140-144)
- Mualem, Y. and Friedman, S.P., (1991). Theoretical prediction of electrical conductivity in saturated and unsaturated soil. *Water Resources Res.* 27 (10), 2771–2777.
- Nadler. A., Dasberg S. and Lupid, I., (1991). Water content and electrical conductivity determination of layered soil profiles using time domain reflectometry. *Soil Sci. Soc. Am. J.*, 55: 938-943.
- Nielsen, D. R., Biggar, J. W. and Erh, K. T. (1973). Spatial variability of field measured soil water properties. *Hilgardia*, 42:215–259.
- Pauwels, V.R.N., Hoeben, R., Verhoest, N.E.C. and De Troch, F.P. (2001). The importance of the spatial patterns of remotely sensed soil moisture in the improvement of discharge predictions for small-scale basins through data assimilation. *J. Hydrol. (Amsterdam)* 251:88–102.

- Preetz, H., Altfelder, S. and Igel, J. (2008). Tropical soils and landmine detection – an approach for a classification system. *Soil Sci. Soc. Am. J.*, 72, 151–159.
- Preko, K (2007). Volumetric soil water determination using ground penetrating radar (GPR). Ph.D Thesis, Geophysical institute, University of Karlsruhe.
- Preko, K. and Wilhelm, H. (2012). Volumetric soil water content monitoring of a dike model using GPR techniques. *Innovative Feuchtemessung in Forschung und Praxis*, 2:65–71.
- Rinaldi, V.A., Cuestas, G.A., (2002). Ohmic conductivity of a compacted silty clay. *Journal of Geotechnical and Geoenvironmental Engineering* 128 (10), 824–835.
- Ritsema, C.J. (1999). Special issue: Preferential flow of water and solutes in soils. *J. Hydrol.* (Amsterdam) 215:1–3.
- Ritsema, C.J. and Dekker, L.W. (1998). Three-dimensional patterns of moisture, water repellency, bromide and pH in a sandy soil. *J. Contam. Hydrol.* 31:295–313.
- Robinson, D., Jones, S., Wraith, J., Or, D. and Friedman, S., (2003). A review in dielectric and electrical conductivity measurements in soils using time domain reflectometry, *Vadose Zone J.* 2:444–475.
- Samouëlian, A., Cousin, I., Tabbagh, A., Bruand, A. and Richard, G., (2005). Electrical resistivity survey in soil science: a review. *Soil Till. Res.* 83 (2), 173–193.
- Sandmeier, K.J. (1998). Windows 9x/NT/2000/XP/7 – program for processing of seismic, acoustic or electromagnetic reflection, refraction and transmission data; Reflexw manual.
- Schlesinger, W.H. (1997). Biogeochemistry: an Analysis of Global Change, volume 2. Academic Press, San Diego, CA. Chapter 10: The Water Cycle.

- Singha, K. and Gorelick, S.M., (2006). Effects of spatially variable resolution on field-scale estimates of tracer concentration from electrical inversions using Archie's Law. *Geophysics* 71 (3), G83–G91.
- Sperl, C. (1999). Determination of soil water content in an agro-ecosystem using the ground wave of ground penetrating radar. PhD thesis, University Of Munich.
- Stratton, J.A. (2007) Electromagnetic theory. John Wiley and Sons vol. 33
- Takahashi, K., Igel J., Preetz, H. and Kuroda, S. (2012). Basics And Application Of Ground Penetrating Radar As A Tool For Monitoring Irrigation Process, Problems And Challenges Of Agricultural Water Management. InTech.
- Titov, K., Kemna, A., Tarasov, A. and Vereecken, H., (2004). Induced polarization of unsaturated sands determined through time domain measurements. *Vadose Zone Journal* 3 (4), 1160–1168.
- Topp, G.C, Davis J.L, and Annan, A.P. (1980): Electromagnetic determination of soil water content: Measurements in coaxial transmission lines.–*Water Resources Research* 16: 574–582.
- Topp, G. C. and Davis, J. L. and Annan, A. P. (1982). Electromagnetic determination of soil water content using TDR: In applications to wetting fronts and steep gradients. *Soil Sci. Soc. Am. J.*, 46:672–678.
- Ulaby, F.T., Moore, M.K and Fung A.K. (1986). Microwave remote sensing, Active and Passive vol. 2 Artech house Norwood MA.

- van Overmeeren, R.A., Sariowan, S.V. and Gehrels, J.C. (1997). Ground penetrating radar for determining volumetric soil water content: Results of comparative measurements at two sites. *J. Hydrol.* (Amsterdam) 197:316–338.
- Weihermuller, L., Huisman, J.A., Lambot, S, Vereecken, H and Herbst, M. (2007). Mapping the spatial variation of soil water content at the field scale. Elsevier
- Weiler, K.W., Steenhuis, T.S., Boll, J. and Kung, K-J.S. (1998). Comparison of ground penetrating radar and time domain reflectometry as soil water sensors. *Soil Sci. Soc. Am. J.* 62:1237–1239.
- Western, A.W., Blöschl, G. and Grayson, R.B. (1998). Geostatistical characterisation of soil moisture patterns in the Tarrawarra catchment. *J. Hydrol.* (Amsterdam) 205:20–37.
- Whalley, W.R. (1993). Considerations on the use of time domain reflectometry (TDR) for measuring soil water content, *J. Soil Sci.*; 44:1-9
- Whalley, W.R. and Bull, C.R., (1991). An assessment of microwave reflectance as a technique for estimating the volumetric water content of soil. *J. of Agricultural Engineering Res.* 50, 315–326.
- Whalley, W.R., Leeds-Harrison, P.B. and Bowman, G.E. (1991). Estimation of soil moisture status using near infrared reflectance. *Hydrological Processes* 5:321-327.
- Zegelin, S.J., White, I and Russell, G.F., (1992). A critique of the time domain reflectometry technique for determining field soil-water content. In: G.C. Topp and R.E Green (Editors), *Advances in Measurement of soil physical properties: Bringing Theory into Practice. Soil Sci. Soc. Am. J.* Madison, WI, USA. Special Publication 30:187-208.

APPENDIX A

```
#!/bin/bash

filename="Iarp005.2013.07.11.15.12.18"
file=${filename}.DAT
filename1="Iarp77.2013.08.30.11.18.10"
file1=${filename1}.DAT

awk 'NR==FNR{a[NR]=$1;next}{if (a[FNR]==$1) {print "1" > "3.txt"} else {print $0 > "3.txt"}}'
$file $file1
```

A 1: Script to compare files for equal data points

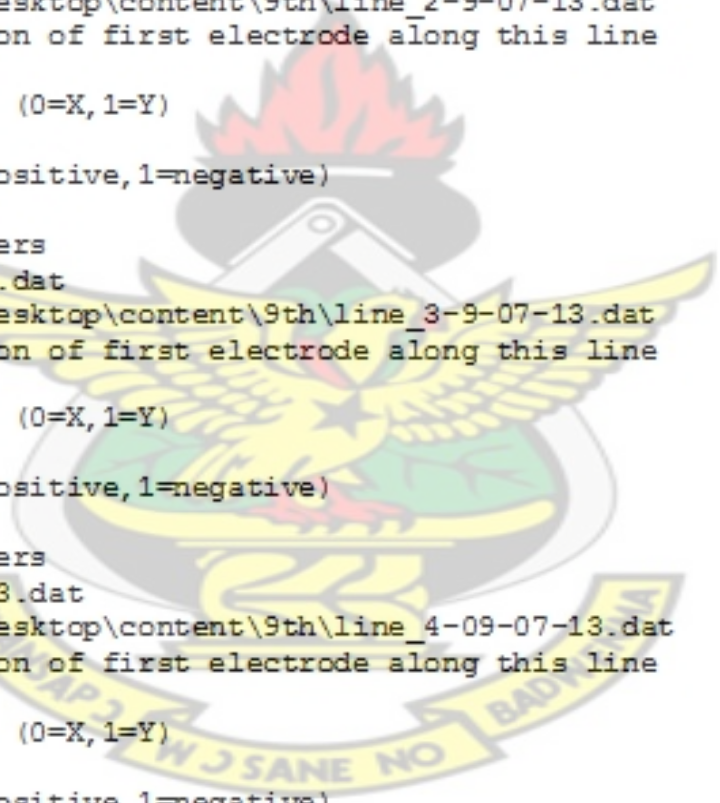
```
#!/bin/bash

filename="Iarp001.2013.07.09.15.09.18"
file=${filename}.DAT
filename1="Iarp005.2013.07.11.15.12.18"
file1=${filename1}.DAT
filename2="Iarp009.2013.07.11.15.12.18"
file2=${filename2}.DAT
filename3="Iarp013.2013.07.12.15.47.43"
file3=${filename3}.DAT
filename4="Iarp017.2013.07.16.15.55.15"
file4=${filename4}.DAT
filename5="Iarp021.2013.07.17.15.03.45"
file5=${filename5}.DAT
filename6="Iarp025.2013.07.19.15.16.01"
file6=${filename6}.DAT

paste $file $file1 $file2 $file3 $file4 $file5 $file6 | awk '{ printf "%1.2f\t%1.2f\t%3.6f\n", $1, $2, $3, $6,$9, $12, $15, $18, $21}'>
Palm.txt

#print column1 and 2 from file1.txt and column 2 from file2.txt
# and print the output as try.txt
#chmod +x scriptname -this gives permission to run script#
```

A 2: Sample script to join files



```

COLLATE_2D_3D.TXT file
Conversion of RES2DINV data files
Number of files to colate
4
File 1 parameters
line_1-09-07-13.dat
C:\Users\NAT\Desktop\content\9th\line_1-09-07-13.dat
X and Y location of first electrode along this line
0.0,0.0
Line direction (0=X,1=Y)
0
Line sign (0=positive,1=negative)
0
File 2 parameters
line_2-9-07-13.dat
C:\Users\NAT\Desktop\content\9th\line_2-9-07-13.dat
X and Y location of first electrode along this line
0.0,8.0
Line direction (0=X,1=Y)
0
Line sign (0=positive,1=negative)
0
File 3 parameters
line_3-9-07-13.dat
C:\Users\NAT\Desktop\content\9th\line_3-9-07-13.dat
X and Y location of first electrode along this line
0.0,16.0
Line direction (0=X,1=Y)
0
Line sign (0=positive,1=negative)
0
File 4 parameters
line_4-09-07-13.dat
C:\Users\NAT\Desktop\content\9th\line_4-09-07-13.dat
X and Y location of first electrode along this line
0.0,24.0
Line direction (0=X,1=Y)
0
Line sign (0=positive,1=negative)
0
Name of output file in RES3DINV format
C:\Users\NAT\Desktop\content\9th\File_3D.dat
End of file

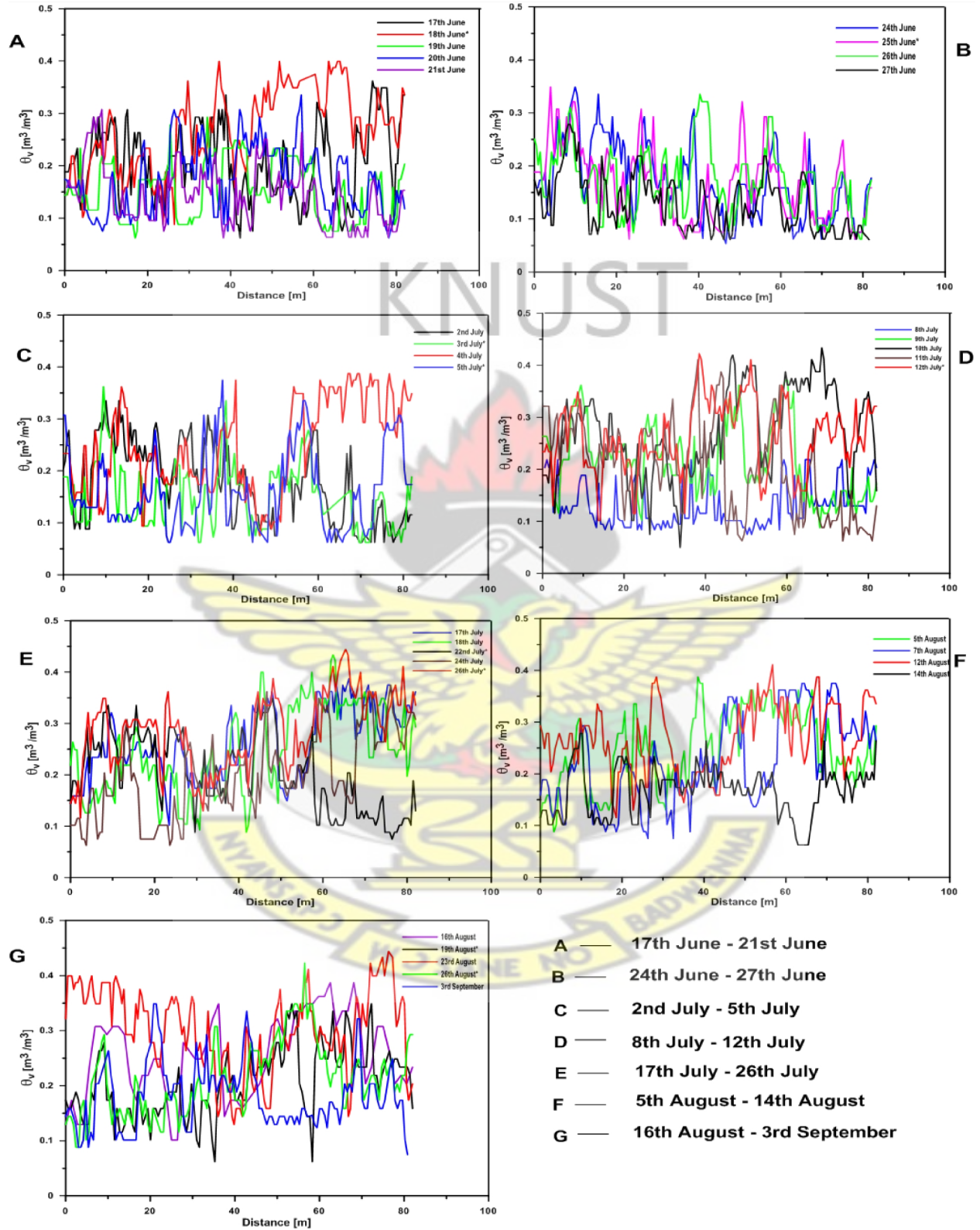
```

A 3: Script to collate 2D resistivity data into 3D

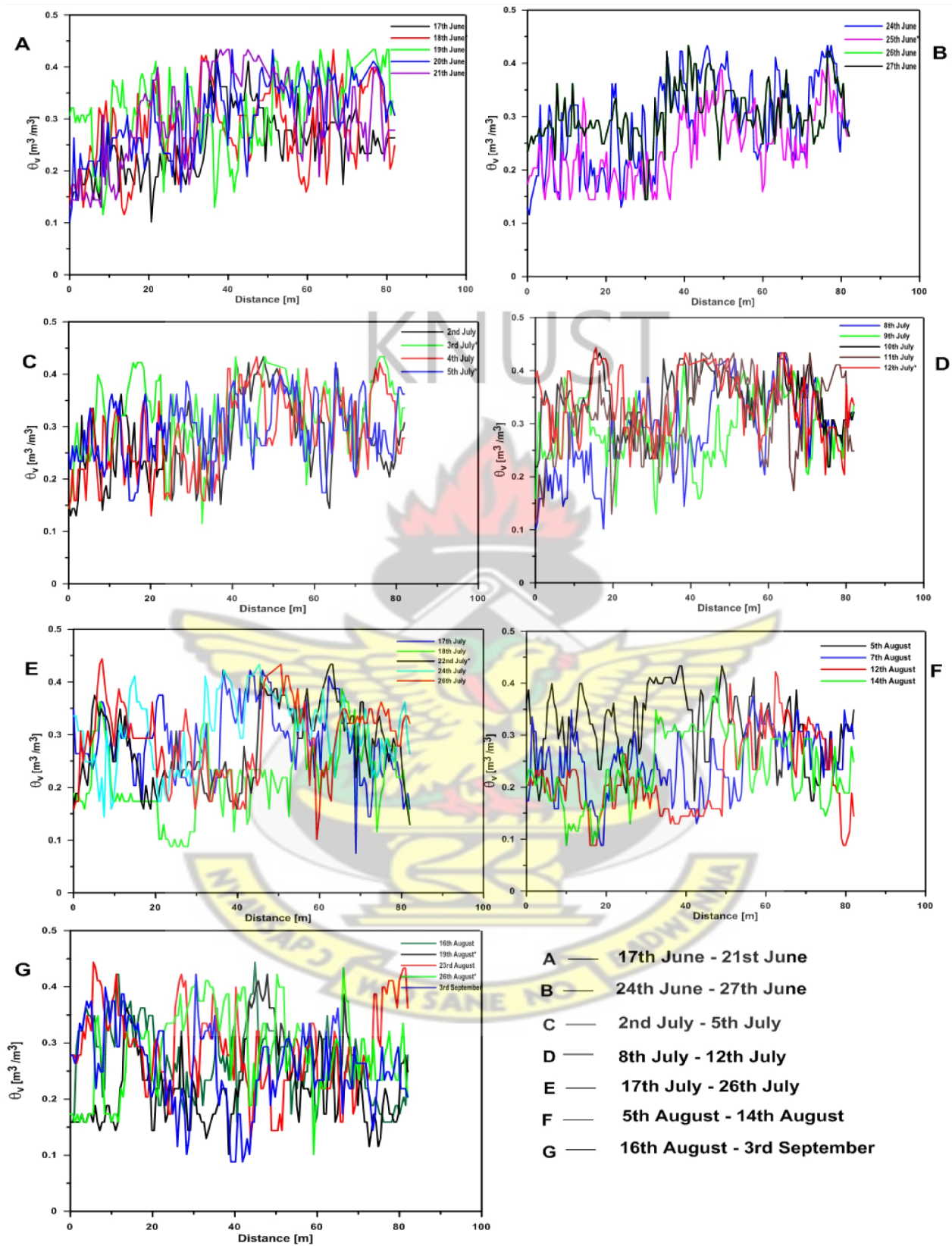
Table A 1: Measurement days and rainfall rates (www.worldweatheronline.com retrieved 14th January 2014)

Date	Amount of rain [mm]
17 th June 2013	0
18 th June 2013	4.0
19 th June 2013	2.0
20 th June 2013	1.7
21 st June 2013	1.3
24 th June 2013	0.6
25 th June 2013	1.4
26 th June 2013	0
27 th June 2013	0
2 nd July 2013	0
3 rd July 2013	3.8
4 th July 2013	4.4
5 th July 2013	6.9
8 th July 2013	2.5
9 th July 2013	12.8
10 th July 2013	0.5
11 th July 2013	4.5
12 th July 2013	7.0
17 th July 2013	6.0
18 th July 2013	0
22 nd July 2013	22.0
24 th July 2013	0
26 th July 2013	28.3
5 th August 2013	0
7 th August 2013	0
12 th August 2013	0
14 th August 2013	0
16 th August 2013	11.3
19 th August 2013	2.5
23 rd August 2013	0
26 th August 2013	7.5
3 rd September 2013	0

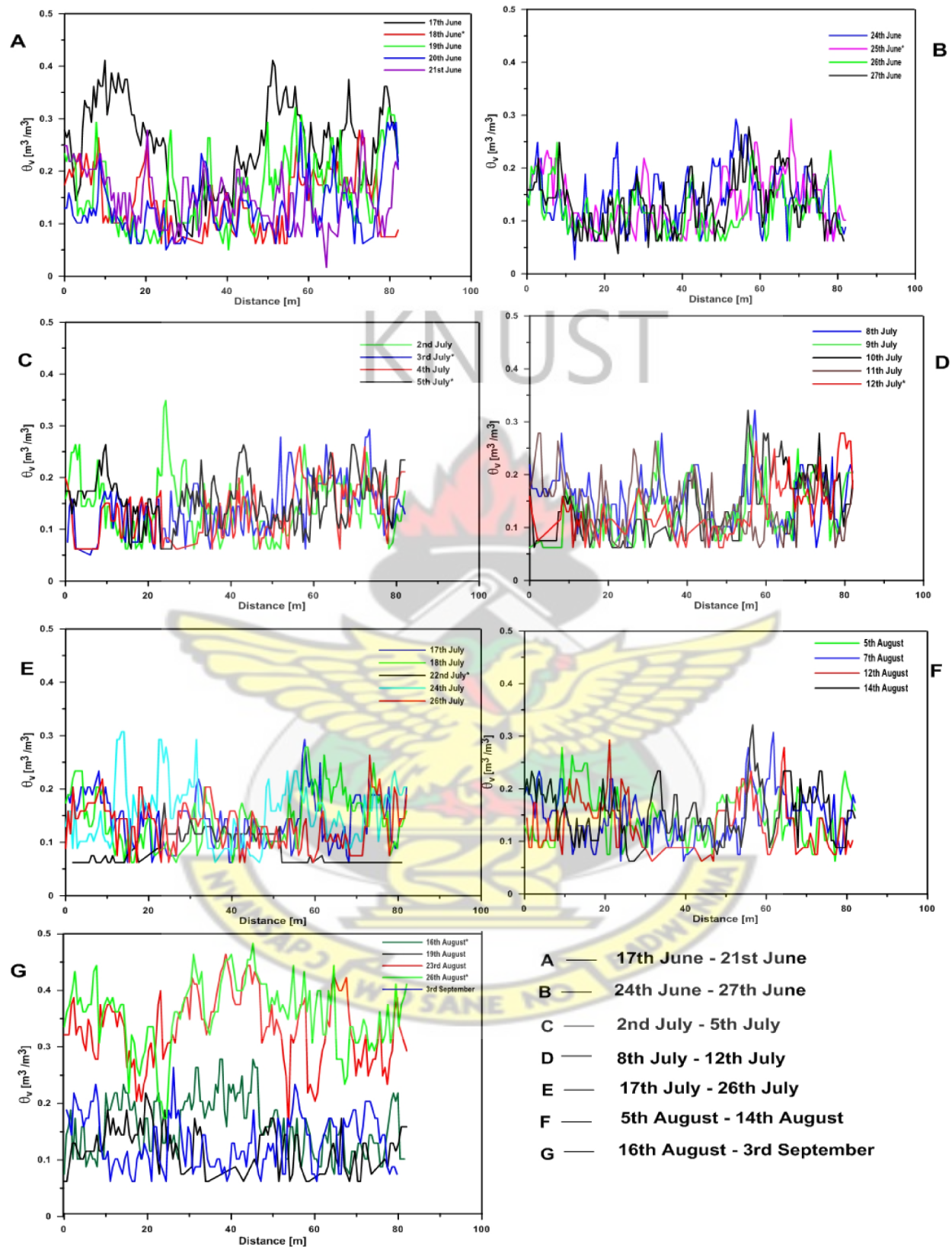
APPENDIX B



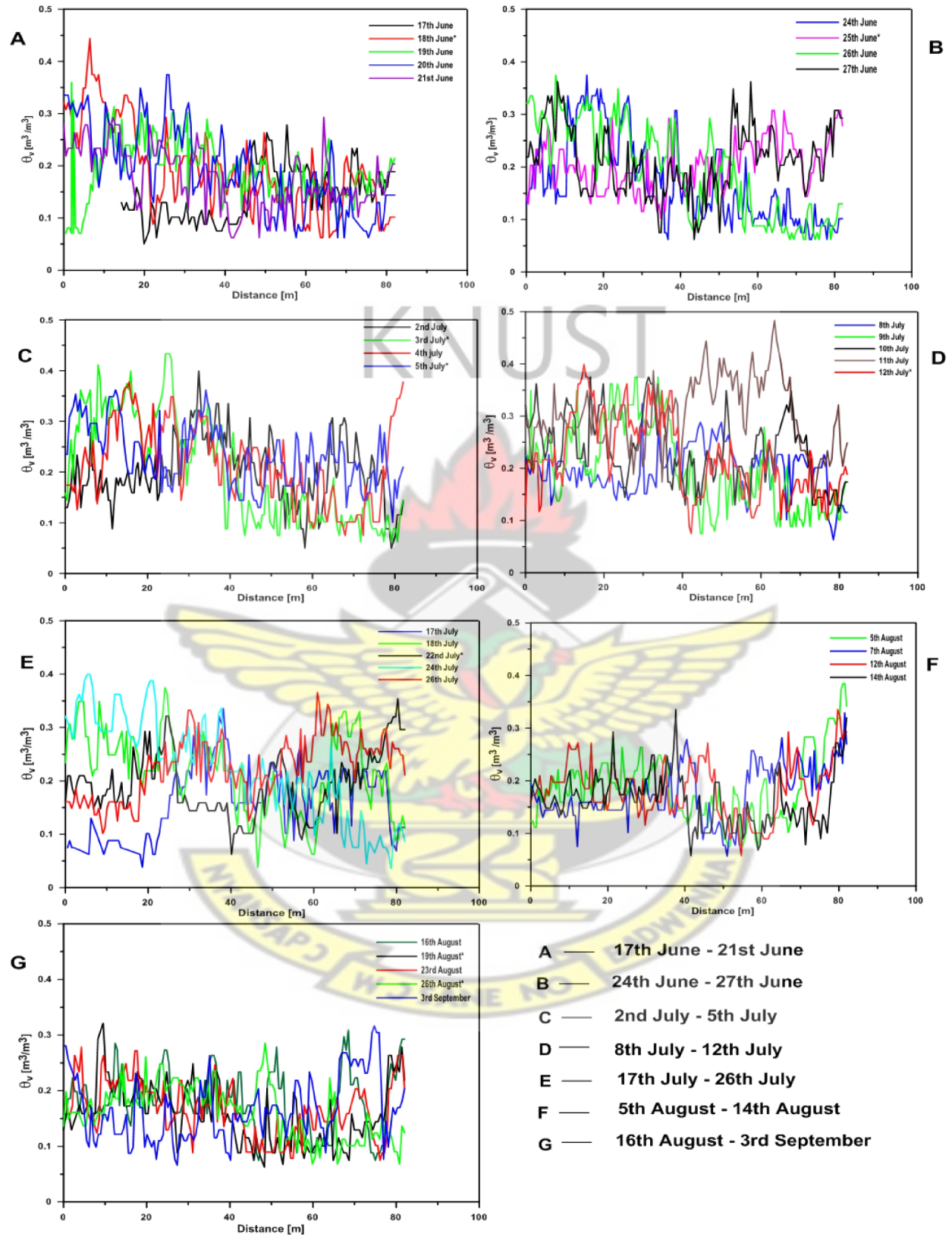
B 1: GPR result for line 1



B 2: Results for line 2

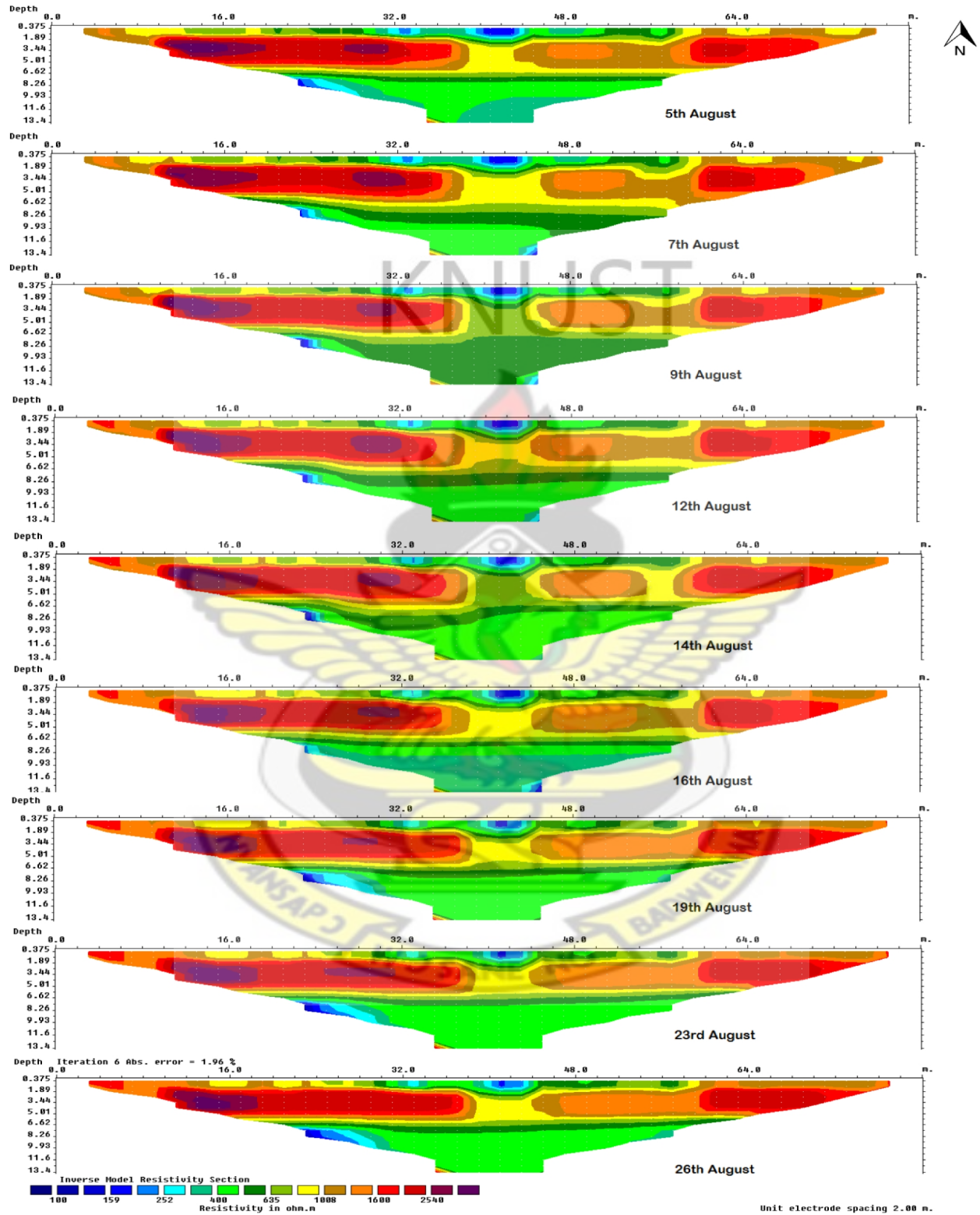


B 3: Results for line 3

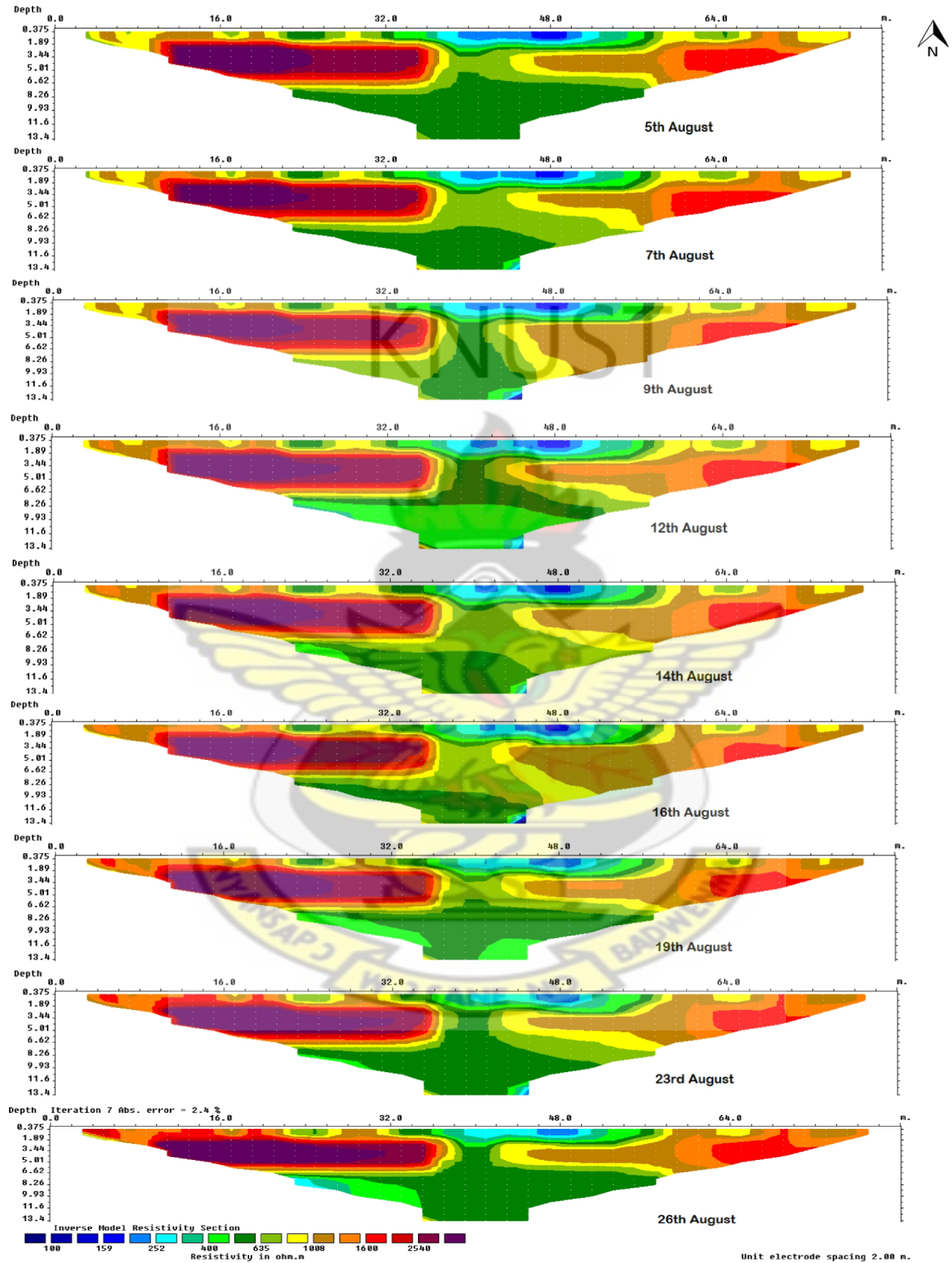


B 4: Results for line 4

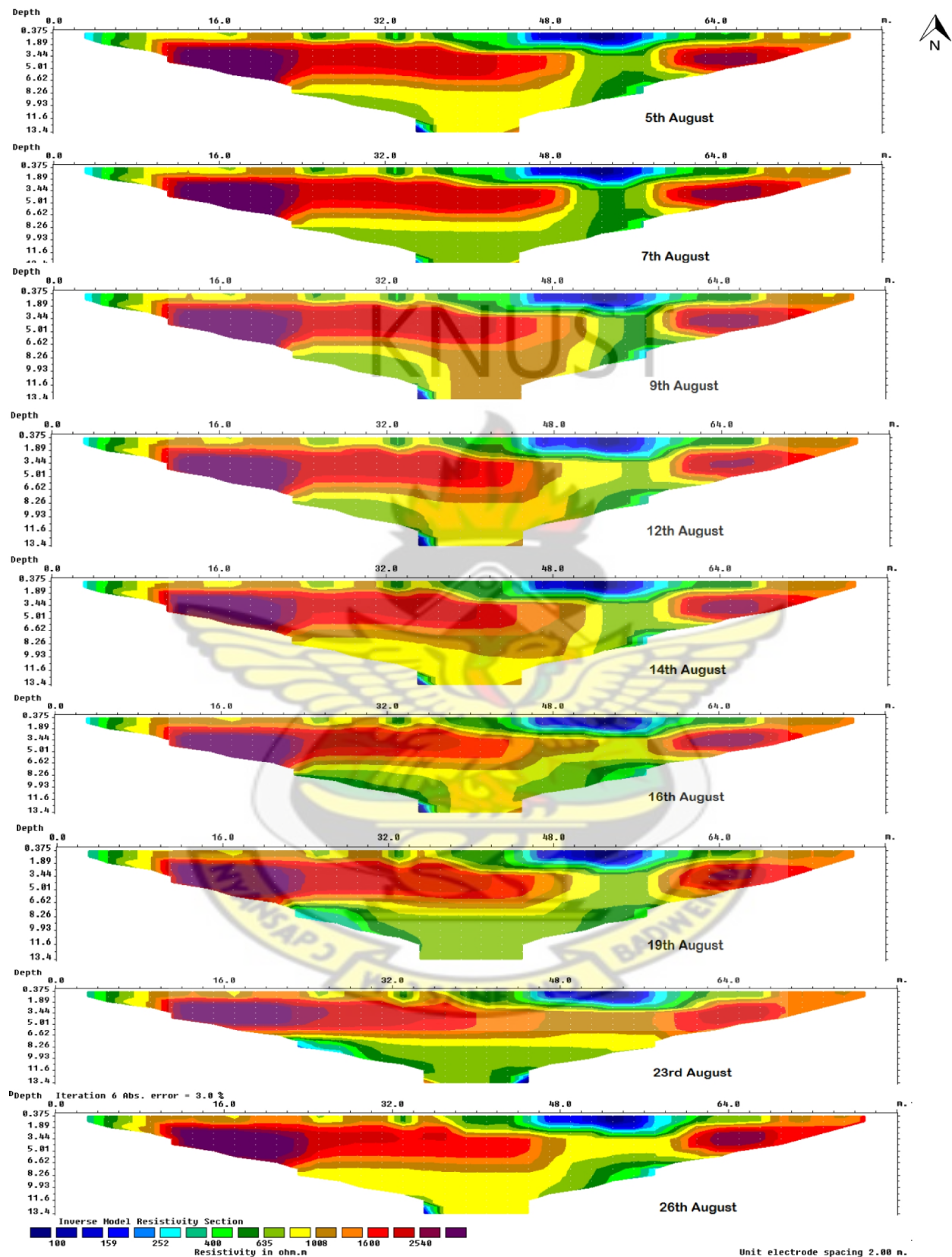
APPENDIX C



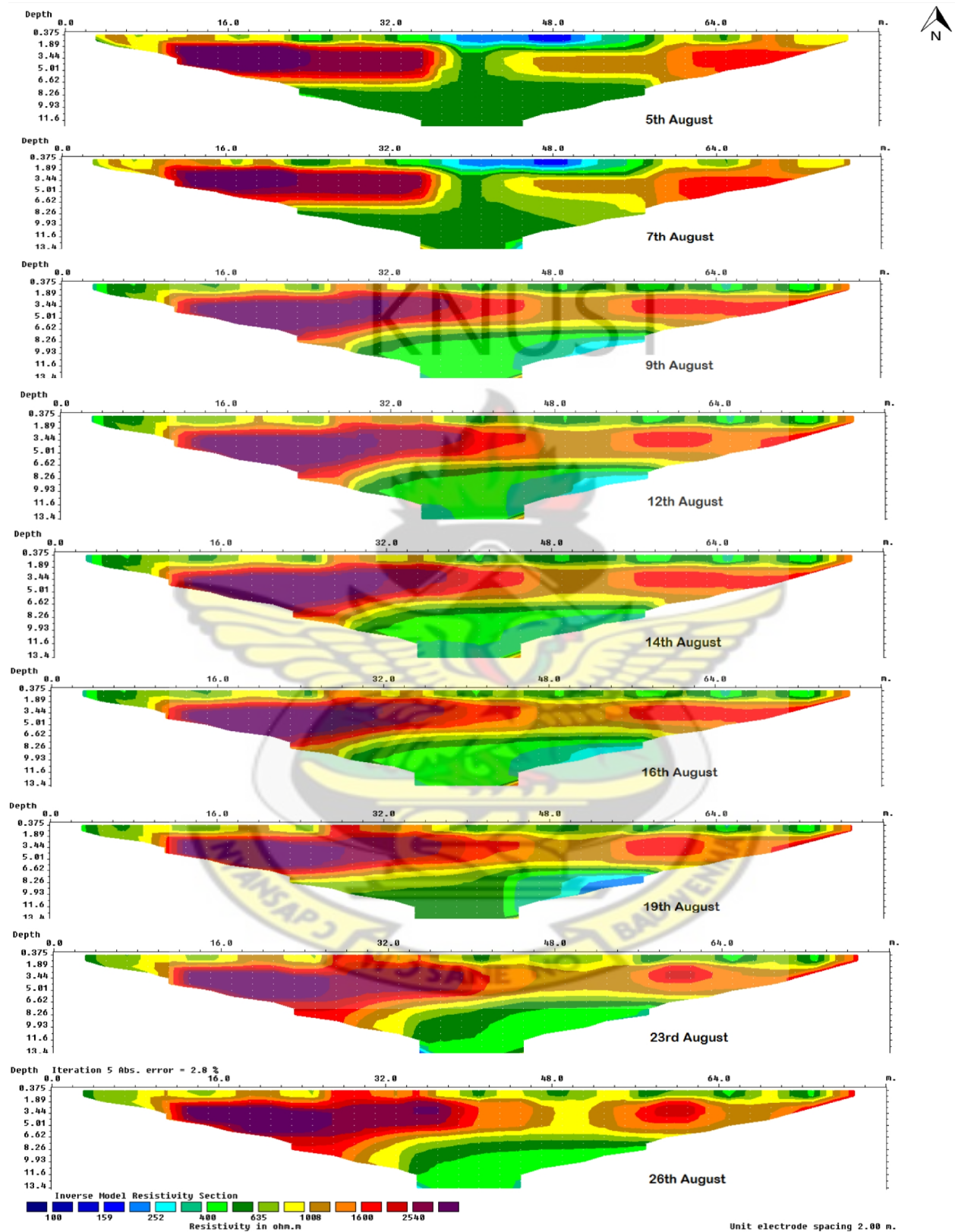
C 1: Resistivity results for August 2013 on line 1



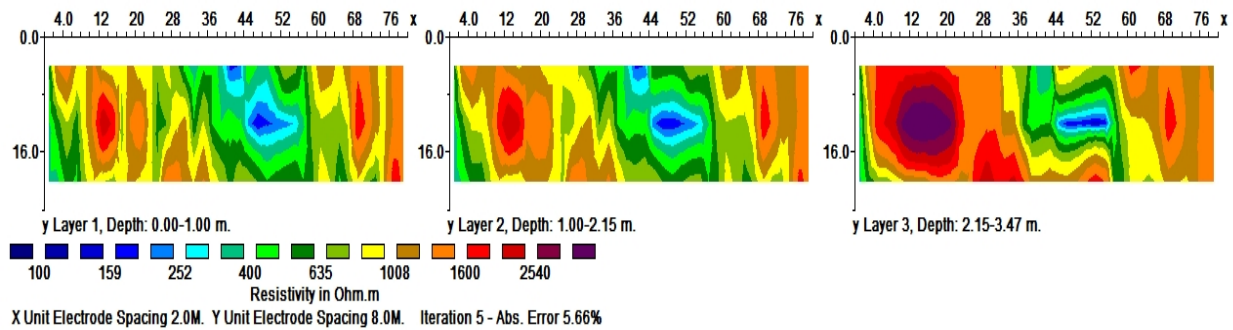
C 2: Resistivity results for August 2013 on line 2



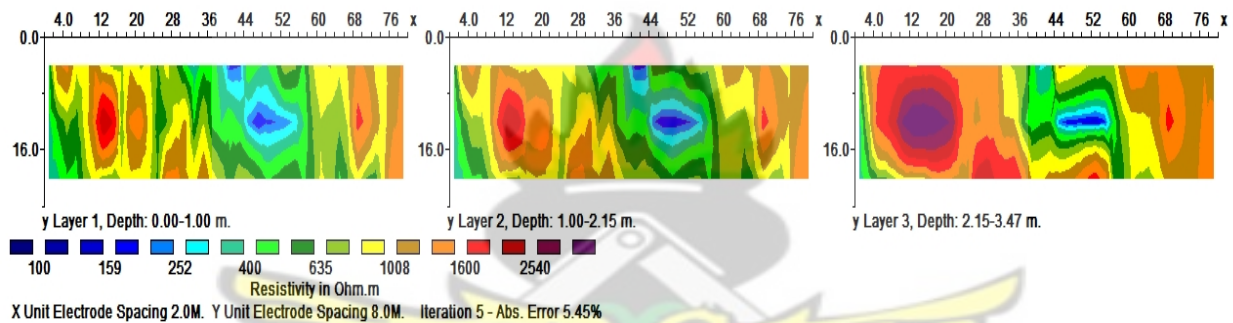
C 3: Resistivity results for August 2013 on line 3



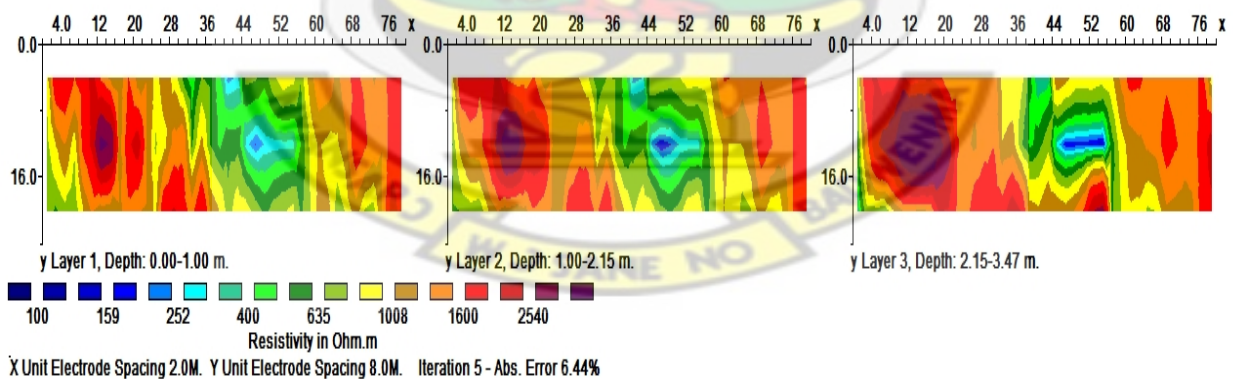
C 4: Resistivity results for August 2013 on line 4



C 5: 3D resistivity for 18th July 2013



C 6: 3D resistivity for 26th July 2013



C 7: 3D resistivity for 26th August 2013

KNUST

